WIRELESS POWER TRANSFER TO MM-SCALE BIOMEDICAL IMPLANTS

by

Erik John Andersen

A dissertation submitted to the faculty of
The University of Utah
in partial fulfillment of the requirements for the degree of

Doctor of Philosophy

Department of Mechanical Engineering

The University of Utah

August 2022

The University of Utah Graduate School

STATEMENT OF DISSERTATION APPROVAL

The dissertation of **Erik John Andersen**

has been approved by the following supervisory committee members:

Shadrach J. Roundy	, Chair	**July 20, 2022** Date Approved
Jake J. Abbott	, Member	**July 20, 2022** Date Approved
Stephen A. Mascaro	, Member	**July 20, 2022** Date Approved
Roseanne Warren	, Member	**July 20, 2022** Date Approved
Berardi Sensale Rodriguez	, Member	**July 21, 2022** Date Approved

and by **Bruce K. Gale** , Chair/Dean of

the Department/College/School of **Mechanical Engineering**

and by David B. Kieda, Dean of The Graduate School.

ABSTRACT

Biomedical implantable devices are a powerful tool for treatment of various ailments. However, biomedical implants' usefulness is limited by their requirement to devote a large percentage of their volume to energy storage. Wirelessly powering the implant enables for the removal or reduction of the implant's battery, allowing for device miniaturization. Smaller wirelessly powered implantable devices can be installed using minimally invasive surgery, are more conducive to high patient quality of life, and do not need to be removed to recharge their battery. This dissertation will explore the challenges and potential solutions to optimally wirelessly power mm-scale biomedical implants.

This dissertation will first explore the relationship between operating frequency and power transfer for weakly coupled resonant inductive coupling (RIC) and magnetoelectric (ME) WPTS. The operating frequency of the WPTS is important because of the B-field exposure safety standards that must be followed. These safety constraints prevent delivering more power to the receiver by increasing the power in the transmitter.

To ensure that the receiver has adequate B-field to power the biomedical implant, we develop an optimal design process for maximizing the B-field at the receiver while adhering to B-field safety, transmitter size, and power constraints. This design process was used to build a RIC WPTS for a biomedical knee stability sensor that can deliver 997 mWs at 10 cm.

Another potential problem when wirelessly powering biomedical implants is the

potential misalignment between the transmitter and receiver. We develop a novel approach to counteract misalignment and increase the efficiency of a WPTS using a dynamic transmit coil. The dynamic transmit coil uses servo motors to alter the directionality of the transmitted B-field by actuating the transmit coil.. We build a rotational dynamic transmit coil that increases the power transferred to a misaligned ME receiver by a factor of 2.2.

Finally, we build and characterize a small biomedical temperature sensor that uses a 12 x 5 x 1 mm^3 self-biased ME receiver. Our device can successfully read and transmit sensor data via Bluetooth radio and outperforms other ME WPTS built for biomedical implants when normalized by device volume and B-field

.

TABLE OF CONTENTS

LIST OF TABLES

Tables

ACKNOWLEDGMENTS

I would like to thank my advisor, Dr. Shad Roundy for all his help and guidance over countless hours while I completed my Ph.D. I would also like to thank the members of my advisory committee, Dr. Jake Abbott, Dr. Berardi Sensale-Rodriguez, Dr. Stephen Mascaro, and Dr. Roseanne Warren for their knowledge and help they imparted both as advisors and teachers.

Thank you to all the members of the ISS lab that supported me throughout my time in the lab. I would especially like to thank Dr. Binh Duc Troung for his help and mentorship to me. And I would like to thank all my friends and family that provided countless assistance these last 4 years. This work would not have been possible without the support of the NSF Grant ECCS-1651438.

CHAPTER 1

INTRODUCTION AND MOTIVATION

1.1 Wireless Power Transfer to Biomedical Implants

Nikola Tesla demonstrated the ability to transfer electrical power through the air at the turn of the 20th century. Famously, he envisioned a world where we would use the earth as a giant conduit to wirelessly power the world's electrical consumption needs. However, it would take about another century before Soljacic would demonstrate a resonant inductive wireless power transfer system (WPTS) that powered a light bulb across a 2-meter gap [1]. Stemming from this experiment in 2007 research into wireless power transfer exploded because of both the new and improved electrical components and tools and because of the vast array of small low powered smart devices (coincidently 2007 was also the first release of the iPhone) that have become ingrained in modern day society which are suited for wireless power transfer.

An example of a modern-day invention seemingly ideally suited for wireless power is implanted biomedical devices. Implantable biomedical devices are used to treat a variety of ailments, from glucose sensing for diabetics to treating sleep apnea. However, a significant drawback to these implants is their relatively large size, which can cause patient discomfort and limit the areas in the body in which they can be implanted. For example a Boston Scientific ACCOLADE Pacemaker L301 is 5 x 4.5 x 0.8 cm^3 [2].

Because implants are inaccessible except via surgery, their size is often constrained by their need for a battery that will last years [3]. Up to 90% of the biomedical implant's volume can be its battery [4]. However, once the battery is expired, the patient must undergo surgery to extract and replace the implant, which carries an inherent risk to the patient. Wirelessly powering the implant eliminates excess surgeries to removed expired devices. Additionally, removing or reducing the battery and wirelessly powering the device allows for device miniaturization, allowing for minimally invasive surgery to initially install the implant and reducing the patient's discomfort in their day-to-day life.

1.2 Inductive WPTS

Previous research in wireless power transfer (WPT) has addressed wirelessly powering biomedical implants. The majority of these works use a two-coil near field inductive wireless power system [5]–[10], or a multi- (more than three) coil system [11]–[13].

Inductive WPTS uses transmit and receive coils, often tuned and operated at a resonant frequency, and power is transmitted via a coupled magnetic field (B-field), as shown in Figure 1.1. An RF power amplifier is used to supply a high frequency AC current across the transmit coil, which emits a magnetic field (B-field). Some of the magnetic field passes through the receive coil, which induces a voltage according to Faraday's law

$$\nabla x\, E = -\frac{\partial B}{\partial t} \tag{1}$$

where E is the electric field, B is the magnetic field which for a closed loop receive coil

can be simplified to

$$V_{rx} = -n * A\frac{\partial B}{\partial t} \tag{2}$$

where V_{rx} is the voltage across the receive coil, n is the number of turns, and A is the area of the closed loop receive coil.

For inductive WPTS powering biomedical implants, the receive coil is implanted within the body and coupled with an external transmit coil. Most of these systems operate in the low-radio frequency (RF) region below 20 MHz, but some work has been done on higher RF frequencies [14]–[16]. Inductive wireless power systems operate most efficiently when the transmitter and receiver coils are of similar size and the mutual inductance, or coupling, is relatively high. As the size of implants continues to shrink, however, the receive coil will necessarily shrink with the following likely effects: the mutual inductance and coupling will fall, the size of the receive coil will become small compared to the implant depth, the size of the transmit coil will become large compared to the receive coil, and the optimal operating frequency will go up. An increase in frequency due to small size results in higher attenuation of the magnetic field in human tissue which further reduces the efficiency of the WPTS [17].

1.3 Magnetoelectric Transducers WPTS

Another method of wirelessly powering biomedical implants is through the use of magnetoelectric (ME) transducers. ME transducers typically utilize a magnetostrictive material that is laminated with a piezoelectric material. The key concept of a ME WPTS is shown in Figure 1.2. A ME transducer is utilized as a receiver, which converts a magnetic wave produced by a transmit coil to electrical power to supply a biomedical

implant. The ME WPTS first transforms the magnetic energy to mechanical vibrations through the interaction of magnetostrictive material and the applied field. The vibrational kinetic energy is then converted to electrical form by a piezoelectric phase.

ME transducers have recently been used as both transmit and receive antennas [18]–[20]. According to [21], for a given frequency, the characteristic wavelength of a ME antenna could be five orders of magnitude shorter than the electromagnetic wavelength, thus leading to more efficient energy transfer for small devices operating at low frequencies. This reduction occurs because the characteristic wavelength of a ME antenna is defined by its mechanical properties, whereas that of a typical coil antenna is determined by its electromagnetic properties. Comparing the overall system efficiency of very small receiver coil-based WPTS to ME receiver-based WPTS is an area of active research [22]–[25]. The outperformance of one system over another has not been conclusively shown. However, ME receiver-based WPTS seems promising given recent work [22], [26].

1.4 Safety Considerations for WPTS

Regardless of the form of wireless power transfer, patient safety should be a high priority when powering biomedical implants. Two main international agencies currently govern the use of low frequency (below 10 MHz) non-ionizing radiation: International Commission on Non-Ionizing Radiation Protection (ICNIRP), and the International Committee on Electromagnetic Safety (ICES, which is a subsidiary of IEEE). Each agency has released its recommendations for safety standards [27]–[29]. While these safety standards were originally derived for environmental field safety, they are still

applicable for wireless power transfer for medical applications.

The primary safety concerns with non-ionizing radiation exposure are RF shocks and burns, electrostimulation within the body, localized RF heating effects, surface heating effects, and whole-body heating effects. For frequencies below 5 MHz, RF shocks and electrostimulation are the primary concern. For frequencies of 100 kHz to 300 GHz, tissue heating becomes a major concern, especially as frequencies increase. In the region between 100kHz and 5 MHz, both the RF shocks and tissue heating must be considered by the designer. Given these adverse health effects, ICES and ICNRP have set exposure limits for both a controlled (occupational) environment and the general public.

For example, ICES has established "dosimetric reference limits (DRLs)" which are defined in terms of the electric field for RF shocks safety limit and Specific Absorption Rates (SARs) for the thermal heating safety limit. The SAR safety limit in a controlled environment is 0.4 W/kg whole-body exposure and 10 W/kg for localized exposure taken over a 6 minute period. But these Basic Restrictions can be challenging to measure and taxing to compute. Therefore, "exposure reference levels" or ERLs are introduced which are simpler and easier to measure. These are mostly defined in terms of magnetic field (B-field) exposure, although some ERLs are defined in terms of the electrical field exposure. ERL's are a more conservative safety estimate, a system complying with the ERLs will also comply with the DRLs and thus follow the safety regulations. The occupational/controlled-environment magnetic field exposure limits for both ICES and ICNRP as a function of frequency are presented in Figure 1.3.

The allowable B-field dramatically decreases as the frequency of the magnetic field increases. The B-field is especially limiting at frequencies above 100 kHz. For a

ME-based WPTS, the power of the receiver is proportional to the square of the B-field [30]. Thus, operating at frequencies below 100 kHz could result in higher safe power generation at the implant. Generating a B-field as close as possible to the allowable safety limit, depending on the chosen operating frequency, will maximize the available power at the implant.

The ERL limits are more appropriate and convenient for low frequency WPTS, such as ME transducers. For systems that operate at high RF frequencies (MHz – GHz range), the ERLs are so strict that it may be impossible to construct a useful WPTS that adheres to them. In these cases, directly calculating the DRL's (SARs) will offer better insight into the overall safety of the WPTS. However, we emphasize that ERLs can still be applied for RIC WPTS, as seen in a few works recently [31], [32].

However, currently, these safety standards are generally ignored in the design of WPTS for biomedical implants. A survey of 24 WPTS for biomedical implants [5], [6], [8]–[13], [22]–[26], [32]–[42] , comprising of both ME transducer and inductive WPTS, found that only six articles([5], [6], [17], [22], [32], [35]) even attempted to address the safety issues of their design using the IEEE or ICNIRP guidelines. Out of these six, two used the B-field ERLs to justify their safety, while four others calculated the SARs for their WPTS design. And when doing the SAR calculations, sometimes the WPTS designers had to resort to other post hoc correction factors to meet the safety standards, such as averaging the tissue heating over a large volume of tissue or duty cycling the transmit power.

While only a minority of WPTS for biomedical implants even address the safety aspect of their design, most of these only do so post hoc; once they've designed a system,

they test it to see if it meets the safety requirements. As far as we can tell, only one of these WPTS was designed with safety limitations as part of the driving aspect of the design. This dissertation will address how to optimally design a WPTS with regard to the safety constraints in Chapter 3.

1.5 Receiver Misalignment in WPTS

Besides adhering to magnetic field safety constraints, another consideration for wirelessly powering biomedical implants is the effect of misalignment between the receiver and the transmitter in the WPTS. Once the surgeon installs an implant, its exact location and orientation may be unknown. Misalignment between the receiver and the transmitter reduces the efficiency of the wireless power transfer system, and this reduction in efficiency is true for both inductive [43]–[49] and ME WPTS [30], which require the B-field to be aligned with the receiver for maximum wireless power transfer. This receiver location uncertainty is often ignored when designing WPTS for biomedical implants. The 24 WPTS for biomedical implants previously mentioned only reported the wireless power transfer in a perfectly aligned system.

The magnetic field exposure safety standards also prevent compensating for the misalignment, and thus reduced efficiency, by just increasing the transmit coil power, and thus increasing the WPTS B-field, to obtain a certain power level at the receiver. An inefficient WPTS could mean long recharge times for implants with a battery or passive implants (implants which no onboard energy storage) not receiving enough power to function.

Receiver misalignment can be compensated by adjusting the B-field to realign it

at the receiver. Research has been done on omnidirectional WPTS that can alter the direction of the B-field at a point or specific points in space. The most common construction of omnidirectional WPTS is multiple transmit coils configured either as orthogonal intersecting coils [50]–[52] or in a single plane [53]–[55], as shown in Figure 1.4. These omnidirectional WPTS can realign the B-field with a misaligned receiver at a point in space by using constructive interference of the B-field. However, the current planar coil arrays can only alter the B-fields at selected points in space depending on the geometry of the coil array. A different approach to a planar coil that can alter its B-fields directionality is through using a single solenoid transmit coil that is physically actuating and altering its position/orientation through servo motors. This new dynamic transmit coil will be presented in Chapter 5 as a novel method to account for receiver misalignment for WPTS powering biomedical implants.

1.6 Dissertation Outline

This dissertation will proceed as follows; first, we explore the relationship between power and frequency for both inductive and ME WPTS. Next, an optimal design procedure is presented that maximizes the received power at the biomedical implant while considering safety and other system constraints. This optimal design process is used to assist in the building of a wirelessly powered knee sensor to help measure muscle recovery post-surgery. Following that, a novel method to account for receiver location uncertainties and misalignment for WPTS powering biomedical implants is presented. And finally, a ME transducer WPTS for a biomedical implant is built, characterized, and compared to similarly sized inductive and ME WPTS.

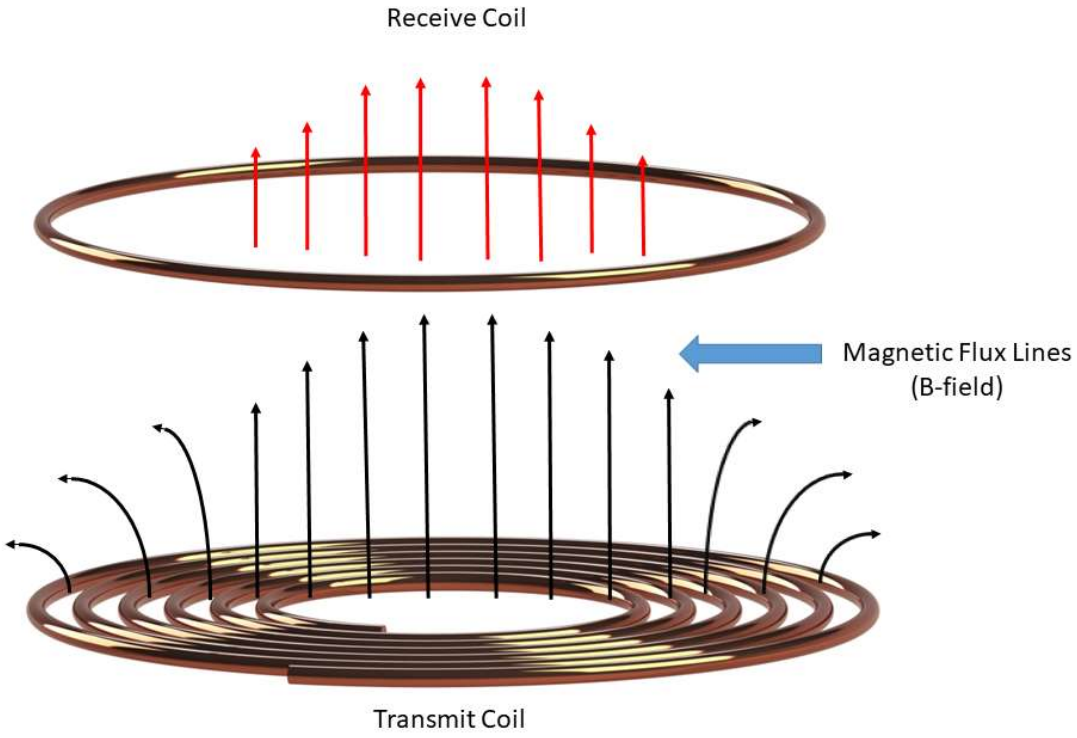

Figure 1.1 An inductive WPTS. An AC current is applied across the transmit coil generating magnetic flux (black arrows). According to Faraday's law, as some of the magnetic flux pass (red arrows) through the receive coil, it induces a voltage in the receive coil.

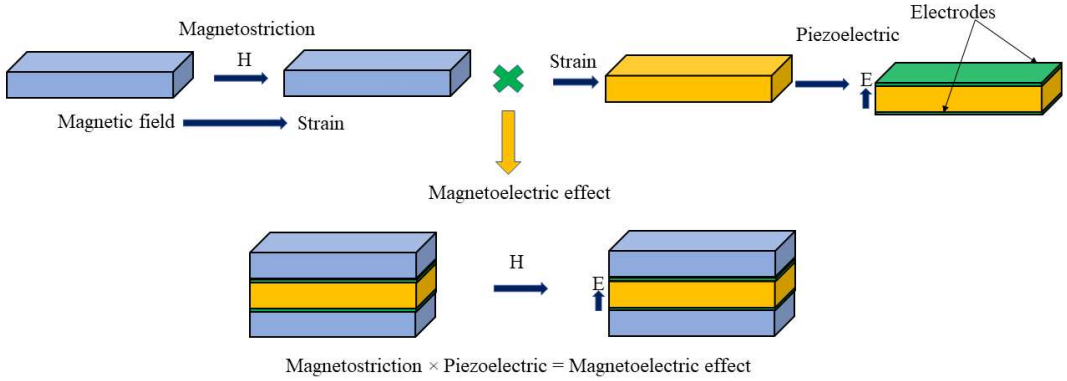

Figure 1.2 A system diagram of a magnetoelectric transducer receiver used in a ME WPTS. The B-field excites the magnetostrictive layer, causing it to vibrate. This vibration strains the piezoelectric layer, generating an electrical voltage.

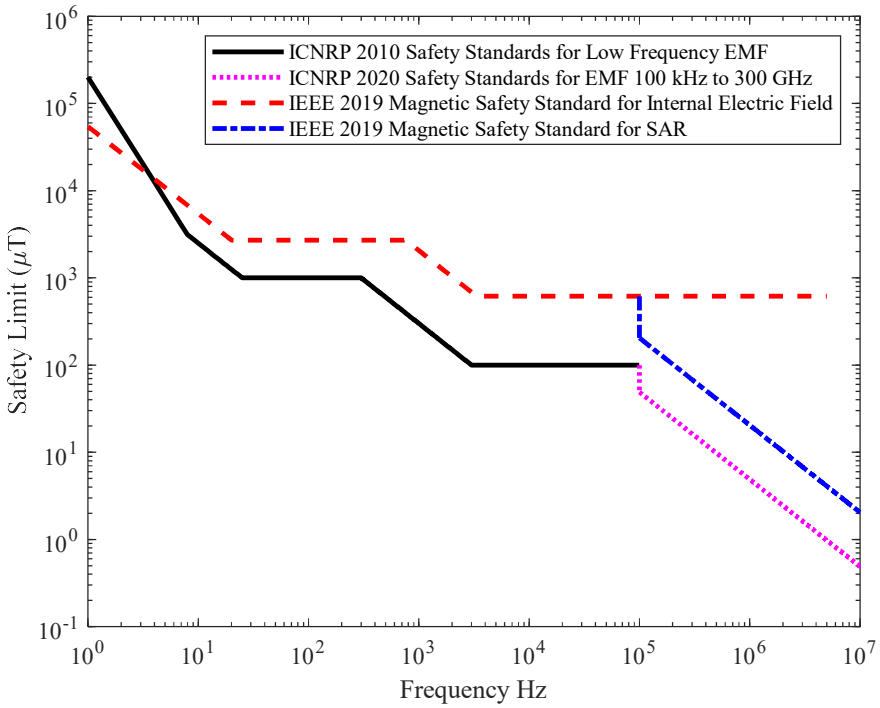

Figure 1.3 ICNRP AND IEEE ERLs for the B-field safety standards for human occupational/controlled-environment exposure as a function of frequency.

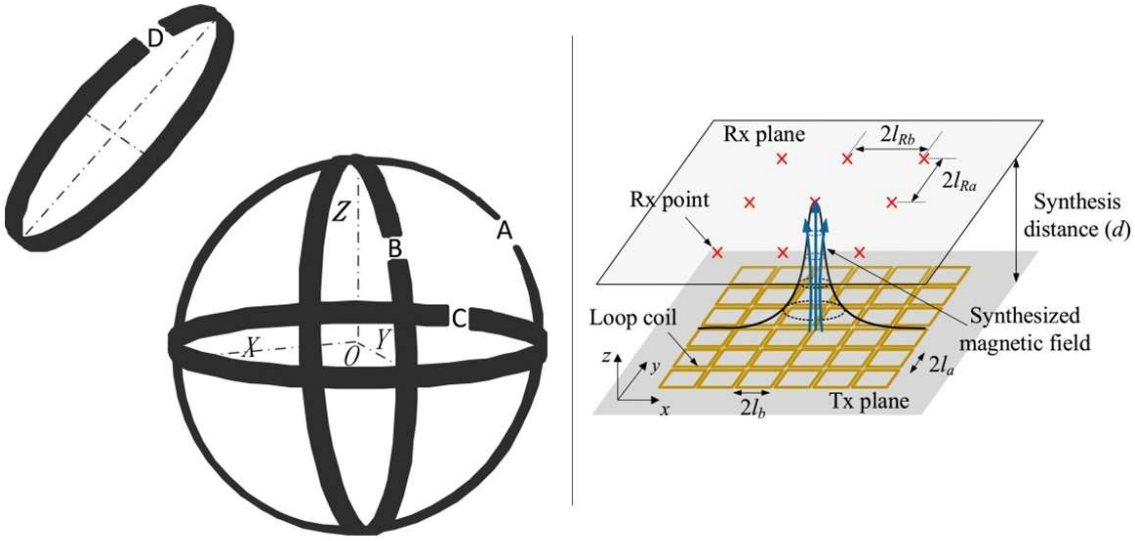

Figure 1.4 There are multiple types of omnidirectional WPTS. Left) An omnidirectional WPTS composed of orthogonal intersecting coils [51]. Right) An omnidirectional WPTS composed of planar coils [53].

CHAPTER 2

OPTIMAL TRANSMIT COIL DESIGN FOR WIRELESSLY FREQUENCY-DEPENDENCE OF POWER AND EFFICIENCY FOR RIC AND ME WPTS

This chapter explores the relationship between frequency and power transfer for different wireless power transfer systems. I would like to especially acknowledge the contributions of Dr. Binh Duc Truong in formal analysis and as an advisor of the work.

2.1 Introduction

Wireless power transfer systems (WPTSs) actively transmit power from a source to a receiver, providing deterministic control over the generated power [1], [56]. This property has made wireless power transfer (WPT) a promising means to supply energy for low power electronics such as wireless sensors, especially for implantable devices where using traditional batteries raises many safety concerns [36], [57]. Among methods based on electromagnetic fields, near–field resonant inductive coupling is perhaps the most commonly used structure [58], [59]. In the last few years, wireless power transfer systems (WPTSs) utilizing magnetoelectric (ME) effects have emerged as an attractive alternative due to their excellent miniaturization potential without compromising much of the power delivery capability [21], [60], [61]. In this work, we narrow our focus to these

two methods.

Most WPTSs consider the link efficiency, defined by the ratio between the power delivered to the load and the power input to the transmitter, as the primary objective. However, the safety standards regulated by the Institute of Electrical and Electronics Engineers (IEEE) and the International Commission on Non–Ionizing Radiation Protection (ICNIRP) are not related to efficiency but to actual power generated at the receiver side, drive frequency, magnetic flux density, and Specific Absorption Rates (SARs) [27]–[29]. The average energy flux density and average power density carried by an electromagnetic wave are shown to be proportional to its frequency and frequency squared, respectively [62]. However, the relationship between the power captured by a receiver and the wave frequency, which depends on the physics of energy conversion it obeys, has not been thoroughly studied. Exploring the direct influence of drive frequency on the generated power of a given mechanism could create a convenient bridge for designing an efficient WPTS used for biomedical applications, particularly when subject to safety requirements.

In contrast to WPT, energy harvesting (EH) systems convert the available energy from environmental sources and provide enduring power without any “cost" [63]. In recent years, inductively scavenging energy from current–carrying structures such as power lines has demonstrated its potential as an approach to power wireless sensor networks [64]–[66]. Instead of efficiency, the output power (or sometimes the power density) is the paramount quantity of interest for an EH system. Determining the power–frequency dependence in the relationships with other parameters and how this dependence changes under different scenarios (e.g., resonant or non–resonant) could

bring further insight into these devices.

In this chapter, we investigate both the efficiency and output power of the RIC and ME WPTSs and determine the conditions to maximize these two quantities. The central objectives are to explore the changes in power generation and transfer efficiency under the variations of the drive frequency. RIC WPTS has been largely investigated in the literature. However, here we not only summarize classic, well–known results, such as the efficiency of RIC WPTS, but also further interpret them to determine the relationship between power and frequency for different RIC WPTS. Additionally, we explore the unrevealed properties to form the most comprehensive and universal framework possible for both structures (especially for deriving the efficiency and relationship between power and frequency for for ME WPTSs). Other efforts are devoted to introducing a figure of merit for each configuration and unifying the expressions of power (and efficiency) of the two architectures in the same general form, written as a function of the figure of merit. Some important results are also applicable to relevant inductive EH or magneto–mechano–electric WPT systems.

2.2 Power Optimization of WPT at Weak Coupling Regime and Inductive Energy Harvesting

Figure 2.1 depicts the key concepts of the inductive-based WPT and EH systems. With the focus on biomedical wearable and implantable applications, in the following study, we presume that the coupling between the transmitter and receiver of the WPTS is weak due to the mismatch between their sizes and a long transfer distance compared to the receiver dimensions. Therefore, the impedance reflected onto either of them is also

neglected. The transmitter is now considered a source of magnetic waves that can provide any field strength at any frequency. This analysis, therefore, applies to both EH systems that scavenge energy from magnetic fields available in the environment and weakly-coupled WPTSs.

For a given magnetic flux density **B**, the magnetic flux passing through a surface **S** is

$$\begin{aligned} \Phi &= \iint_S \boldsymbol{B} \cdot \mathrm{d}\boldsymbol{S} \\ &= B \cdot S = BS\cos\theta \end{aligned} \qquad (3)$$

where B is the magnitude of the magnetic flux density, S is the surface area which is assumed to be a finite area, and θ is the angle between the magnetic field lines and the normal (perpendicular) to **S**. B is assumed to be uniform in the region of S. For the sake of simplification, from now on we consider $\theta = 0$ unless otherwise stated; equivalently, $\Phi = BS$.

Considering a solenoid coil of N turns exposed to a uniform magnetic flux density **B** as illustrated in a close-up view of Figure 2.1, according to Faraday's law of induction, the induced electromotive force (EMF) is

$$V_{\mathrm{EMF}} = -N\frac{\mathrm{d}\Phi}{\mathrm{d}t} = -NS\frac{\mathrm{d}B}{\mathrm{d}t}. \qquad (4)$$

With a time harmonic magnetic flux density $B(t) = -B_0\sin\omega t$ of angular frequency ω, the EMF can be written as $V_{\mathrm{EMF}} = V_0\cos\omega t$ where

$$V_0 = \omega B_0 NS. \qquad (5)$$

Given receiver geometry, V_0 is proportional to ω. When a planar spiral coil is used, $V_0 = \omega B_0 \sum_{i=1}^{N} S_{\mathrm{i}}$ where S_{i} is the corresponding area of the i^{th} turn.

When connecting the two terminals of the receiver (or harvester) with an

electrical load, the EMF becomes a voltage source of the circuit. The power induced in the load then depends on the magnitude and frequency of the magnetic fields and the impedance characteristics of the receiving system. The primary aim of this section is to explore the relationships between the maximum generated power and the frequency under different scenarios that can take place in practice.

2.2.1 A General Model for Small-Scale Receiver Coil

We first investigate the maximum possible power that a receiver or harvester can provide by considering a single-coil resonator loaded with a resistance. A general model of this resonator is shown in Figure 2.2, in which an external capacitance C is in series with the coil inductance L. In many cases, the coil parasitic capacitance C_{p} is relatively smaller than C and is neglected. However, C_{p} may have a significant impact on the dynamics of the receiver and the performance of the output power in principle [67]. Therefore, it is included for a comprehensive analysis.

A convenient method to examine the output power is to use the The′venin equivalent circuit such as that demonstrated in Figure 2.3. The The′venin voltage and impedance are derived as follows,

$$V_{\mathrm{th}} = V_0 \frac{1/j\omega C_{\mathrm{p}}}{R + j\omega L + 1/j\omega C_{\mathrm{p}}}, \tag{6}$$

$$Z_{\mathrm{th}} = Z_{\mathrm{out}} = \frac{1}{j\omega C} + \frac{1}{j\omega C_{\mathrm{p}}} \frac{R + j\omega L}{R + j\omega L + 1/j\omega C_{\mathrm{p}}}. \tag{7}$$

The voltage across the load resistance and the output power are given by

$$V_{\mathrm{L}} = \frac{V_{\mathrm{th}}}{Z_{\mathrm{out}} + R_{\mathrm{L}}} R_{\mathrm{L}}, \tag{8}$$

$$P = \frac{1}{2}\frac{{V_{\mathrm{L}}}^2}{R_{\mathrm{L}}} = \frac{1}{2}\frac{{V_{\mathrm{th}}}^2}{Z_{\mathrm{out}} + {R_{\mathrm{L}}}^2} R_{\mathrm{L}}. \tag{9}$$

The impedance matching conditions to achieve the maximum power delivered to the load are

$$\begin{cases} \Re\{Z_{\mathrm{out}}\} = R_{\mathrm{L}} \\ \Im\{Z_{\mathrm{out}}\} = 0, \end{cases} \tag{10}$$

which yield the optimal values of the load resistance and series capacitance as

$$R_{\mathrm{L}} = \frac{R}{(QQ_{\mathrm{p}} - 1)^2 + Q_{\mathrm{p}}^2}, \tag{11}$$

$$C = C_{\mathrm{p}} \frac{(QQ_{\mathrm{p}} - 1)^2 + Q_{\mathrm{p}}^2}{Q_{\mathrm{p}}(Q - Q_{\mathrm{p}}(Q^2 + 1))} \tag{12}$$

where $Q = \omega L/R$ and $Q_{\mathrm{p}} = \omega C_{\mathrm{p}} R$. The necessary and sufficient condition such that $C > 0$ is $Q_{\mathrm{p}} < Q/(Q^2 + 1) \leq 1/2$. This solution leads to the output power

$$P = \frac{1}{8}\frac{V_0^2}{R} = \frac{1}{8}\frac{(\omega B_0 NS)^2}{R}, \tag{13}$$

which is also the largest possible power the receiver can produce. This maximum power is referred to as the power limit, denoted as P_{lim}.

From the circuit theory point of view, V_{EMF} and R play a role as an effective power source for a lossless two-port network formed by $\{L, C_{\mathrm{p}}, C\}$, and P_{lim} is the power available for extraction. In the later stage, the output port of the T–network is connected to the load resistance R_{L} at which the electrical energy converted is consumed. Equation (13) is a simple and efficient means to predict the maximum output power of a magnetic energy harvester or a weakly coupled WPTS. Especially in the latter case, there is no need to explicitly identify the dynamics of the transmitter, the actual coupling coefficient between the two coils, or the system efficiency, but only the field strength at the receiver.

The wave frequency is typically known ahead of time.

The results obtained in this section hold regardless of whether R is a constant or frequency-dependent. It is important to note that the power expression (13) can be considered as a quadratic function of the frequency of the propagating waves when R is nearly unchanged with respect to frequency. In the next sections, we study the relationships between the maximum output power and the frequency under different scenarios in practice where (13) may or may not be reached.

2.2.2 Case I: Low-Frequency Nonresonant Transducer

Magnetic energy harvesting systems with a pickup coil usually operate at low frequencies at which the parasitic capacitance C_{p} is negligibly small and therefore disregarded. Furthermore, the required optimal capacitance C for forming a resonator is too large to implement. In these circumstances, the general model shown in Figure 2.2 can be simplified to that in Figure 2.4.

The output power now reads as

$$P = \frac{1}{2} V_0^2 \frac{R_{\mathrm{L}}}{(R + R_{\mathrm{L}})^2 + (\omega L)^2}. \tag{14}$$

Since the two conditions in (10) cannot be satisfied simultaneously, the impedance matching condition is then given by $R_{\mathrm{L}} = Z_{\mathrm{out}}$ where $Z_{\mathrm{out}} = R + j\omega L$. In particular, the optimal load and the corresponding maximum power are

$$R_{\mathrm{L}} = R\sqrt{1 + Q^2}, \tag{15}$$

$$P = \frac{1}{8} \frac{V_0^2}{R} \frac{2}{1 + \sqrt{1 + Q^2}} < P_{\mathrm{lim}} = \frac{1}{8} \frac{V_0^2}{R} \ \forall \, Q. \tag{16}$$

We note that using the gradient descent method leads to the same results. At low

frequency, L and R are almost constant, $V_0^2 \propto \omega^2$ and $Q \propto \omega$. Therefore, $P \propto \omega$ when $Q \gg 1$, approximately.

2.2.3 Case II: Resonant Energy Harvester and Wireless Power Transfer Receiver

We now consider a scenario where C_p is still negligibly small and is ignored. However, at the same time, there exists suitable capacitance C connected in series with L to form a resonator. This configuration is described in Figure 2.5, in which the operating frequency is usually between a few tens kHz up to a few tens MHz.

The generated power in this case is computed as

$$P = \frac{1}{2} V_0^2 \frac{R_\mathrm{L}}{(R + R_\mathrm{L})^2 + (\omega L - 1/\omega C)^2}. \tag{17}$$

Similarly, the optimal values of load resistance and output power are

$$R_\mathrm{L} = R\sqrt{1 + (Q - 1/Q_\mathrm{c})^2}, \tag{18}$$

$$P = \frac{1}{8}\frac{V_0^2}{R}\frac{2}{1 + \sqrt{1 + (Q - 1/Q_\mathrm{c})^2}} \leq P_\mathrm{lim}\ \forall \{Q, Q_\mathrm{c}\} \tag{19}$$

where $Q_\mathrm{c} = \omega RC$. At the resonance frequency $\omega_0 = 1/\sqrt{LC}$, we have $QQ_\mathrm{c} = 1$, $R_\mathrm{L} = R$, and the equality is attained.

In brief, in order to maximize the output power, the resonance frequency ω_0 of the resonator needs to be tuned to match the magnetic field frequency ω, and the load resistance is adapted to the resistance of the coil simultaneously. Similar to (13), $P \propto \omega^2$.

2.2.4 Case III: High-Frequency Wireless Power Transfer Receiver

For a WPTS operating at high frequency, the effect of the parasitic capacitance is significant and must be taken into account. On the contrary, the use of an external capacitor may no longer be feasible. And more importantly, it may be not necessary. The following analysis is to clarify this argument.

The equivalent circuit for this circumstance is shown in Figure 2.6. The power delivered to the load is determined by

$$\begin{aligned} P &= \frac{1}{2} V_0^2 \frac{R_\mathrm{L}}{R_\mathrm{L} + (j\omega R_\mathrm{L} C_\mathrm{p} + 1)(R + j\omega L)^2} \\ &= \frac{1}{2} \frac{V_0^2}{R_\mathrm{L}} \frac{1}{[1 + R/R_\mathrm{L} - QQ_\mathrm{p}]^2 + [QR/R_\mathrm{L} + Q_\mathrm{p}]^2}. \end{aligned} \tag{20}$$

Using the gradient descent approach, the optimal load at each frequency is

$$R_\mathrm{L} = R\sqrt{\frac{1 + Q^2}{(1 - QQ_\mathrm{p})^2 + Q_\mathrm{p}^2}}. \tag{21}$$

Moreover, the optimal load and frequency can be simultaneously determined by the impedance matching conditions $\Re\{Z_\mathrm{out}\} = R_\mathrm{L}$ and $\Im\{Z_\mathrm{out}\} = 0$ where

$$Z_\mathrm{out} = \frac{1}{j\omega C_\mathrm{p}} \frac{R + j\omega L}{R + j\omega L + 1/j\omega C_\mathrm{p}}, \tag{22}$$

which results in the solution

$$R_\mathrm{L} = R(1 + Q^2), \tag{23}$$

$$\omega^2 = (LC_\mathrm{p})^{-1} - (R/L)^2. \tag{24}$$

This solution is real for $L > C_\mathrm{p}R^2$, or equivalently, $Q > Q_\mathrm{p}$. Note that (23) is a particular case of (21) at a specific frequency ω that is given by (24). From (23) and (24), we observe that both optimal frequency and load resistance solely depend on the electrical

characteristics of the coil $\{L, R, C_{\mathrm{p}}\}$. We also have the relation $1/Q_{\mathrm{p}} = Q + 1/Q$.

At the optimal load and frequency conditions, the corresponding maximum output power is

$$P = \frac{1}{8}\frac{V_0^2}{R} = P_{\mathrm{lim}}. \tag{25}$$

This result shows that P is still able to reach its global maximum P_{lim} without the need for an added capacitance. In practice where the wave frequency is known beforehand, it is desired to design a receiver coil whose properties satisfy the condition (24), and the load resistance is chosen based on (23).

The results obtained in this subsection are applicable for a receiver resonator configured in parallel, in which C_{p} now represents the sum of the added capacitance and the parasitic capacitance. Given the same resonator parameters, the optimal frequency of the parallel configuration is slightly smaller than that of the series structure. Meanwhile, the optimal load resistance of the former is higher than that of the latter. Therefore, choosing which type of connection, series or parallel, strongly depends on the loading condition.

The findings presented in three cases {I, II, III} together with a more general form shown in Figure 2.2 can cover the most commonly used structures in EH and WPT systems. These investigations provide explicit relationships between the maximum output power and operating frequency, and at the same time, show how to reach the power limits under each circumstance.

2.2.5 On the Constant Magnetic Field

Considering the weak coupling condition in which the reflected impedance on the transmit side of a RIC WPTS is negligible, the generated magnetic field then solely depends on the transmitter geometry and the current flowing in it. A constant current amplitude that produces a constant B–field can be accomplished by adapting an external series-capacitance such that the imaginary parts of the transmitter impedance cancel out each other, which is equivalent to forming a resonator. Under the resonance condition, the input current is a function of the coil resistance, but not inductance, and therefore is independent of frequency. This technique is able to produce constant magnetic field strength over a wide range of frequencies.

2.3 Efficiency Consideration of a Resonant Inductive Coupling Wireless Power Transfer System

When the transfer efficiency is chosen as the objective of the study, the output power is bounded by the power available from a source. For a given power source, the magnetic field strength is determined by the current flowing into the transmitter coil, which depends on the input impedance of the system that is a function of the operating frequency. Therefore, B_0 is not independent of ω in general. This is the fundamental difference between the efficiency maximization and power optimization problems presented in Section 2.2. The efficiency is obviously always less than unity. However, the dependence of the efficiency on the drive frequency is still of great interest.

The maximum achievable transfer efficiency for a two-coil RIC WPTS is asymptotically expressed in the following form [68], [69]

$$\eta = \frac{k^2 Q_1 Q_2}{(\sqrt{1 + k^2 Q_1 Q_2} + 1)^2} \tag{26}$$

where Q_1 and Q_2 are the unloaded quality factors of the transmitter and receiver coils, respectively. In particular, $Q_{\mathrm{i}} = \omega L_{\mathrm{i}}/R_{\mathrm{i}}$, where $\mathrm{i} = \{1,2\}$. The coupling coefficient is defined by $k = M/\sqrt{L_1 L_2}$, where M is the mutual inductance between the two coils. The efficiency expression (26) is applicable to approximate the global optimum efficiency of the four configurations, series–series, series–parallel, parallel–series, and parallel–parallel [69]. It is essential to note that (26) is attained if and only if the impedance matching conditions to both source and load are satisfied, that is

$$\begin{cases} R_{\mathrm{s}} = R_1\sqrt{1 + k^2 Q_1 Q_2}, \\ R_{\mathrm{L}} = R_2\sqrt{1 + k^2 Q_1 Q_2}, \end{cases} \tag{27}$$

and $\omega = 1/\sqrt{L_{\mathrm{i}} C_{\mathrm{i}}}$. The corresponding maximum output power is

$$P = \eta P_{\mathrm{avs}}. \tag{28}$$

Here, $P_{\mathrm{avs}} = {V_{\mathrm{s}}}^2/8R_{\mathrm{s}}$ is the power available from the source that is represented by a series circuit with a source voltage V_{s} and a resistor R_{s}. For a given power source, P_{avs} is defined and independent of frequency. It is apparent that P is a linear function of η in the form of $y = ax$.

Some authors refer to the term $k^2 Q_1 Q_2$ to as the figure of merit of a RIC WPTS since it directly determines the magnitude of the transfer efficiency. An obvious observation is that η always increases with the increase of $k^2 Q_1 Q_2$. Given the geometries of the transmitter and receiver and the distance between them, the coupling coefficient is a constant. A convenient approach to enhance $k^2 Q_1 Q_2$ is to enlarge the Q–factors by operating at higher frequencies.

In the weak coupling regime, $k^2 Q_1 Q_2 \ll 1$, the optimal load (i.e., the second condition in (28) is approximately $R_\mathrm{L} \approx R_2$. This result coincides with that in Section 2.3, which indicates that *maximizing the efficiency is considered equivalent to optimizing the output power under a given magnetic field for the weakly coupled condition*. At the same time, matching the source resistance with that of the transmitter coil $R_\mathrm{s} \approx R_1$ maximizes the input power, and as a consequence, the **B**–field generated. The maximum efficiency and output power can be approximated by

$$\eta \approx \frac{1}{4} k^2 Q_1 Q_2, \tag{29}$$

$$P \approx \frac{P_\mathrm{avs}}{4} k^2 Q_1 Q_2. \tag{30}$$

A comparison between the maximum achievable efficiency and its estimation at weak coupling is shown in Figure 2.7. Under the situation where $k^2 Q_1 Q_2 \ll 1$, both η and P are proportional to frequency squared since $Q_1 Q_2 \propto \omega^2$.

It should be emphasized that, in the low coupling regime, no matter whether we neglect the reflected impedances on the transmitter and receiver sides or we consider the dynamics of the entire system, the quadratic relationship between the maximum output power and the frequency always holds. However, the derivations in Section 2.1 are favorable to approximate P since determining the **B**–field strength generated by the transmitter at the receiver location is more convenient than measuring the coupling between the two coils. For a strongly coupled RIC WPTS with high quality factors, $k^2 Q_1 Q_2 \gg 1$, $\eta \approx 1 - 2/\sqrt{x} + 2/x \to 1$ and $P \to P_\mathrm{avs}$, where x represents $k^2 Q_1 Q_2$.

2.4 Power Optimization of Magnetoelectric Wireless Power Transfer and Energy Harvesting

The concept of a ME WPTS is depicted in Figure 2.8, in which the transmitter is a circular coil similar to that of a RIC WPTS, but the receiver in this case is a ME transducer composed of two magnetostrictive layers and one piezoelectric layer instead of a pick-up coil. The magnetic energy captured by the magnetostrictive material is transformed into the vibration of the ME composite. The vibrational kinetic energy is then converted to electricity through the direct piezoelectric effect.

It is possible to operate a RIC WPTS at different frequency bands *with given geometries of the two coils* by choosing appropriately external capacitances. However, the optimal operating frequency of a ME WPTS is usually at or near the mechanical resonance or anti-resonance frequencies. These two specific frequencies are directly dependent on the receiver geometry. Therefore, geometry optimization and the power–frequency relationship are always two inseparable problems for a ME WPTS. A thorough study to address the relevant questions was presented in [70].

Mechanical Q–factor, a dimensionless parameter, is widely used as a criterion to examine the efficiency of a mechanical system [71]. In order to evaluate the performance of a ME WPTS as fairly as possible when subject to the change of the receiver geometric dimensions, we assume that the mechanical quality factor is constant and is independent of the geometry. Following this assumption, it is shown that the maximum output power is proportional to the operating frequency [70]. More importantly, such a property holds regardless of the magnitude of the volume constraint.

2.5 Efficiency and Figures of Merit of a Magnetoelectric Wireless Power Transfer

Figure 2.9 shows an equivalent circuit model to investigate the overall transfer efficiency of a ME WPTS. The internal impedance of the source is expressed in a general form of $Z_{\mathrm{s}} = R_{\mathrm{s}} + jX_{\mathrm{s}}$. L_1 and R_1 represent the inductance and resistance of the transmitter coil, and C_1 is an external capacitor connected in series with $\{L_1, R_1\}$. Ψ_{m} is the effective electrodynamic transduction factor that relates the input current and the electromotive voltage V_{e} to the equivalent force F_0 acting on the ME composite and its longitudinal velocity respectively. Z denotes the mechanical impedance, and b is the mechanical damping coefficient. The coupling between the mechanical and electrical domains at the final stage of the conversion is represented by the electromechanical transduction factor Γ_{p}. C_0 is the nominal capacitance of the piezoelectric element (parasitic capacitances are typically very small by comparison to the piezoelectric capacitance), and R_{L} is the load resistance connected at the output terminals of the ME transducer.

Two widely used criteria to evaluate the performance of a two-port network are the transducer power gain η_{t} and the operating power gain η_{p}, defined as

$$\eta_{\mathrm{t}} = \frac{\text{power delivered to the load}}{\text{power available from the source}} = \frac{P_{\mathrm{L}}}{P_{\mathrm{avs}}}, \qquad (31)$$

$$\eta_{\mathrm{p}} = \frac{\text{power delivered to the load}}{\text{power input to the network}} = \frac{P_{\mathrm{L}}}{P_{\mathrm{in}}}. \qquad (32)$$

in which η_{p} is usually referred to as the power transfer efficiency or the link efficiency in the field of WPT. η_{t} is a lower bound of η_{p} since $\eta_{\mathrm{t}} \leq \eta_{\mathrm{p}}$ for any WPTS. We now maximize η_{t} and η_{p} based on impedance matching principle. We choose $R_{\mathrm{s}}, X_{\mathrm{s}}, C_1, \omega$ and

R_{L}, which are not characteristics of the transmitter or receiver, as objective variables of the optimization problem.

$\Psi_{\mathrm{m}}, Z, \Gamma_{\mathrm{p}}$ and C_0 are derived as

$$\Psi_{\mathrm{m}} = \Lambda_{\mathrm{H-I}}\Gamma_{\mathrm{m}} = \Lambda_{\mathrm{H-I}}(2wt_{\mathrm{m}}d_{33,\mathrm{m}}/s_{33}^{\mathrm{H}}), \tag{33}$$

$$Z = -j\left(\frac{n}{s_{11}^{\mathrm{E}}} + \frac{1-n}{\kappa s_{33}^{\mathrm{H}}}\right)\frac{A}{2\overline{v}}\cot\frac{\omega L}{2\overline{v}}, \tag{34}$$

$$\Gamma_{\mathrm{p}} = -wd_{31,\mathrm{p}}/s_{11}^{\mathrm{E}}, \tag{35}$$

$$C_0 = \epsilon_{33}^{\mathrm{S}}wL/t_{\mathrm{p}}. \tag{36}$$

$\Lambda_{\mathrm{H-I}}$ is a coefficient describing the relationship between the current input to the transmitter coil and the magnetic field strength it generates at the location of the ME device. $\Lambda_{\mathrm{H-I}}$ is dependent on the coil geometry, distance between transmitter and ME device, and the orientation of the ME device relative to the transmit coil. An example of how to determine $\Lambda_{\mathrm{H-I}}$ for a thick coil with rectangular cross section is presented in Section 2.9. Γ_{m} is the magneto-elastic transduction factor (it is also sometimes referred to as the electrodynamic transduction factor). The definitions of the material constants and other necessary quantities are as follows. L and w are the length and width of the ME laminate, while t_{p} and t_{m} are the thicknesses of the piezoelectric and magnetostrictive layers, respectively. $d_{33,\mathrm{m}}$ is the piezomagnetic constant. s_{33}^{H} is the elastic compliance at constant magnetic field. s_{11}^{E} is the elastic compliance of the piezoelectric material under constant electric field. $d_{31,\mathrm{p}}$ is the transverse piezoelectric charge constant. $\epsilon_{33}^{\mathrm{T}}$ – is the dielectric permittivity under constant stress. $\epsilon_{33}^{\mathrm{S}}$ is the permittivity component at constant strain with the plane-stress assumption of a thin narrow beam (i.e., $\epsilon_{33}^{\mathrm{S}} = \epsilon_{33}^{\mathrm{T}} - d_{31,\mathrm{p}}^2/s_{11}^{\mathrm{E}}$). κ is the interface coupling coefficient relating the stress transferred between

the magnetostrictive and piezoelectric materials, $0 \le \kappa \le 1$. A, n and $\overline{v}^2$ are the cross-sectional area, the thickness ratio, and the squared speed of sound in the composite, respectively,

$$A = w(t_\mathrm{p} + 2t_\mathrm{m}), \tag{37}$$

$$n = t_\mathrm{p}/(t_\mathrm{p} + 2t_\mathrm{m}), \tag{38}$$

$$\begin{aligned} \overline{v}^2 &= \frac{1}{\overline{\rho}}[n(s_{11}^\mathrm{E} - \frac{d_{31,\mathrm{p}}^2}{\epsilon_{33}^\mathrm{T}})^{-1} + \frac{1-n}{\kappa}(s_{33}^\mathrm{H} - \frac{d_{33,\mathrm{m}}^2}{\mu_{33,\mathrm{m}}^\mathrm{T}})^{-1}] \\ &= [n/s_{11}^\mathrm{D} + (1-n)/(\kappa s_{33}^\mathrm{B})]/\overline{\rho}, \end{aligned} \tag{39}$$

$\mu_{33,\mathrm{m}}^\mathrm{T}$ is the magnetic permeability at constant stress. The equivalent mass density of the ME laminate is

$$\overline{\rho} = n\rho_\mathrm{p} + (1-n)\rho_\mathrm{m}/\kappa \tag{40}$$

where ρ_p and ρ_m are the mass densities of the piezoelectric and magnetostrictive materials, respectively.

Writing Z in the form of $Z = jZ_0$, the input and output impedances are

$$Z_\mathrm{in} = j\omega L_1 + \frac{1}{j\omega C_1} + \frac{\Psi_\mathrm{m}^2}{Z_\mathrm{M}} + R_\mathrm{L}, \tag{41}$$

$$Z_\mathrm{out} = \frac{\frac{1}{j\omega C_0}\frac{jZ_0 + Z_\mathrm{N} + b}{\Gamma_\mathrm{p}^2}}{\frac{1}{j\omega C_0} + \frac{jZ_0 + Z_\mathrm{N} + b}{\Gamma_\mathrm{p}^2}} \tag{42}$$

where the intermediate parameters Z_M and Z_N are

$$\begin{aligned} Z_\mathrm{M} &= Z + b + \Gamma_\mathrm{p}^2 \frac{R_\mathrm{L}}{1 + j\omega R_\mathrm{L} C_0} \\ &= jZ_0 + b + \Delta K_\mathrm{p} \frac{\tau_\mathrm{p}}{1 + j\omega\tau_\mathrm{p}}, \end{aligned} \tag{43}$$

$$Z_{\mathrm{N}} = \frac{\Psi_{\mathrm{m}}^2}{j\omega L_1 + \frac{1}{j\omega C_1} + R_1 + R_{\mathrm{s}} + jX_{\mathrm{s}}}, \tag{44}$$

with $\Delta K_{\mathrm{p}} = \Gamma_{\mathrm{p}}^2 / C_0$ and $\tau_{\mathrm{p}} = R_{\mathrm{L}} C_0$.

In order to form a resonator at the transmitter side, C_1 is determined by the relation $j\omega L_1 + (j\omega C_1)^{-1} = 0$, which results in

$$C_1 = (\omega^2 L_1)^{-1}, \tag{45}$$

then $Z_{\mathrm{in}} = R_1 + \Psi_{\mathrm{m}}^2 / Z_{\mathrm{M}}$. From (43), we have

$$\Re\{Z_{\mathrm{M}}\} = b + \Delta K_{\mathrm{p}} \frac{\tau_{\mathrm{p}}}{1 + (\omega\tau_{\mathrm{p}})^2}, \tag{46}$$

$$\Im\{Z_{\mathrm{M}}\} = Z_0 - \Delta K_{\mathrm{p}} \frac{\omega\tau_{\mathrm{p}}^2}{1 + (\omega\tau_{\mathrm{p}})^2}. \tag{47}$$

Let us choose the operating frequency such that

$$\Im\{Z_{\mathrm{M}}\} = 0, \tag{48}$$

the real and imaginary parts of the input impedance become

$$\Re\{Z_{\mathrm{in}}\} = R_1 + \frac{\Psi_{\mathrm{m}}^2}{b + \Delta K_{\mathrm{p}} \tau_{\mathrm{p}} (1 + (\omega\tau_{\mathrm{p}})^2)^{-1}}, \tag{49}$$

$$\Im\{Z_{\mathrm{in}}\} = 0. \tag{50}$$

The conditions for matching to the source impedance are

$$R_{\mathrm{s}} = \Re\{Z_{\mathrm{in}}\}, \tag{51}$$

$$X_{\mathrm{s}} = -\Im\{Z_{\mathrm{in}}\} = 0. \tag{52}$$

Under these circumstances, the input power is equal to the power available from the source, $P_{\mathrm{in}} = P_{\mathrm{avs}}$. Therefore, the two power gains collapse to the same solution, $\eta_{\mathrm{t}} = \eta_{\mathrm{p}} = \eta$. In addition, due to (52), the power available from the source takes the form $P_{\mathrm{avs}} = {V_{\mathrm{s}}}^2 / (8R_{\mathrm{s}})$.

The power delivered to the load is given by [70]

$$P = \frac{1}{2}\,\Delta K_{\mathrm{p}}\frac{\omega^2\tau_{\mathrm{p}}}{1+(\omega\tau_{\mathrm{p}})^2}F_0^2/ \\ \{[\,\overline{Z}+\Delta K_{\mathrm{p}}\frac{(\omega\tau_{\mathrm{p}})^2}{1+(\omega\tau_{\mathrm{p}})^2}]^2+[\omega b+\Delta K_{\mathrm{p}}\frac{\omega\tau_{\mathrm{p}}}{1+(\omega\tau_{\mathrm{p}})^2}]^2\} \tag{53}$$

where $\overline{Z} = j\omega Z = -\omega Z_0$, and the equivalent force is computed as

$$F_0 = \frac{\Psi_{\mathrm{m}}V_{\mathrm{s}}}{\sqrt{(R_{\mathrm{s}}+\Re\{Z_{\mathrm{in}}\})^2+(\Im\{Z_{\mathrm{in}}\})^2}} = \frac{\Psi_{\mathrm{m}}V_{\mathrm{s}}}{2R_{\mathrm{s}}}. \tag{54}$$

We can write

$$\begin{aligned}\overline{Z}+\Delta K_{\mathrm{p}}\frac{(\omega\tau_{\mathrm{p}})^2}{1+(\omega\tau_{\mathrm{p}})^2} &= -\omega[Z_0-\Delta K_{\mathrm{p}}\frac{\omega\tau_{\mathrm{p}}^2}{1+(\omega\tau_{\mathrm{p}})^2}] \\ &= -\omega\Im\{Z_{\mathrm{M}}\}=0,\end{aligned} \tag{55}$$

due to the equality in (48). From (53), (54), and (55), the power transfer efficiency reads

$$\begin{aligned}\eta &= \Delta K_{\mathrm{p}}\frac{\omega^2\tau_{\mathrm{p}}}{1+(\omega\tau_{\mathrm{p}})^2}\frac{\Psi_{\mathrm{m}}^2}{R_{\mathrm{s}}}[\omega b+\Delta K_{\mathrm{p}}\frac{\omega\tau_{\mathrm{p}}}{1+(\omega\tau_{\mathrm{p}})^2}]^{-2} \\ &= \frac{\Delta K_{\mathrm{p}}}{\omega b}\frac{\omega\tau_{\mathrm{p}}}{1+(\omega\tau_{\mathrm{p}})^2}\frac{\Psi_{\mathrm{m}}^2}{bR_{\mathrm{s}}}[1+\frac{\Delta K_{\mathrm{p}}}{\omega b}\frac{\omega\tau_{\mathrm{p}}}{1+(\omega\tau_{\mathrm{p}})^2}]^{-2}.\end{aligned} \tag{56}$$

We now consider a condition to match the output impedance Z_{out} to the load, $R_{\mathrm{L}} = Z_{\mathrm{out}}$, to further optimize η. From (45) and (52), it follows that

$$Z_{\mathrm{N}} = \frac{\Psi_{\mathrm{m}}^2}{R_1+R_{\mathrm{s}}} = \Delta K_{\mathrm{m}}\tau_{\mathrm{m}} \tag{57}$$

where we have introduced $\Delta K_{\mathrm{m}} = \Psi_{\mathrm{m}}^2/L_1$ and $\tau_{\mathrm{m}} = L_1/(R_1+R_{\mathrm{s}})$, which are analogous to the definitions of ΔK_{p} and τ_{p}, respectively. From (42), we have that

$$Z_{\mathrm{out}} = \frac{1}{\omega C_0}\frac{\sqrt{(Z_0/b)^2+(1+Z_{\mathrm{N}}/b)^2}}{\sqrt{(\Delta K_{\mathrm{p}}/(\omega b)-Z_0/b)^2+(1+Z_{\mathrm{N}}/b)^2}}. \tag{58}$$

Substituting Z_0 obtained from equations (47) and (48) into the fraction Z_0/b, we get

$$\frac{Z_0}{b} = \frac{\Delta K_\mathrm{p}}{\omega b}\frac{(\omega\tau_\mathrm{p})^2}{1+(\omega\tau_\mathrm{p})^2} = M_\mathrm{p}\frac{X^2}{1+X^2} \tag{59}$$

where $M_\mathrm{p} = \Delta K_\mathrm{p}/(\omega b)$ is an electromechanical figure of merit and $X = \omega\tau_\mathrm{p} > 0$. In the same manner, we can write $Z_\mathrm{N}/b = M_\mathrm{m}Q_\mathrm{t}$ where $M_\mathrm{m} = \Delta K_\mathrm{m}/(\omega b)$ and $Q_\mathrm{t} = \omega\tau_\mathrm{m} = \omega L_1/(R_1 + R_\mathrm{s})$. The parameter M_m can be considered as an electrodynamic figure of merit. Alternative forms of M_p and M_m expressed in terms of the coupling coefficients and the mechanical quality factor of the ME transducer, which are widely utilized in EH and WPT literature, are discussed in Section 2.9. Q_t is the effective quality factor of the transmitter coil, which takes both dissipative components R_s and R_1 into account. Setting the right hand side of (58) equal to R_L, we obtain

$$X = \frac{\sqrt{(M_\mathrm{p}\frac{X^2}{1+X^2})^2 + (1+M_\mathrm{m}Q_\mathrm{t})^2}}{\sqrt{(M_\mathrm{p} - M_\mathrm{p}\frac{X^2}{1+X^2})^2 + (1+M_\mathrm{m}Q_\mathrm{t})^2}}. \tag{60}$$

Denoting $X^2 = Y > 0$, equation (60) can be simplified as follows

$$(1-Y)[(1+M_\mathrm{m}Q_\mathrm{t})^2(1+Y)^2 - M_\mathrm{p}^2 Y] = 0. \tag{61}$$

One obvious solution from the first factor is $Y = 1$, in other words,

$$\omega\tau_\mathrm{p} = 1. \tag{62}$$

In this case, the equation to find ω is

$$2Z_0\omega = \Delta K_\mathrm{p}, \tag{63}$$

following (47) and (46); notice that Z_0 is also a function of ω, $Z_0 = Z_0(\omega)$.

The expression (56) now reduces to

$$\eta = \frac{\Psi_{\mathrm{m}}^2}{bR_{\mathrm{s}}}\frac{M_{\mathrm{p}}/2}{(1+M_{\mathrm{p}}/2)^2} = 2\frac{\Psi_{\mathrm{m}}^2}{bR_{\mathrm{s}}}\frac{M_{\mathrm{p}}}{(M_{\mathrm{p}}+2)^2} = 2M_{\mathrm{m}}Q_{\mathrm{s}}\frac{M_{\mathrm{p}}}{(M_{\mathrm{p}}+2)^2}. \quad (64)$$

where we define $Q_{\mathrm{s}} = \omega\tau_{\mathrm{s}} = \omega L_1/R_{\mathrm{s}}$, a non-dimensional parameter that is analogous to a quality factor. Q_{s} is an intermediate quantity used for further derivations. We note that the unloaded quality factor of the transmitter coil is characterized by $Q_1 = \omega\tau_1 = \omega L_1/R_1$. Due to the relations given in (49), (51) and (62), the ratio between Q_{s} and Q_1 can be written as

$$\frac{Q_{\mathrm{s}}}{Q_1} = \frac{R_1}{R_{\mathrm{s}}} = \frac{M_{\mathrm{p}}+2}{2M_{\mathrm{m}}Q_1+M_{\mathrm{p}}+2}. \quad (65)$$

From (64) and (65), η can be described in terms of three variables, the two figures of merit M_{m} and M_{p}, and the resonator unloaded quality factor Q_1,

$$\eta = \frac{2M_{\mathrm{m}}Q_1}{2M_{\mathrm{m}}Q_1+M_{\mathrm{p}}+2}\frac{M_{\mathrm{p}}}{M_{\mathrm{p}}+2}. \quad (66)$$

We would like to emphasize that $\{M_{\mathrm{m}}, M_{\mathrm{p}}, Q_1\}$ are solely dependent on the properties of the transmitter and receiver, and the expression (66) is the maximum power transfer efficiency with the optimal load that satisfies condition (62).

The other factor in (61) leads to the solution

$$\frac{Y}{(1+Y)^2} = \frac{(1+M_{\mathrm{m}}Q_{\mathrm{t}})^2}{M_{\mathrm{p}}^2}, \quad (67)$$

or equivalently,

$$\frac{\omega\tau_{\mathrm{p}}}{1+(\omega\tau_{\mathrm{p}})^2} = \frac{1+M_{\mathrm{m}}Q_{\mathrm{t}}}{M_{\mathrm{p}}}, \quad (68)$$

which results in

$$\omega\tau_{\mathrm{p}} = \frac{1 \pm \sqrt{1 - (2(1 + M_{\mathrm{m}}Q_{\mathrm{t}})/M_{\mathrm{p}})^2}}{2(1 + M_{\mathrm{m}}Q_{\mathrm{t}})/M_{\mathrm{p}}}. \tag{69}$$

This solution is real (and also positive) only if $M_{\mathrm{p}} \geq 2(1 + M_{\mathrm{m}}Q_{\mathrm{t}})$.

From (68) and (56), we get

$$\eta = M_{\mathrm{m}}Q_{\mathrm{s}}\frac{1 + M_{\mathrm{m}}Q_{\mathrm{t}}}{(2 + M_{\mathrm{m}}Q_{\mathrm{t}})^2}. \tag{70}$$

Substituting (68) into (51) yields

$$R_{\mathrm{s}} = R_1 + \frac{\Psi_{\mathrm{m}}^2}{b(2 + M_{\mathrm{m}}Q_{\mathrm{t}})}. \tag{71}$$

The relation between the quality factors Q_{t} and Q_1 is

$$\frac{Q_{\mathrm{t}}}{Q_1} = \frac{R_1}{R_{\mathrm{s}} + R_1} = \frac{2 + M_{\mathrm{m}}Q_{\mathrm{t}}}{4 + 2M_{\mathrm{m}}Q_{\mathrm{t}} + M_{\mathrm{m}}Q_1}, \tag{72}$$

which is equivalent to

$$M_{\mathrm{m}}Q_{\mathrm{t}}^2 + 2Q_{\mathrm{t}} - Q_1 = 0. \tag{73}$$

The positive solution to this quadratic equation is

$$Q_{\mathrm{t}} = \frac{\sqrt{M_{\mathrm{m}}Q_1 + 1} - 1}{M_{\mathrm{m}}}. \tag{74}$$

Therefore, $M_{\mathrm{m}}Q_{\mathrm{t}} + 1 = \sqrt{M_{\mathrm{m}}Q_1 + 1}$ and $(M_{\mathrm{m}}Q_{\mathrm{t}} + 2)^2 = (\sqrt{M_{\mathrm{m}}Q_1 + 1} + 1)^2$. The other is negative and not physical. Following the same procedure, we find that

$$Q_{\mathrm{s}} = \frac{Q_1}{\sqrt{M_{\mathrm{m}}Q_1 + 1}}. \tag{75}$$

Inserting (68), (69), and (74) back into (47) and (48), the operating frequency is then determined by the equation

$$\begin{aligned} 2Z_0\omega &= \Delta K_\mathrm{p}[1 \pm \sqrt{1-(2(1+M_\mathrm{m}Q_\mathrm{t})/M_\mathrm{p})^2}\,] \\ &= \Delta K_\mathrm{p}[1 \pm \sqrt{1-4(M_\mathrm{m}Q_1+1)/M_\mathrm{p}^2}\,]. \end{aligned} \quad (76)$$

Finally, we substitute Q_t and Q_s into (70) and obtain

$$\begin{aligned} \eta &= \frac{\sqrt{M_\mathrm{m}Q_1+1}}{(\sqrt{M_\mathrm{m}Q_1+1}+1)^2}\frac{M_\mathrm{m}Q_1}{\sqrt{M_\mathrm{m}Q_1+1}} \\ &= \frac{M_\mathrm{m}Q_1}{(\sqrt{M_\mathrm{m}Q_1+1}+1)^2}. \end{aligned} \quad (77)$$

We note that at the critical value when $M_\mathrm{p} = M_\mathrm{p}^* = 2(1+M_\mathrm{m}Q_\mathrm{t})$, $\omega\tau_\mathrm{p} = 1$ (i.e., see (69)), and the two cases collapse to a single solution. Furthermore, we can write the output impedance in (42) and its imaginary part as

$$Z_\mathrm{out} = \frac{1}{\omega C_0}\frac{jZ_0/b + (Z_\mathrm{N}/b+1)}{(M_\mathrm{p}-Z_0/b)+j(Z_\mathrm{N}/b+1)}, \quad (78)$$

$$\Im\{Z_\mathrm{out}\} = \frac{1}{\omega C_0}\frac{(Z_0/b)(M_\mathrm{p}-Z_0/b)-(Z_\mathrm{N}/b+1)^2}{(M_\mathrm{p}-Z_0/b)^2+(Z_\mathrm{N}/b+1)^2}. \quad (79)$$

With $\omega\tau_\mathrm{p} = 1$, based on (63), $Z_0/b = M_\mathrm{p}/2$ and $M_\mathrm{p} - Z_0/b = M_\mathrm{p}/2$. In addition, $Z_\mathrm{N}/b = M_\mathrm{m}Q_\mathrm{t}$. As a consequence, $\Im\{Z_\mathrm{out}\} = 0$, and the equation $R_\mathrm{L} = Z_\mathrm{out}$ is equivalent to $R_\mathrm{L} = \Re\{Z_\mathrm{out}\}$. This result shows that at $M_\mathrm{p} = M_\mathrm{p}^*$, the bi-conjugate impedance matching conditions

$$\begin{cases} Z_\mathrm{in} = Z_\mathrm{s}^*, \\ Z_\mathrm{out} = Z_\mathrm{L}^*, \end{cases} \quad (80)$$

are satisfied. Therefore, the expression (77) is the maximum possible efficiency that can be obtained by the ME WPTS under consideration. More importantly, this global optimum can also be achieved at any $M_\mathrm{p} > M_\mathrm{p}^*$. The previous solution, i.e., (66), with lower transfer efficiency applies for $M_\mathrm{p} < M_\mathrm{p}^*$.

We see that the efficiency in (77) is independent of the electromechanical figure of merit M_{p} and is only a function of the electrodynamic figure of merit M_{m} and the unloaded quality factor Q_1 of the transmitter. (Note, M_{m} embeds both the electrodynamic coupling factor and the mechanical quality factor of the ME receiver.) The independence of efficiency from M_{p} reflects the fact that when M_{p} reaches M_{p}^{*}, further improvements in the piezoelectric material properties will not result in more power output. The increased damping effect from higher electromechanical coupling (i.e. from the piezoelectric material) would reduce the amount of mechanical power available even though a higher percentage of that power would be converted to electrical power. Hence, both the output power and efficiency saturate for M_{p} going beyond M_{p}^{*}.

It should be noted that while $\Psi_{\mathrm{m}}, Z, \Gamma_{\mathrm{p}}$ and C_0 presented at the beginning of this Section are for a ME WPTS, the analysis and findings apply to a magneto-mechano-electric (MME) WPTS. This is true for translational [72], [73] or rotational [74] architectures with their corresponding parameters. In many practical scenarios, the internal impedance of a source $Z_{\mathrm{s}} = R_{\mathrm{s}} + jX_{\mathrm{s}}$ and the electrical load R_{L} are predetermined. In order to realize the general maximum power transfer theorem in [75], two additional networks (e.g., T– or Π–type) can be used as passive impedance matching circuits at both transmitter and receiver sides. A detailed analysis of the method is out of the scope of this work, but an example can be found in [76].

When the coupling between the transmitter coil and the ME receiver is weak, $M_{\mathrm{m}}Q_{\mathrm{t}} \ll 1$. Thus, the solution (69) is approximately $\omega\tau_{\mathrm{p}} \approx (M_{\mathrm{p}} \pm \sqrt{M_{\mathrm{p}}^2 - 4})/2$ with the condition $M_{\mathrm{p}} \geq 2$. This alternative expression of (69) along with (62) form the same

complete set of solutions to the power optimization problem for a ME WPTS presented in [70], Section 2.3. Therefore, *in the weak coupling regime, the efficiency maximization can be considered equivalent to optimizing the output power under an applied magnetic field*. Moreover, obeying the conditions (45) and (51) (now roughly $R_{\mathrm{s}} \approx R_1$) yields the maximum input power and the largest magnetic field that the transmitter coil can produce (for a given power source). Since the two problems are unified, we can also infer that the relationships between the transfer efficiency and frequency are identical to those of power and frequency obtained from optimizing the geometry of the ME transducer. For instance, under the condition of a constant mechanical quality factor, the efficiency is proportional to the chosen operating frequency, $\eta \propto \omega$. For the circumstances where $M_{\mathrm{m}} Q_{\mathrm{t}} \ll 1$, and correspondingly $M_{\mathrm{m}} Q_1 \ll 1$, the optimum transfer efficiency and output power are

$$\eta \approx \frac{1}{4} M_{\mathrm{m}} Q_1, \tag{81}$$

$$P \approx \frac{P_{\mathrm{avs}}}{4} M_{\mathrm{m}} Q_1. \tag{82}$$

Comparing (26) and (77), we see that despite the apparent differences in the energy conversion mechanisms, the optimal transfer efficiency of the two topologies, RIC and ME, essentially share the same form $\eta = \Theta/(\sqrt{1+\Theta}+1)^2$. The quantity Θ can be referred to as the figure of merit and receives different values depending on the WPT structure used. Especially, for weakly coupled systems, the maximum efficiency and output power are reduced to the forms $\eta \approx \Theta/4$ and $P \approx P_{\mathrm{avs}}\Theta/4$.

2.6 Experimental Validations: A Case Study for a Weakly Coupled RIC System

A RIC WPTS is implemented to experimentally validate a key finding in Section 2.2 that the maximum output power is proportional to the drive frequency squared at the weak coupling regime. The experimental setup is shown in Figure 2.10. The receiver coil is a 3 cm diameter 6–turn solenoid coil composed of 16 AWG (1.291–mm diameter) copper wire. A resonator is formed at the receiving side by connecting an external capacitor in parallel with the receiver coil. This configuration eliminates the effects of the parasitic capacitance (of the receiver), in which the effective capacitance is now a summation of the added capacitance and that parasitic capacitance. The frequency range of interest is within $(0, 250]$ kHz, which is also a typical operating frequency range of a ME WPTS. In this case, the frequency–dependent resistance of the coil (also known as AC resistance) is negligible [57]. Therefore, the coil series resistance can be considered constant and only contains a DC resistance. The transmitter coil is a 15.56 cm diameter 9–turn solenoid coil made of 16 AWG (1.201–mm diameter) copper wire.

The receiver is placed along the centerline of the transmitter and at a distance of 10 cm. The planes of both coils are in parallel (i.e., there is no misalignment). The squared coupling coefficient between the transmitter and receiver of the particular system under investigation is approximately $k^2 \approx 0.01\%$, obtained by COMSOL simulation. Since the coupling is weak, the transmitter coil acts as a pure magnetic field generator. An E&I 240L class A linear power amplifier was used to supply the transmitter coil with a high–frequency current. The **B**–field strength produced at the location of the receiver is measured by a MC110A magnetic field sensor (manufactured by Magnetic Sciences

Inc.). In order to reduce the complexity of the experimental process, we choose not to form a resonator at the transmitting side and normalize the maximum delivered power with the **B**–field squared instead. This approach does not affect the relationship between output power and frequency. The load resistance is varied to determine its optimal value and the corresponding maximum power at each drive frequency.

Figure 2.11 shows a comparison between the experimental data and a quadratic approximation of the form $y = ax^2$, where y is the normalized power P/B_0^2 and x is the frequency. The coefficient $a = 3.108 \times 10^{-3}$ is determined by MATLAB Curve Fitting Toolbox. The discrepancy between the measured and fitted quadratic curve is negligible, showing a quadratic dependence of the maximum output power on the drive frequency. This finding is consistent with the theoretical prediction.

Performing experimental validations for a RIC WPTS is straightforward by using different external capacitors to adjust the resonance frequency of a given receiver coil. However, the validation process becomes more complicated for a ME WPTS, which requires many ME composites fabricated with various geometric dimensions to attain different resonance frequencies. Manufacturing multilayer and multi–material ME transducers at a small scale is challenging. Therefore, the experimental study on the power–frequency relationship for ME devices is left open in this work. Since a complete model taking the dynamics of both the transmitter and receiver has been thoroughly validated by rigorous experiments [30], [77], the theoretical analysis in Sections 2.4 and 2.5 is still an appropriate framework for further investigations of other researchers in the field of ME WPT.

2.7 Discussion

The derivations presented in Sections 2.2 and 2.3 hold independently of the receiver and harvester structures. However, when the coil geometry is subject to change, the EMF amplitude V_0 and the coil series resistance R become functions of the number of turns N, the drive frequency ω, and the geometric dimensions. In the low– and intermediate–frequency ranges (e.g., up to a few hundreds of kHz), R slightly increases with ω and is approximately proportional to N [78]. Meanwhile, V_0 can be considered proportional to both N and ω. Therefore, P_{lim} (and P) almost always increases with N and ω, assuming that the other parameters such as the magnetic flux density B_0 and the surface area S are kept unchanged. Therefore, increasing the number of turns and the operating frequency is preferable. These characteristics are more important in energy harvesting systems that operate at very low frequencies, such as ones that scavenge magnetic energy from a power line [79].

On the other hand, R increases exponentially with ω in higher frequency bands (e.g., sub–MHz). A small change of N may lead to a substantial increase of the overall value of R due to the eddy current and the proximity effect [80]–[83]. Thus, considering the geometry optimization problem is essential under this scenario, especially when the volume or area is constrained. This concern is out of the scope of the chapter and is left open for further study.

The quadratic dependence of the maximum output power and efficiency on the drive frequency observed in Sections 2.2 and 2.3 is only valid in a frequency range in which the change of the coil series resistance with frequency is small. In order to emphasize this property, without loss of generality, we consider an example where two

identical spiral coils form a RIC WPTS. The relevant parameters and equations for computing the example are detailed in Section 2.9. The results are presented in Figure 2.12, showing the variation of the coil resistance R in terms of the operating frequency for a given coil geometry and the frequency response of the largest possible transfer efficiency of the considered RIC WPTS. In particular, for $f \leq 200$ kHz, R is nearly constant, and therefore, both P and η are proportional to ω^2. However, in a higher frequency range, R increases dramatically and causes a significant decrease in the Q–factors. As a consequence, P and η reduce with frequency.

The power and efficiency expressions presented in Sections 4 and 5 are valid when the demagnetization effects are negligible. For magnetostrictive materials with very high permeability, Metglas for example, the demagnetizing field could significantly decrease both the power and efficiency and thus cannot be ignored [84]. Maximizing transferred power and efficiency associated with the geometry optimization problem becomes much more complicated when taking the demagnetization phenomenon into account. Therefore, using numerical methods to find optimal solutions is more appropriate than analytical counterparts. However, it is essential to note that the presence of the demagnetizing field does not alter the relationship between power/efficiency and frequency, which is still linear with the assumption of a constant mechanical quality factor.

Human safety considerations are essential for WPTS used to provide power for biomedical implantable devices, regardless of their energy conversion mechanisms. The International Committee on Electromagnetic Safety (ICES, a subsidiary of IEEE) and ICNIRP have established safety standards for WPTS, especially for exposure to magnetic

and electric fields) [27]–[29]. In particular, ICES has regulated Dosimetric Reference Limits (DRLs) for RF shocks (defined in terms of the electric field) and SARs for thermal heating inside the human body. For instance, the limits of the SARs are 0.4 W/kg and 10 W/kg for the whole–body and localized exposures, respectively. Such restrictions are very challenging to measure or predict. Thus, Exposure Reference Levels (ERLs) have been introduced as an alternative. Most of the ERLs are defined as the maximum allowable magnetic flux density with respect to the wave frequency, making them much more convenient to assess. For example, the permissible **B**–field strength at 100 kHz is 100 μT while that at 6.78 MHz is 0.29 μT. Most importantly, the regulations based on ERLs are more conservative than those relied on SARs. In other words, a system complying with the ERLs also simultaneously satisfies the requirements of DRLs and therefore obeys the safety standards [85].

Up to this point, the relationship between a chosen operating frequency and the corresponding exposure reference level, and the relationship between the output power and an applied magnetic field, are relatively well–known. Exploring a direct dependence of power on frequency provides the last bridge connecting the triangle of power–frequency–magnetic field strength. The obtained properties could serve as simple and efficient tools to estimate, design, and optimize the performance of a WPTS, especially when subject to safety restrictions.

2.8 Conclusion

We discussed four scenarios with two central objectives, maximum output power, and optimum efficiency, for two wireless power transfer systems based on resonant

inductive coupling and magnetoelectric effects. We unified the power and efficiency maximization problems for each architecture in the weak coupling regime, in which we found that both schemes yield the same optimal load and frequency. We also resolved the differences in the energy conversion of the two mechanisms by expressing the power and efficiency in similar general forms, respectively. We revealed the quadratic dependence of both quantities (power and efficiency at their maximum) on drive frequency for a resonant inductive coupling system. In the case of a magnetoelectric configuration, these relationships become linear under a constant mechanical quality factor condition.

Although the two considered wireless power transfer techniques have been extensively studied in the literature, the findings presented in this chapter could provide a more insightful understanding of their performance. In addition, the results can be extended to other relevant systems that share similar physics, such as inductive energy harvesting or magneto-mechano-electric (sometimes referred to as electrodynamic) wireless power transfer. Therefore, the perspective and the approach we chose here could be beneficial to a wide variety range of fields.

2.9 Supplemental Information

2.9.1 Current and Magnetic Field Relationship of a Thick Coil with a Rectangular Cross Section

$$\Lambda_{\mathrm{H-I}} = \frac{H_0}{I} = \frac{1}{4\pi(z_2 - z_1)(r_2 - r_1)} \int_{r_1}^{r_2} \int_{\varphi_1}^{\varphi_2} \int_{z_1}^{z_2} \frac{(\tilde{r} - r\cos\tilde{\varphi})\tilde{r}}{(r^2 + \tilde{r}^2 - 2r\tilde{r}\cos\tilde{\varphi} + (z - \tilde{z})^2)^{3/2}} \tilde{r}\tilde{\varphi}\tilde{z}. \tag{83}$$

The geometric dimensions of a thick coil that carries an (effective) input current

of I are shown in Figure 2.13. The notations are defined as follows. r_1 (r_2) – the inner (outer) radius. z_1 (z_2) – the lower (upper) height. t_c – the total thickness of the coil, usually $z_1 = -z_2 = t_\mathrm{c}/2$. For the sake of simplicity, we assume that the ME transducer is in parallel with the centerline of the transmitter coil, hence $H_0 = H_\mathrm{z}(r, z)$. The parameter $\Lambda_{\mathrm{H-I}}$ is then given by equation (83) [86], where $\tilde{r}, \tilde{\varphi}$ and $\tilde{z}$ are the integration variables, $\varphi_1 = 0$ and $\varphi_2 = 2\pi$. This three-dimensional integral can be numerically computed by the function [*integral3*] in MATLAB. An alternative form of $H_0 = H_\mathrm{z}(x, y, z)$ expressed in the Cartesian coordinates can be found in [87].

2.9.2 Approximations of Electromechanical and Electrodynamic Figures of Merit

We first assume that the mechanical impedance Z in (34) can be approximated by a mass–spring systems $\{m, K_0\}$ such that $\omega m - K_0/\omega \approx Z(\omega)$ for all ω. The electrodynamic and electromechanical coupling coefficients are defined by [88], [89]

$$k_\mathrm{p}^2 = \frac{\Gamma_\mathrm{p}^2}{(\Delta K_\mathrm{p} + K_0)C_0} = \frac{\Gamma_\mathrm{p}^2}{\Gamma_\mathrm{p}^2 + K_0 C_0}, \tag{84}$$

$$k_\mathrm{m}^2 = \frac{\Psi_\mathrm{m}^2}{(\Delta K_\mathrm{m} + K_0)L_1} = \frac{\Psi_\mathrm{m}^2}{\Psi_\mathrm{m}^2 + K_0 L_1}. \tag{85}$$

The corresponding expedient coupling coefficients [90] (also known as generalized coupling coefficients [91]) are given by

$$k_{\mathrm{p,e}}^2 = \frac{k_\mathrm{p}^2}{1 - k_\mathrm{p}^2} = \frac{\Gamma_\mathrm{p}^2}{K_0 C_0}, \tag{86}$$

$$k_{\mathrm{m,e}}^2 = \frac{k_\mathrm{m}^2}{1 - k_\mathrm{m}^2} = \frac{\Psi_\mathrm{m}^2}{K_0 L_1}. \tag{87}$$

The electromechanical and electrodynamic figures of merit can be written

$$M_{\mathrm{p}} = \frac{\Delta K_{\mathrm{p}}}{\omega b} = \frac{\Gamma_{\mathrm{p}}^2}{C_0 \omega b} = k_{\mathrm{p,e}}^2 \frac{m\omega_0^2}{\omega b}, \tag{88}$$

$$M_{\mathrm{m}} = \frac{\Delta K_{\mathrm{m}}}{\omega b} = \frac{\Psi_{\mathrm{m}}^2}{L_1 \omega b} = k_{\mathrm{m,e}}^2 \frac{m\omega_0^2}{\omega b} \tag{89}$$

where $\omega_0 = \sqrt{K_0/m}$ and $K_0 = m\omega_0^2$. Usually, the operating frequency of a ME WPTS is close to the resonance frequency, $\omega \approx \omega_0$. Therefore, M_{p} and M_{m} are approximately

$$M_{\mathrm{p}} \approx k_{\mathrm{p,e}}^2 Q_0, \tag{90}$$

$$M_{\mathrm{m}} \approx k_{\mathrm{m,e}}^2 Q_0 \tag{91}$$

where $Q_0 = \omega m/b$ is the mechanical quality factor of the ME receiver at its resonance frequency.

2.9.3 Spiral Coil Modeling

While many different types of coil can be used for a WPTS, here we chose a spiral coil structure for the purpose of demonstration since the mathematical model for estimating its electrical properties, such as inductance and series resistance, is quite straightforward. Figure 2.14 shows the geometry of a spiral coil, in which d_{in} and d are the inner and outer diameters. The copper track thickness, width, and the spacing between two tracks are denoted as t_0, w, and s, respectively.

The equations to compute the coil inductance and total resistance are reported in [57] and summarized as follows.

$$d = 2(d_{\mathrm{in}}/2 + (n-1)s + nw),$$

$$\beta = (d - d_{\mathrm{in}})/(d + d_{\mathrm{in}}),$$

$$d_{\mathrm{L}} = (d + d_{\mathrm{in}})/2,$$

$$L = \frac{\mu n^2 d_{\mathrm{L}}}{2}\left[\ln\left(\frac{2.46}{\beta}\right) + 0.2\beta^2\right],$$

$$d_{\mathrm{avg}} = d - (w + s)n/2,$$

$$l_{\mathrm{c}} = \pi d_{\mathrm{avg}} n,$$

$$A_{\mathrm{c}} = w t_0,$$

$$R_{\mathrm{DC}} = \rho \frac{l_{\mathrm{c}}}{A_{\mathrm{c}}},$$

$$\delta = \sqrt{\frac{2\rho}{\omega\mu}},$$

$$R_{\mathrm{skin}} = R_{\mathrm{DC}} \frac{t_0}{\delta(1-\exp(-t_0/\delta))} \frac{1}{1+t_0/w},$$

$$R_{\mathrm{prox}} = \frac{R_{\mathrm{DC}}}{10}\left(\frac{\omega}{\omega_{\mathrm{c}}}\right)^2,$$

$$\omega_{\mathrm{c}} = \frac{3.1}{\mu_0}\frac{(w+s)\rho}{w^2 t_0},$$

$$R = R_{\mathrm{DC}} + R_{\mathrm{skin}} + R_{\mathrm{prox}}.$$

For copper conductors, the permeability is approximately $\mu \approx \mu_0$, where $\mu_0 = 4\pi \times 10^{-7}\ \mathrm{N/A^2}$ is the permeability of free space. R_{DC} represents the DC loss of the conductor. R_{skin} and R_{prox} are the frequency–dependent components of the resistance due to the skin and proximity effects, respectively. The summation $(R_{\mathrm{skin}} + R_{\mathrm{prox}})$ is also known as AC resistance, instantaneous resistance, or dynamic resistance. β is referred to as the fill–factor. δ is the skin depth. ρ is the resistivity of the material, $\rho = 1.68 \times 10^{-8}\ \Omega\mathrm{m}$ for copper at $20°\mathrm{C}$. l_{c} and A_{c} are the length and the cross–sectional area of the conductor, respectively. ω_{c} is the critical frequency at which current crowding begins to occur. A RIC WPTS formed by two identical coils is considered, hence $Q_1 = Q_2 = \omega L/R$. The number of turn of each coil is $n = 10$. The coupling coefficient between the transmitter and receiver is arbitrarily chosen as $k^2 = 1\ \%$. The particular

parameter values used are $d_{\text{in}} = 1$ cm, $w = 3$ mm, $s = 2w$ (the inductance of a circular spiral coil is accurately predicted with less than 8 % error for $s \leq 3w$), and $t_0 = 35$ μm (for standard plated printed circuit board).

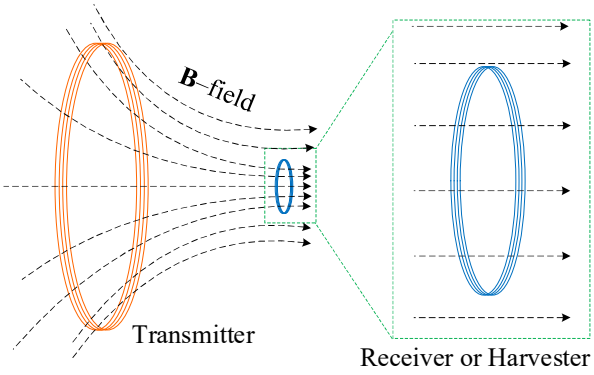

Figure 2.1 Concepts of a weakly-coupled wireless power transfer system and an inductive energy harvester.

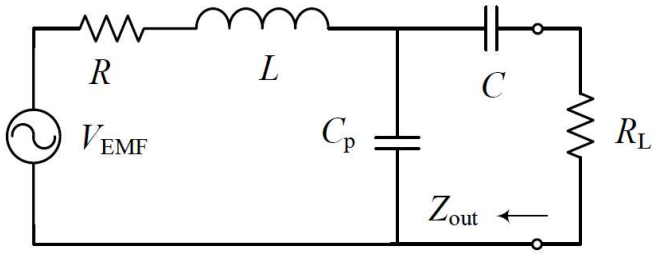

Figure 2.2: A general model of a coil resonator as a magnetic energy harvester or receiver.

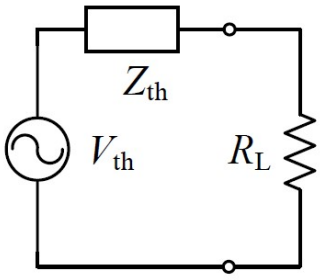

Figure 2.3: The'venin equivalent circuit.

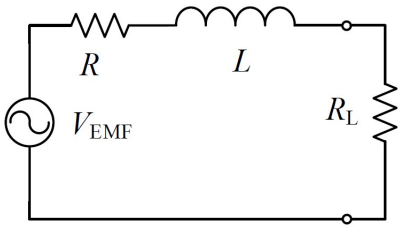

Figure 2.4: Simplified model for low frequency operation.

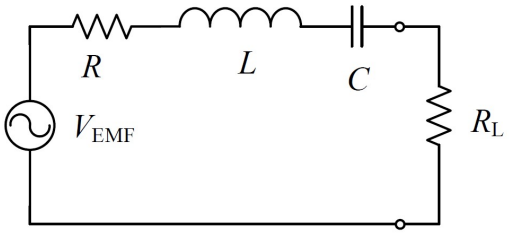

Figure 2.5: Simplified model for intermediate frequency operation.

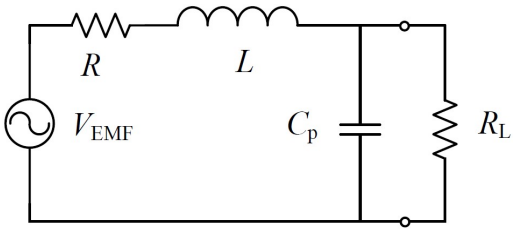

Figure 2.6: Simplified model for high frequency range.

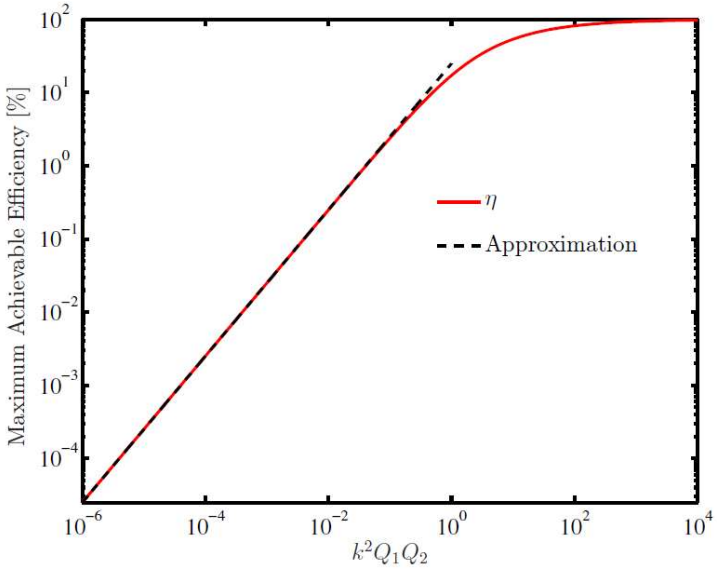

Figure 2.7: Maximum achievable transfer efficiency in percentage of a RIC WPTS with respect to a figure of merit $k^2Q_1Q_2$.

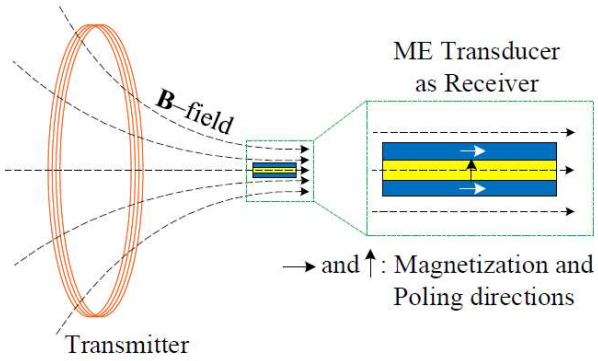

Figure 2.8: Concept of a magnetoelectric-based wireless power transfer system.

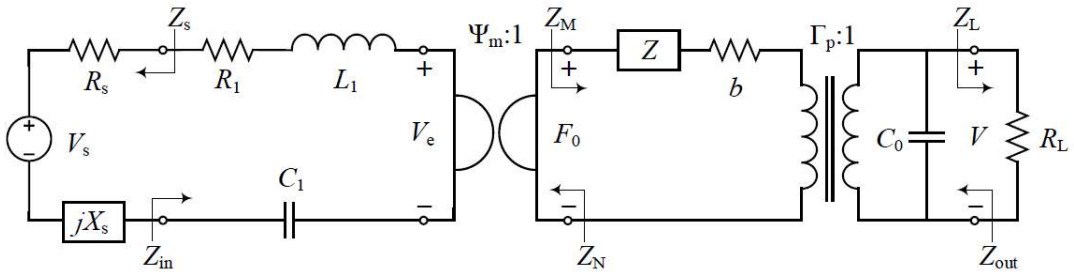

Figure 2.9: A complete model of a ME WPTS.

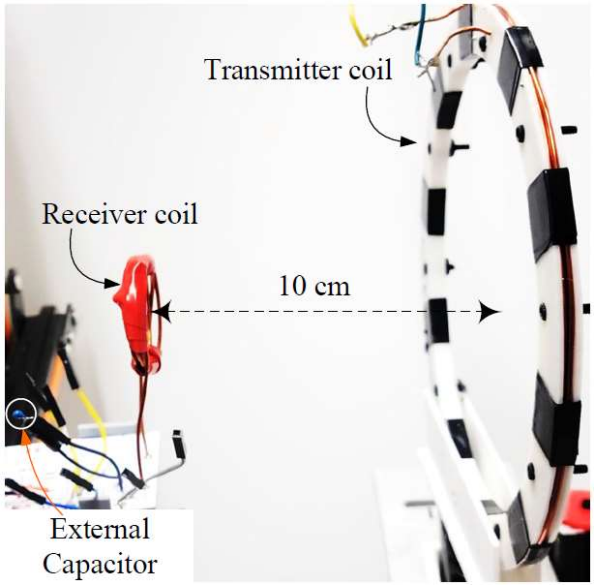

Figure 2.10: Experimental setup of a weakly–coupled inductive wireless power transfer system.

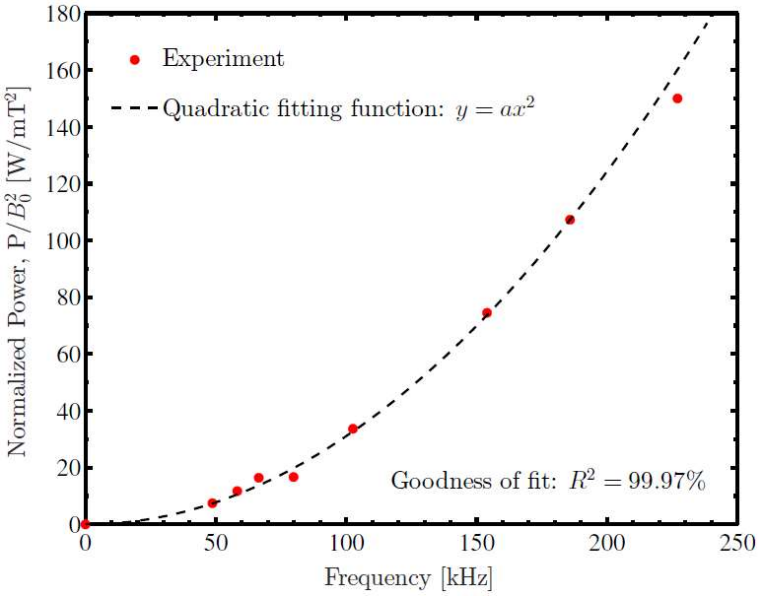

Figure 2.11: Maximum transferred power with respect to drive frequency.

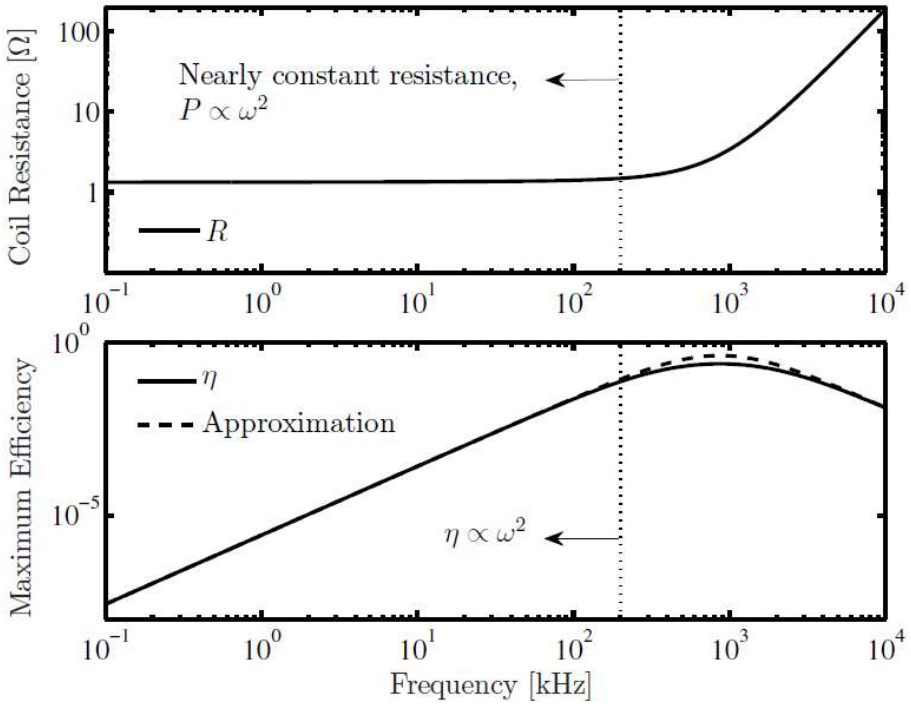

Figure 2.12: An example of the dependence of the coil series resistance and maximum transfer efficiency on the drive frequency.

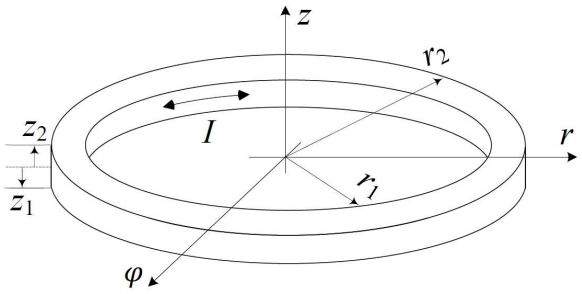

Figure 2.13: Geometry of a thick coil carrying a uniform current density. Here, I is the effective current flowing in the coil.

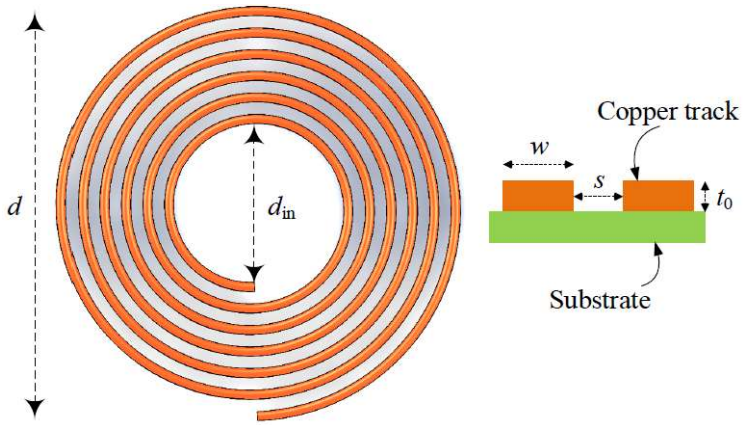

Figure 2.14: Geometry and parameter definitions of a spiral–shaped coil.

CHAPTER 3

OPTIMAL TRANSMIT COIL DESIGN FOR WIRELESSLY POWERED BIOMEDICAL IMPLANTS CONSIDERING MAGNETIC FIELD SAFETY CONSTRAINTS

This chapter is on developing an optimal design process that maximizes the B-field at the receiver while considering B-field exposure limits, transmitter size, and transmitter power constraints. I would like to acknowledge the work of Curtis Casados for his help in running the experimental verification and Binh Duc Truong for his help as an advisor.

3.1 Introduction

Human safety considerations must be paramount in any WPTS for biomedical implants, including ME and resonant inductive coupling (RIC). This safety concern is why optimal design rules of other WPTS cannot be generally applied to WPTS that operate near or within the human body. The safety standards are shown in Figure 1.3,

which is reshown here for ease of reference. As the frequency of the WPTS increase, the allowable B-field decreases except for some regions in the Hz and kHz frequency range. For example, according to [27], [28], the allowable magnetic flux density (B-field) at 100 kHz is 100 μT compared to 0.29 μT at 6.78 MHz. Therefore, there is an incentive to explore methods to achieve WPT with very small receivers that operate efficiently at lower frequencies. Especially for systems that can operate near the 100 kHz corner frequency range.

ME WPTS at mm to cm size scales naturally operate in the low kHz frequency range. Most small ME transducers' mechanical resonance is on the order of 100 kHz. An illustration of a ME WPTS is shown in Figure 3.1. A ME transducer is utilized as a receiver, which converts a magnetic wave produced by a transmit coil to electrical power to supply a biomedical implant. The operation principle of a ME receiver was thoroughly investigated in [77]. The authors showed that the maximum possible power that can be delivered to a load P_{avt} is proportional to the square of the magnetic field amplitude H_0. In particular,

$$P_{avt} = \frac{1}{8}\frac{(\Gamma_m H_0)^2}{b} \tag{92}$$

where Γ_m is the electrodynamic transduction factor and b is the mechanical damping coefficient. Γ_m is a function of the geometry and material parameters of the ME transducer. Meanwhile, b is solely dependent on the mechanical properties of the receiver. For a given receiver structure implanted inside the human body, both Γ_m and b are determined ahead of time. Therefore, maximizing P_{avt} by optimizing H_0 generated at the implant location (which can be accomplished by an appropriate design of the transmitter geometry) is of great interest to study.

The optimal design problem is to design the transmit coil to maximize the magnetic field at the location of the implant, subject to design constraints, while ensuring the magnetic field exposure is below the safety constraint at any point inside the human body. For instance, if the implant is 10 mm below the surface of the skin, one would seek to design a transmitter that maximizes the magnetic field at 10 mm below the surface of the skin while ensuring that the magnetic field at the surface of the skin (or anywhere else inside the body) is below the limits of the relevant safety standard. The idea behind this approach is that by determining the maximum achievable B-field at the implant, the designer can then design a receiving transducer to achieve the required power from this magnetic field.

An alternative approach would be to first design the receiver, and then determine the required B-field that will provide adequate power. The analysis presented in this chapter is reversible such that the equations developed could also be used for this alternative approach. While this chapter focuses on ME WPTS, a similar analysis can be extended to an inductive coupling WPTS. In general, increasing the B-field at the receiver will increase the maximum power that can be delivered to the load. We also note that, when designing a RIC WPTS, other relevant parameters such as system coupling, resonance, coil quality factor, and impedance matching should be considered. These factors are out of the scope of this chapter because, unlike ME WPTS, it may not be safe to assume that the transmitter dynamics can be decoupled from the receiver because of the potentially higher coupling between the transmit and receiver coils in some RIC WPTS. Thereby designing the optimal transmit coil that maximizes power delivered to the load no longer solely depends on maximizing the B-field at the receiver. However, for

RIC WPTS with weak coupling, ($k^2 Q_1 Q_2 \ll 1$), these parameters may be less relevant and the analysis in this chapter may be more directly applicable.

For a ME WPTS, it is indicated that the optimal coil diameter that maximizes the transferred power depends upon the distance between the transmit coil and the ME receiver [30]. A bigger coil is more suitable for a large transfer range in general, and a smaller transmitter is preferable for a close distance. However, this argument may no longer hold when subject to the safety standards and systems constraints, which the authors have not considered. Furthermore, universal rules to design an optimal transmitter have not been revealed yet.

In an implantable system, it is likely that the receiver is much smaller than the transmitter, and the distance between them is much larger than the size of the receiver. These unavoidable mismatches result in a weak coupling. Therefore, WPTS used in biomedical applications typically have a low transfer efficiency, which is usually less than 1 %. For instance, the overall efficiency of the system reported in [77] was only 0.12 %. Thus, the impedance reflected onto the transmit coil from the ME transducer can be disregarded. Additionally, if the operating frequency is low enough, the receiver is potentially much smaller than the electromagnetic wavelengths (e.g., at 1 GHz the EMF wavelength is 30 cm). These assumptions allow us to optimize the transmitter geometry without taking into account the appearance of the receiver; in other words, the transmitter can be considered purely as a magnetic field source.

With a focus on supplying low-power bioelectronics, we treat the actual power delivered to the load as the key metric of a ME WPTS. In this chapter, the central objective is to generalize design rules to attain a desired transmit coil. The questions on

optimizing the overall transfer efficiency or designing a fully optimal system are left open for further investigation.

This chapter proceeds as follows. The motivations and central objectives of the work are given in the Introduction. Optimal transmitter designs considering only safety constraints are then explored. Further design constraints are then incorporated. These constraints include transmit coil size and placement constraints, and transmit current constraints. A case study is presented in which optimal transmit coils (for ME-based WPTSs) are designed and experimentally validated. Next is a discussion of generalized design principles and an optimal design process. And finally the concluding sections further discuss alterations on the constraints, such as needing a minimum air gap between the transmit coil and the skin, and how constraining power instead of current affects the optimal design process.

3.2 Transmit Coil Optimization

Due to its ease in manufacturing and well described magnetic wave propagation properties, solenoids are often chosen as the geometry for electromagnets. For a solenoid based transmit antenna, the B-field at a WPT receiver attached to a biomedical implant located inside a human body is dependent upon the following factors: (i) The distance into the body of the implant, $Z_{implant}$; (ii) The input current density, J; (iii) The coil thickness, t; (iv) The inner and outer radii, r_1 and r_2, respectively; and (v) The gap between the transmit coil and the skin, b, [86]. The definitions of these parameters are shown in Figure 3.2. The B-field is considered a function of current density, i.e. current per area, instead of the actual current. This alternative is convenient to generalize the

design of the solenoid transmitter. For example, a 10 turn solenoid with a 1 amp of RMS current is equivalent to a 1 turn solenoid with 10 amps of RMS current in terms of the field generated, assuming the radii of the two solenoids are equal. However, the quality factor, *Q*-factor, of each transmit coil will be different, which can affect the overall transfer efficiency of the system. Nonetheless, the available power at the receiver of the two cases are identical since the corresponding B-field strengths at the receiver are equal in principle.

The objective is to maximize the power that can be transferred to an electrical load, which correlates to maximizing the B-field at the biomedical implant without violating a magnetic field safety limit. Hence, the constrained optimization problem becomes

$$\begin{aligned} &\max B(r_1, r_2, t, b, z, J) \; at \; z = Z_{implant} + b \\ &s.t. \quad B(r_1, r_2, t, b, z, J) < B_{safe} \; \forall \; Z_{body}. \end{aligned} \tag{93}$$

Solving the optimization problem in this form involves calculating the B-field produced by a solenoid which is given by

$$B = \frac{\mu}{4\pi} \iiint_V \vec{j} \, d\tilde{v} \wedge \frac{\vec{r} - \overrightarrow{r'}}{\left|\vec{r} - \overrightarrow{r'}\right|^3} \tag{94}$$

where $\vec{j}$ is the current density, and $\vec{r} - \overrightarrow{r'}$ is a space vector between a point where the magnetic field is calculated and a location inside the solenoid conductor.

Generally, for any point, (94) may necessitate evaluating elliptical integrals. Therefore, the problem was solved numerically using gradient-based optimization algorithms subjected to a safety limit constraint. Through this numerical optimization, several trends quickly emerge. As expected, there is always an ideal alignment between

the solenoid and the biomedical implant, in which the receiver lies along the coil center axis. The optimal thickness, t, and the difference between the inner and outer radii, $r_2 - r_1$, are much smaller than the inner radius of the coil. The optimization pushes the design of the solenoid transmit coil to closely resemble a current loop. Using this insight, the governing equations for calculating the B-field for the solenoid along its z-axis can be simplified to

$$B = \frac{\mu}{4\pi} \frac{2\pi R^2 I}{(z^2 + R^2)^{\frac{3}{2}}} \tag{95}$$

where *B* is the B-field produced along the centerline at some distance *z* away by a current loop with a radius *R,* and current *I*, operating in some space with magnetic permeability μ. For human tissue, the magnetic permeability is equal to that of free space [92]. Equation (95) will be shown to be a good approximation for the solenoid magnetic field when compared with (94), COMSOL simulations, and an experimentally measured solenoid B-field in Section 3.3 on model validation.

3.2.1 Unconstrained Wireless Power Transmitter Optimization

The maximum achievable B-field at a point located $Z_{implant}$ distance inside the body, B_{max}, can be represented as

$$\mathrm{B_{max}} = \Gamma \mathrm{B_{safe}} \tag{96}$$

where B_{safe} is the maximum safe exposure limit, and Γ is a ratio less than or equal to one. If the B-field were completely uniform along the z-axis (see Figure 3.2), Γ would be equal to 1 and B_{max} would be as high as it is allowed by the safety standard. If there are no constraints placed upon the size or power consumption of the transmit coil, the

optimization process does in fact result in a transmit coil that emits a near-uniform magnetic field along the z-direction just under the imposed safety constraint (i.e., $\Gamma \approx 1$). In order to create this nearly uniform B-field, the transmit coil is tremendously large, with the radius of the coil much greater than the depth of the biomedical implant, and uses extremely high currents. However, this solution represents a highly idealized case that is unrealistic for practical design situations where available space and power are not infinite.

Therefore, this chapter will examine how the optimal design of the transmit coil for a WPT system is affected by both magnetic field safety constraints and either geometric/size constraints or power/current constraints. This investigation will provide useful insights into design rules for optimizing the achievable power at a biomedical implant without exceeding the magnetic field safety limit. The solutions to the constrained optimization problem differ significantly from the unconstrained case. The optimal design no longer produces a uniform magnetic field. The optimal B-field shape differs based upon the given constraints.

3.2.2 Geometrically Constrained Transmitter Optimization

Given the fact that the optimal transmit coil design resembles a current loop with the B-field described by (95), the geometric constraints consist of a constraint on the maximum radius of the coil, R, and the minimum and maximum distance that the coil can be placed from the skin, b. If geometric constraints are imposed, the solution to the optimization problem yields an optimal coil design whose radius is equal to the geometric constraint: R is as large as the constraint will allow. As the minimum distance constraint

is active, the air gap between the transmit coil and the skin should be minimal. Assuming that the transmit coil can be placed right at the skin (i.e., $b = 0$), the required current in the optimal transmit coil is

$$I = B_{safe}\frac{2R}{\mu} \tag{97}$$

where the radius R of the coil is equal to the geometric constraint limit, and μ is the magnetic permeability of the human body, which can be considered to be identical to that of free space. Equation (97) is derived using (95) and solving for the current that would result in a magnetic field at the safety limit at z = 0, or at the skin.

One interesting result of this optimization process is that the air gap should always be minimized. In other words, it is never beneficial to increase the air gap as it simultaneously requires an increase in the operating current of the transmit coil to compensate for the B-field at the implant location. The justification for this result is seen by examining the shape of the B-field produced by a current loop. Taking the derivative of (95) with respect to z yields

$$\frac{dB}{dz} = -\frac{\mu}{4\pi}\frac{6\pi R^2 I}{(z^2 + R^2)^{\frac{5}{2}}}z. \tag{98}$$

Equation (98) shows that the slope of the B-field is always negative, and the most significant drop in B-field occurs close to the transmit coil. This principle is indicated in Figure 3.3, in which the B-field amplitude and its derivative in terms of the distance are presented for three coils with different radii. It should be noted that the corresponding optimal current of each coil is used. The B-field of the different sized coils falls at different rates depending on the radius of the coil. The smallest coil has a B-field with a high initial negative slope, while the largest coil B-field has a much lower initial slope.

The slope of the B-field is always negative and initially becomes more negative before flattening out and approaches zero at large distances. It is impractical to operate in the area where the slope is level, since this property occurs at distances much larger than the radius of the coil and would require very high currents. As analyzed in the previous section, such a method can only be implemented when the coil geometry and input power are not constrained, which are unfeasible.

It is desirable to minimize the air gap as much as possible (ideally, $b \longrightarrow 0$). However, a non-zero small air gap may be necessary for some realistic circumstances. For many large coils, the magnetic field near the coil windings is stronger than that in the coil center. Depending on the input current, this phenomenon could cause B-field strengths at a small space near the coil windings to exceed the safety limit. If these scenarios take place, (94) can also be used to find the distance at which the B-field no longer violates the safety standard. The obtained value can be considered as the minimum required air gap. Section 3.5 outlines how the optimal design rules are modified when a non-zero constraint on the air gap is essential.

The optimal design of the transmitter is a solenoid with its radius equal to the size constraint (i.e. maximum allowed), the air gap minimized to zero, and the excitation current is determined by (97). For this configuration, the maximum B-field at the implant, B_{max}, can be determined by solving (95) with $z = Z_{implant}$. Making use of (97) to define the B-field safety limit, B_{safe}, and referring back to (96), the ratio between B_{max} and B_{safe} can be derived as

$$\Gamma = \frac{B_{max}}{B_{safe}} = \frac{R^3}{\left(Z_{implant}^2 + R^2\right)^{\frac{3}{2}}}. \qquad (99)$$

Furthermore, if the radius of the transmit coil is written in terms of a constant, a, multiplied by the implant depth,

$$R = aZ_{implant}, \tag{100}$$

(99) is reduced to

$$\Gamma = \frac{a^3}{(1+a^2)^{\frac{3}{2}}}. \tag{101}$$

If the geometric radius constraint is framed in this sense (i.e., the maximum allowable coil radius is a times the depth of the implant), then (101) can be utilized to compute the maximum possible fraction of the safety limit for a given radius constraint. A demonstration of (101) is shown in Figure 3.4. As a summary, (101) defines the maximum achievable magnetic field for any implant depth solely as a function of the geometric constraint.

Additionally, this process is reversible. If a particular magnetic field strength is required at the biomedical implant, (99) or (101) can be used to determine the minimum size coil that will produce the required magnetic field without violating the safety limit. For example, if the safety limit is 200 μT (IEEE standard for a 100 kHz magnetic field), and the necessary B-field for successful wireless powering of the implant is 150 μT (i.e., $\Gamma = 0.75$), then the transmit coil radius must be at least equal to 2.2 times the depth of the biomedical implant.

3.2.3 Current Constrained Optimal Transmitter

Attention is now turned to the case in which the electrical current serves as the design constraint, rather than the coil radius and placement (i.e., geometry). The goal of

the optimization problem is to find the current and radius combination that maximizes the B-field at the implant. As we expected, it is always the case that the optimal current is at the constraint, which is the maximum allowed. If we assume that the coil is placed as close to the skin as possible, the coil radius becomes the only remaining design parameter. The optimal coil radius is dependent on the given current constraint, the magnetic field safety limit, and the depth of the biomedical implant.

When performing the optimization algorithm, subject to the current and safety constraints, we observed an important phenomenon. The optimal radius of the transmitter was either constant or a linear function of the implant depth $Z_{implant}$. This behavior appears for any given set of the current constraint and safety limit. The distance at which the optimal radius changes its tendency is referred to as critical distance, Z_{crit}, as defined in Figure 3.5 (a). The numerical results are illustrated in Figure 3.5 (b), which shows the optimal coil radius in terms of $Z_{implant}$ for different current constraints. It is essential to point out that Z_{crit} obtains the value of $Z_{implant}$ at which the constant-optimal-radius line (parallel with the *x*-axis) intersects with the function $R = \sqrt{2}Z_{implant}$. In addition, Z_{crit} is dependent upon the current and B-field safety constraints. For instance, $Z_{crit} = 1.1$ cm for a current constraint of 5 A and $Z_{crit} = 3.3$ cm for 15 A. The magnetic field safety limit is 200 μT for both examples.

As shown in Figure 3.5, if $Z_{implant} \geq Z_{crit}$, the optimal radius is

$$R_{opt} = \sqrt{2}Z_{implant}. \qquad (102)$$

At the critical point, $Z_{crit} = Z_{implant}$, the optimal radius in (14) can be rewritten as

$$R_{opt} = \sqrt{2}Z_{crit}. \qquad (103)$$

Furthermore, when $Z_{implant} \leq Z_{crit}$, the optimal radius of the transmit coil is a constant (independent of $Z_{implant}$). Therefore, the relation in (103) holds for all $Z_{implant} \in [0, Z_{crit}]$. In this range of the implant depth, R_{opt} is dependent on both the current constraint and the safety limit. By substituting the electrical current constraint, I_{max}, into (97), R_{opt} is obtained as follows

$$R_{opt} = \frac{\mu I_{max}}{2B_{safe}}. \qquad (104)$$

From (104) and (103), the closed form expression of the critical distance is given by

$$Z_{crit} = \frac{1}{2}\frac{\mu I_{max}}{B_{safe}\sqrt{2}}, \qquad (105)$$

It is important to note that Z_{crit} is not an independently chosen parameter, but rather is a function of the magnetic field safety limit and current constraint. Z_{crit} plays an essential role in the design process as it represents the distance at which the optimal design path of the transmitter changes.

In order to further gain insight into the origins of (102) and (103), we now consider these two cases analytically. In either circumstance, the optimal radius is equal to a distance multiplied by the square root of two. The reason for this fact can be examined by looking at the optimization problem with and without the safety concern. If there is no magnetic field safety limit, but only a current constraint, the optimization problem is simplified. Once again, the maximum B-field occurs when the current constraint is active. The optimal radius can be found by setting the derivative of (95) with respect to the radius, R, equal to zero, which yields

$$\frac{dB}{dR} = \frac{2\pi 10^{-7} I\left(2Rz^2 - R^3\right)}{\left(R^2+z^2\right)^{\frac{5}{2}}} = 0. \qquad (106)$$

Solving (106) for R gives

$$R = \sqrt{2}\, z. \qquad (107)$$

With the goal of maximizing the B-field at $z = Z_{implant}$, (107) is identical to (102). In that sense, (102) is equivalent to the optimal design of a current constrained transmitter without regard to the magnetic field safety limit, or if the magnetic field safety constraint is not active for a given system. It should be noted that the solution to (102) results in a unique radius for every different implant depth, $Z_{implant}$. However, using (102) for all current constrained WPTS could violate the safety constraint in some circumstances, specifically at shallow depths. In these situations, there is a single optimal coil design for which the current is equal to the constraint and the radius of the coil is set such that the B-field is just under the safety limit at the skin. (104) shows the optimal coil radius for this scenario. In this regard, Z_{crit} represents the distance at which the safety constraint switches from being active at the skin to be being non active.

It is useful to analyze the two different modes of operation in the investigation of the optimal coil radius by looking at a specific example. These modes are illustrated in Figure 3.6, in which the current constraint is set at 10 A, and the maximum achievable B-field, B_{max}, is expressed as a function of the coil radius for different implant depths starting at $Z_{implant} = 0$ (i.e., the implant is right at the skin). The safety constraint for this example is 200 μT, $B_{safe} \leq 200$ μT. We note that if $Z_{implant} = 0$, the safety limit is reached for a coil radius of 3.16 cm. The B-field at the location of the implant, which is also at the surface of the skin, is 200 μ T ($\Gamma = 1$). As the depth of the implant becomes larger, B_{max} decreases. Taking $Z_{implant} = 1\ cm$ for example, $B_{max} = 173$ μ T. The optimal radius is still 3.16 cm since the magnetic field at the surface of the skin is still

200 μT ($\Gamma = 0.875$), and any further decrease in coil radius would violate the safety constraint. However, if $Z_{implant}$ is between 2 and 3.5 cm, the shape of the B_{max} curve changes. The optimal coil radius is now not only a function of the safety limit, but also a function of the implant depth. This is due to the fact that the safety constraint is no longer active. In other words, the coil radius that results in the highest B_{max} does not produce a B-field at or beyond the safety limit anywhere within the body. For this example, the delineation between these two regimes, the safety constraint being active or not active, is at $Z_{implant} = 2.2$ cm, which distance is equal to Z_{crit} calculated using (105).

If a certain Γ or B-field at the implant is required, the process of finding the minimum current is identical to the procedure outlined in the previous section, since the minimum coil radius that provides a certain Γ also requires the least current. The desired coil radius can be calculated using (101) and the corresponding minimum current can be achieved by (96).

3.3 Model Validation and Case Study

In order to validate the mathematical models and design insights, two transmit coils were constructed whose parameters are listed in Table 3.1. In order to reduce environmental impacts on the B-field, the coils were mounted to a support that raised the coils 21 cm above the lab table. The support was made of customized 3-D printed ABS plastic parts and aluminum beams and screws, as depicted in Figure 3.7.

Each transmitter was supplied with 15 A of RMS current at 80 kHz, and the B-field along each centerline axis was measured and recorded using a MC110A magnetic field sensor (Magnetic Sciences Inc.). A frequency of 80 kHz was chosen to minimize

sensor error in the measurements. The sensor was mounted on a modified 3-D printer which moved the sensor along the centerline of the coil's z-axis, as seen in Figure 3.7. Magnetic field readings were taken every 2 mm. In Figure 3.8, the experimentally measured B-field using the MC110A sensor, the simulated B-field using both (94) (numerical) and (95) (analytical) solved using MATLAB, and a COMSOL 5.3a simulation for each coil along its z axis are compared. In the COMSOL simulation, the copper wire coils were modeled in air using the dimesions given in Table 3.1 in a 2D axisymmetric model. Using the magnetic field physics solver with a "finer" mesh, the coils were excited by 15 A RMS current at 80 kHz and the magnetic field was measured along the coils centerline.

The experimental data match closely with those predicted by equations and simulations for both coils, generally within 5% error. The error of the MC110A sensor is listed at 5%, which explains these small discrepancies. The close agreement between the mathematical models and the COMSOL finite element analysis gives confidence in the assumption that (95) is valid for determining the B-field for solenoid transmitter. This lends creditability to optimization rules that were derived in the previous sections using these models. The experiments were conducted in air since the magnetic properties of tissue are almost identical to that of free space at low frequencies [6], [11], [93].

The optimal design rules for transmit coils proposed in this chapter can be explored through a case study, in which the implant distance, $Z_{implant}$, is 3 cm, 4 cm and 5.5 cm. The transmitter has both size and power constraints. In particular, it must be capable of being handheld (coil radius under 20 cm) and has a current limit of 15 amps (RMS). The operating frequency of the transmitter is (arbitrarily) chosen as 73 kHz and,

as such, the B-field cannot exceed the IEEE safety limitation of 200 μT. At low frequencies, the attenuation of an applied B-field due to traveling through human tissues is negligibly small. Additionally, it is assumed that the coil can be placed right at the skin.

With the B-field safety limit given, $B_{safe} \leq 200\ \mu T$, the next step is to determine if the size or current is the limiting constraint. We first set the radius equal to the constraint, $R = 20\ cm$, and use (97) to calculate the required current, which leads to $I = 67.3$ amps. Meanwhile, the design constraint is 15 amps, hence the current constraint will be the limiting factor. Now (102) - (105) are utilized to determine the optimal radius of the transmitter. Solving (105) for this system yields a Z_{crit} of 3.33 cm, meaning that the first implant at 3 cm is located at a distance less than Z_{crit} while the second and third implant distances, 4 and 5.5 cm, are greater than Z_{crit}. Setting $I = 15$ amps and using (103), the optimal radius for the first implant is 4.71 cm. For the latter two implants, (102) results in the optimal radii of 5.66 and 7.78 cm, respectively.

Using (95), the B-field for each of the three solenoid coils with the aforementioned radii were presented in Figure 3.9. The smallest coil produced the highest B-field for any point up to Z_{crit}, including the first implant depth of 3 cm. We note that the safety constraint is active only for the smallest coil for which $Z_{implant} < Z_{crit}$.

Beyond 3 cm, the coils with the larger radii supplied higher B-fields at the larger implant distances. In particular, the B-field of the largest coil (7.78 cm radius) is the greatest at the 5.5 cm distance. The coil with the 5.65 cm radius produced the highest B-field at the implant distance of 4 cm. However, it generated a B-field smaller than that of (i) the 4.71 cm radius coil for distances under Z_{crit} and (ii) the 7.78 cm coil for distances

near the 5.5 cm implant. All coils maintained a B-field under the safety limit of 200 μT at every point along the z-direction. It is noted that the coils in Table 3.1 are the optimally designed coils for implants located at 4 and 5.5 cm. All three coils were built and experimentally shown that they maximized the B-field at their respective implant depths. As mentioned in Section 1.3, at low frequencies, the electric field is usually the limiting constraint. However, since the considered system does not violate the ERLs limit (defined in terms of the magnetic field), it does not violate the electric field DRL either [29]. This result was verified in a COMSOL simulation of the coil's electric field.

3.4 Design Considerations and Design Process

The optimal design study and case study lead to the following three step generalized design process, which is illustrated graphically in Figure 3.10.

1. Define system constraints
    a. Determine desired operating frequency of the WPTS based on system parameters and operating requirements. Based on chosen frequency, find the magnetic field safety limit according to the chosen standard, IEEE or ICNRP [27]–[29].
    b. Define either the geometric and/or current constraints for the WPTS based on the requirements of the operational scenario.
2. Determine limiting constraint and set the corresponding design parameter at the maximum allowable value
    a. If there is only one constraint, that constraint is the limiting constraint.
    b. If there are multiple constraints, set the radius equal the design

constraint and calculate the required current using (97). If that current is below the current constraint, the radius constraint is limiting. Otherwise, the current is the limiting constraint.

c. If there are no constraints other than the magnetic field safety limit, the optimal solution is to make a giant coil that produces a uniform B-field in the axial direction. This, however, is unlikely to be realistic.

3. Solve for the optimal parameter(s) that are not the limiting constraint
    a. In all cases, minimize the air gap between the transmit coil and the subject body. If the air gap cannot be zero or close to zero, see Section 3.5 for optimal design equations for a non-zero air gap.
    b. If the transmit coil radius is the limiting constraint, use (97) to determine the required current. Use (95) to calculate the corresponding maximum achievable B-field at the implant, B_{max}.
    c. If the current is the limiting constraint, use (105) to determine Z_{crit}. If the implant is located a distance greater then Z_{crit}, use (102), otherwise use (103) to calculate the coil radius. Again, use (95) to determine B_{max}.

If there is no feasible solution (i.e. any design that meets geometric and/or current constraints does not produce a B-field at the implant that can provide the necessary power), the designer must loosen either the geometric or current constraints. An alternative possible solution would be to re-design the system for a much lower operating frequency at which there is a higher B-field safety limit.

The central objective of the chapter is to design a transmit coil to maximize the B-field at the implant location given safety, size, and current constraints. The idea behind

this approach is that by determining the maximum achievable B-field, B_{max}, at the implant, the designer can then design a receiving transducer, especially the ME receiver presented in Section 3.1, to achieve the required power from B_{max}. An alternative method would be to first design the receiver, and then determine the required B_{max} that will provide adequate power. Under this scenario, (99) can be used to optimize the coil geometry and (97) can be utilized to determine the required current to achieve the desired B_{max}.

Additionally, the design process introduced in this work assumes that the air gap, *b*, between the transmit coil and the skin can be minimized to be close to zero. This is because the maximum magnetic field for a WPTS for an implant always occurs when the air gap is zero or nearly zero. However, if there is a constraint on the system that does not allow the air gap, *b*, to be near zero, the equations derived in the previous sections can be adapted to maximize the B-field at the implant considering the non-zero air gap. The extended equations are explained in the Section 3.5. The general design process above applies equally to both scenarios when the air gap is zero or non-zero.

In the interest of clarity, some important aspects of the transmitter have not been discussed here. The transmit coil will naturally be designed with copper wire with finite resistance that produces heat when current is applied. The generally recommended current density to avoid overheating of copper wire is between 5 – 6 $\frac{A}{mm^2}$. Once the optimal radius and current of the transmitter is determined, the thickness of the coil should be adjusted such that the current density does not exceed this limit. Moreover, the required current could be lowered by using smaller wire gages and an increasing number of terms. Previous work has been done on the optimal techniques to construct solenoids

consisting of multi-turn wires [94]–[96]. Finally, the efficiency of the transmitter system has not been considered in this study. The goal here was to optimize the transmit coil geometry. However, in most circumstances it is also important to design the transmitter electronics to either maximize the system efficiency or minimize the transmitter power consumption for a given produced B-field. This includes designing high Q transmit coils, which could improve the efficiency of the system. Nonetheless, the key conclusions, and attendant optimal design process, still hold and can provide a useful design guide.

3.5 Power and Additional Constraints

3.5.1 Non-Zero Air Gap with Geometric Constraints

Having the air gap, *b*, equal to or nearly equal to zero is the optimal case for maximizing the B-field inside the human body. However, if this distance cannot be made close to zero, the design process proposed in this chapter can still be utilized with some modifications. For a WPTS that is geometrically constrained, the optimal transmit coil radius is still equal to the constraint limit even if *b* is non-zero. However, the optimal current in (97) now becomes

$$I = \frac{2B_{safe}\left(b^2+R^2\right)^{\frac{3}{2}}}{R^2\mu}. \qquad (97a)$$

Increasing the air gap, *b*, increases the optimal current, and an increase in *b* has a larger impact on the optimal current than an increase in the transmit coil radius, *R*.

Additionally, a non-zero air gap causes (99) to change to

$$\Gamma = \frac{\left(b^2+R^2\right)^{\frac{3}{2}}}{\left(\left(z_{implant}+b\right)^2+R^2\right)^{\frac{3}{2}}}. \qquad (99a)$$

Performing the same substitution as in the *Geometrically Constrained Transmitter Optimization* Section, and defining a ratio, a, the coil radius can be expressed as $R = aZ_{implant}$, $then$ (101) then takes the form

$$\Gamma = \frac{\left(b^2+a^2\, z_{implant}{}^2\right)^{\frac{3}{2}}}{\left(\left(z_{implant}+b\right)^2+a^2\, z_{implant}{}^2\right)^{\frac{3}{2}}}. \qquad (101a)$$

In order to get the same non-dimensional insight as (101), another ratio is added for the convenience. If the relationship between the implant depth and the air gap is expressed as $b = c\, z_{implant}$ where c is a non-dimensional ratio, (101a) reduces to

$$\Gamma = \left(\frac{c^2+a^2}{(c+1)^2+a^2}\right)^{\frac{3}{2}}. \qquad (101b)$$

The effect of the air gap is illustrated in Figure 3.11. Generally, as the air gap (represented by c in Figure 3.11) increases, the maximum achievable B-field decreases for a given size ratio, *a.* It is important to note that at a radius equal to zero, Γ can be numerically defined but that definition is trivial since there is no transmit coil.

However, there appear to be cases where $a < 1$ for which a non-zero air gap ($c >$ 0) seems to be beneficial and gives a higher Γ than the case with no air gap ($c = 0$). For example, see $c = 2$ in Figure 3.11. This phenomenon is closely related to the unconstrained WPTS optimization presented in the *Unconstrained Wireless Power Transmitter Optimization* Section. In that case, the optimal solution is a large coil with high current that produces a uniform magnetic field just under the safety limit. The same effect can, in part, be duplicated by a tiny coil with extremely high current that results in a near-uniform magnetic field at some short distance ($a < 1$) away from the coil. These solutions, while valid, may be impractical since they often necessitate kilo-amperes of

current in a small (mm or smaller) coil. The same or greater Γ can be achieved by an alternative coil that has a radius greater than the implant depth, i.e., $a \geq 1$, while utilizing a much lower current.

3.5.2 Non-Zero Air Gap with Current Constraints

Just as in the original case with no air gap, the optimal current is always at the constraint and there are two different solutions for the optimal radius of the transmit coil. However, instead of the implant distance, $Z_{implant}$ only, the determining factor now is a combination of the air gap and $Z_{implant}$. Similarly to Z_{crit}, there is a critical air gap, b_{crit}, in conjunction with $Z_{implant}$, that determines the optimal radius for the transmitter. b_{crit} is attained by solving the following equation,

$$0 = u_0 I \frac{\left(Z_{implant}^2 + b_{crit}^2\right)}{\left(b_{crit}^2 + 2\left(Z_{implant} + b_{crit}\right)^2\right)^{\frac{3}{2}}} - B_{safe}. \qquad (105a)$$

Given the complexity of the equation, numerical methods are more appropriate.

If the WPTS has an air gap $b \geq b_{crit}$, then the optimal radius of the transmit coil is

$$\mathrm{R_{opt}} = \sqrt{2}(Z_{implant} + b), \qquad (102a)$$

which is similar to (102) (when $Z_{implant} > Z_{crit}$ and $b = 0$). Indeed, the derivation of (13a) is identical to those of (102) and (107), except that $z = Z_{implant} + b$ is substituted into (106) instead of $z = Z_{implant}$.

If $b < b_{crit}$, the optimal radius of the coil R_{opt} is determined by

$$\frac{2\left(b^2 + R_{opt}^2\right)^{\frac{3}{2}} B_{safe}}{I\, u_0} - R_{opt}^2 = 0. \tag{103a}$$

Similarly, using numerical methods are the most suitable. The explanation for (102a) and (103a) is identical to the justification for (102) and (103). The optimal coil radius without a magnetic field safety constraint is given by Eq. (102a). However, there exists a region, dependent on the air gap and also the implant depth, where using (102a) would cause the magnetic field safety constraint to be violated at the skin. Therefore, in order to avoid this behavior while still maximizing the B-field at the implant, the optimal radius is given in (103a).

These principles are illustrated in Figure 3.12, which shows the B-field produced by optimal transmit coils for an implant located 2 cm beneath the skin with differing air gaps. Each WPTS has a current constraint of 15 A and a magnetic field safety constraint of 200 μT. Using (105a), the critical air gap for the given implant location and constraints is $b_{crit} = 1.05$ cm. The first two WPTSs with air gaps equal to 0 and 1 cm are cases where $b < b_{crit}$, which implies that the solution of (14a) is the optimal radius for these WPTSs. It can be observed that the B-field at the skin, marked by a star on the graph, is at the safety limit of 200 μT for the two WPTSs under consideration. In scenarios when $b > b_{crit}$, the B-field at the skin is no longer at 200 μT. Moreover, the larger the air gap, the lower the B-field strength is at the implant.

(103a) differs from (103) in that the optimal radius for transmit coils located below the critical distance is not constant, but rather polynomic. Figure 3.13 shows the radius of the optimal transmit coil as a function of the air gap, *b*, with differing current constraints. The magnetic field safety constraint is set constant at 200 μT and $z_{implant}$ =

2 cm for all systems.

It is essential to note that the critical airgap, b_{crit}, is a function of current constraint, magnetic field safety limit, and $z_{implant}$. More importantly, there are combinations of constraints and implant depths for which b_{crit} is undefined. This implies that the optimal solution of (102a) will not violate the safety limit regardless of how small the air gap may be.

Furthermore, depending on the imposed constraints, there may be two solutions to (105a) and (103a). However, one of them is nonsensical. In particular, (105a) may have a negative solution for b_{crit} which is invalid since b_{crit} is non-negative by definition. For Eq. (103a), both solutions to the optimal radius are positive however the larger radius is the feasible and preferable optimal radius. The other solution is usually too small, on the order of mm or smaller.

3.5.3 Power Constraints Instead of Current Constraints for WPTS

Previously, we assumed that the WPTS had a constraint on the amount of current in the transmit coil. This assumption was made because the B-field of the transmit coil depends solely on the current in the transmit coil. However, most RF power amplifiers do not have the user select a current setting but rather a power setting. This section will address how the design process changes when power is constrained instead of current. The approach is similar to the method described in Section 3.2.3, but the current is now a function of both power, P, and resistance, R_{el}, described in

$$I = \sqrt{\frac{P}{R_{el}}} \tag{108}$$

The resistance can be defined as

$$R_{el} = \frac{N\rho(2\pi R)}{A} \tag{109}$$

where ρ is the resistivity of the solenoid material, N is the number of turns of the winding, and A is the cross-sectional area of the solenoid winding. Taking the derivative of (95) with respect to the radius, R, but with I defined in (108) yields

$$\frac{dB}{dR} = \frac{-3\sqrt{2}AP\mu}{N\rho\sqrt{\pi}} \frac{(R^2 - z^2)}{[(R^2 + z^2)^{\frac{5}{2}}\sqrt{\frac{AP}{R\rho N}}\ ]} = 0 \tag{110}$$

Solving (110) while substituting in $R_{opt} = R$ and $z = Z_{implant}$ to find the optimal coil radius for an implant located at z, yeilds

$$R_{opt} = Z_{implant}. \tag{111}$$

For reasons identical to the ones given in Section 3.2.1, this solution is valid in the region for implants where $Z_{implant} > Z_{crit}$. For implants located at a distance less than Z_{crit} the optimal solution is

$$R_{opt} = Z_{crit} \tag{112}$$

where Z_{crit} is now defined as

$$Z_{crit} = \left[\frac{AP\mu^2}{8B_{safe}^2\rho N\pi}\right]^{\frac{1}{3}}. \tag{113}$$

These equations, (111) - (113) are very similar to their counterparts in the current constraint sections, (102)-(103), (105), expect the slope of the linear relationship is different (1 vs. $\sqrt{2}$) and the definition of Z_{crit} differs. In (113) Z_{crit} is a function of

B_{safe} to the two-thirds power versus B_{safe} to the first power in (105).

Using an example to further illustrate these rules, we construct three optimally designed coils for implants located at 4, 6 and 8 cm inside the body. The WPTS system has a power limit of 0.85 W and must not exceed a 200 μT safety constraint. The solenoid coil will be composed of copper, where $\rho = 1.68\, x10^{-8}$ Ωm, $N = 1$, and with $A = 10^{-6}\text{m}^2$. For this system, Z_{crit} is 4.3 cm. The three optimal radii for the transmit coils are 4.3, 6, and 8 cm. The B-field generated by each of these optimally designed coils is shown in Figure 3.14, where the maximum B-field at each implant occurs with its optimally designed transmit coil.

We assumed the cross-sectional area of the different radii solenoid transmit coils is constant for this analysis. This assumption reflects what we see as the practical application of these design rules when the designer has different sets of standard gauges of conductive wire available and is using them to build an optimal transmit coil and therefore needs to know the correct size coil to construct. Using a larger cross-sectional area leads to higher current as the resistance will drop and is an option for a designer to increase the B-field at the receiver if they are limited by power. Additionally, as mentioned above, care must be taken to ensure that the current going through the transmitter is less than 6 $\frac{A}{mm^2}$ to avoid overheating for copper wire.

Additionally, the resistance we examined in the above analysis is the solenoid coil's DC resistance. When operating at high frequencies, AC resistance also becomes a factor. However, the AC resistance of a coil is equal at a given frequency for a given solenoid cross-sectional area, as long as the coil's wire radius is greater than the skin depth. The ratio between the coil length and its cross-sectional area as defined in (109)

does not change for AC resistance, meaning that the conclusions we draw will still be valid, but the overall current for a given power will be lower as the frequency is increased. Practically, the frequency is usually chosen by the designer based on the receiver design and the safety limits and not based on minimizing AC resistance.

3.6 Conclusion

The optimal design for a transmit coil to power biomedical implants while staying below a magnetic field safety limit depends heavily on the system constraints (such as, B-field safety constraint, transmit coil geometry, and current consumption) and the depth of the biomedical device. If there are no additional constraints besides the magnetic field safety limit, a near uniform magnetic field can be created through large coils with high currents. However, if size constraints are applied, the optimal coil radius will be at the constraint (i.e., the maximum allowable radius). The current that maximizes the B-field at the implant while not violating the B-field safety constraint at the surface of the skin can be calculated accordingly. In this case, the strength of the maximum achievable magnetic field depends solely on the size constraint. The equations are applicable for the reverse problem as well. Given a minimum needed magnetic field, the necessary coil size and current can be found. Additionally, there is no benefit to operating with any air gap between the transmitter and the human body due to the nature of the magnetic fields produced by a current loop.

The design rules for an optimal wireless power transmitter given a current constraint differ from the geometrically constrained case. The maximum magnetic field occurs when the current constraint is active. The optimal radius of the transmitter is

dependent upon the depth of the medical implant, the magnetic field safety limit, and the current or power constraint. A critical distance, Z_{crit}, was found such that for any implant depths less than Z_{crit}, the safety limit constraint is active and the optimal radius is not a function of the implant depth, but only of the current constraint and safety limit. For an implant depth greater than Z_{crit}, the safety limit constraint is not active and the optimal radius becomes a linear function of the implant depth. These design guidelines were experimentally validated and shown to hold true for a constructed case study.

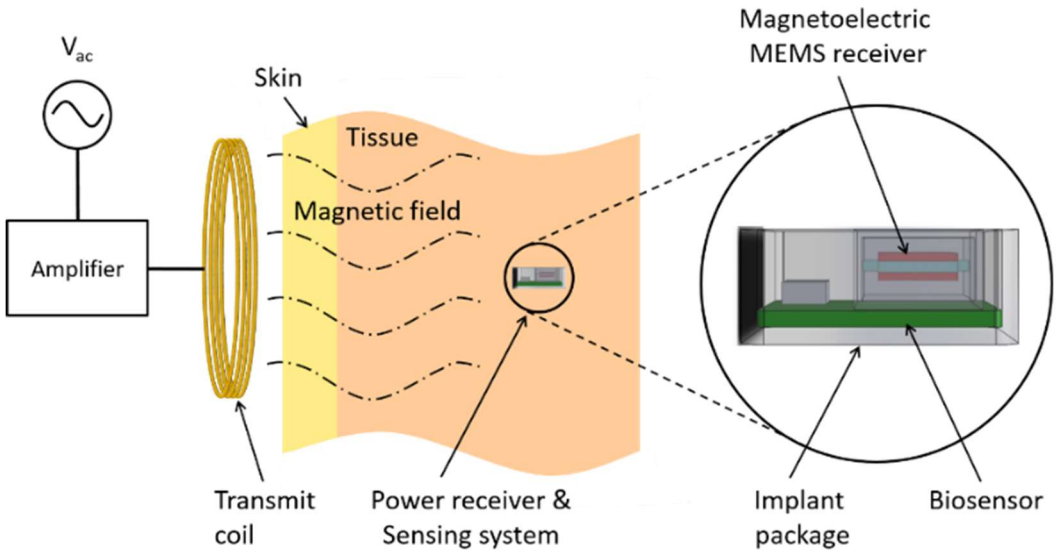

Figure 3.1 A full system diagram of a magnetoelectric transducer WPTS. The power generated by the receiver is positively correlated with the strength of the B-field. The system is weakly coupled, implying that the transmitter dynamics can be examined independent of the receiver.

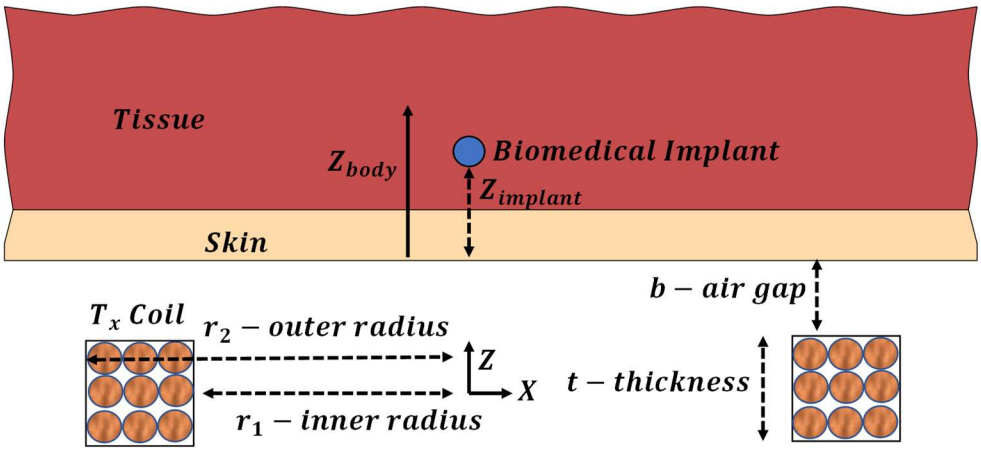

Figure 3.2 Coil optimization parameters labeled with a cross-sectional view of the solenoid. The z axis origin is in the middle of the solenoid coil, with an air gap between the coil and the body. The distance into the human body along the z axis is Z_{body} and the biomedical implant is located at a fixed distance of $Z_{implant}$, measured from the skin, into the human body [97].

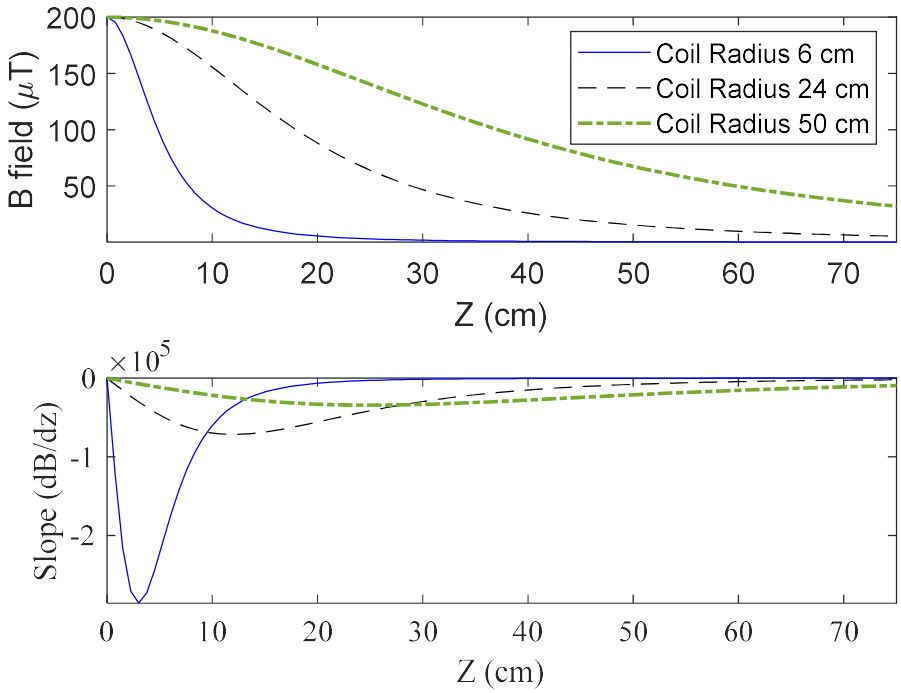

Figure 3.3 B-field amplitude and its derivative with respect to the distance z for three transmitters with different radii using their optimal current. The shape of the B-field as well as $\frac{dB}{dz}$ is similar in all three cases. The slope of the B-field is always negative, and always initially becomes more negative (i.e. the curvature is negative) before flattening out [97].

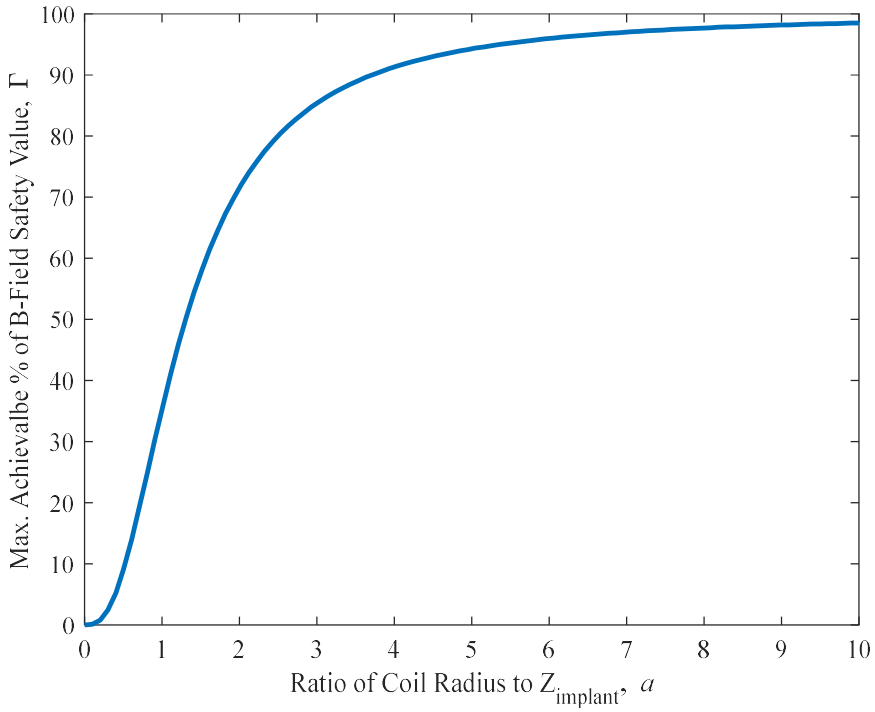

Figure 3.4 Size constraint effects on maximum achievable B-field. The larger the allowable size of the coil relative to the implant depth, the higher the attainable B-field at $Z_{implant}$ [97].

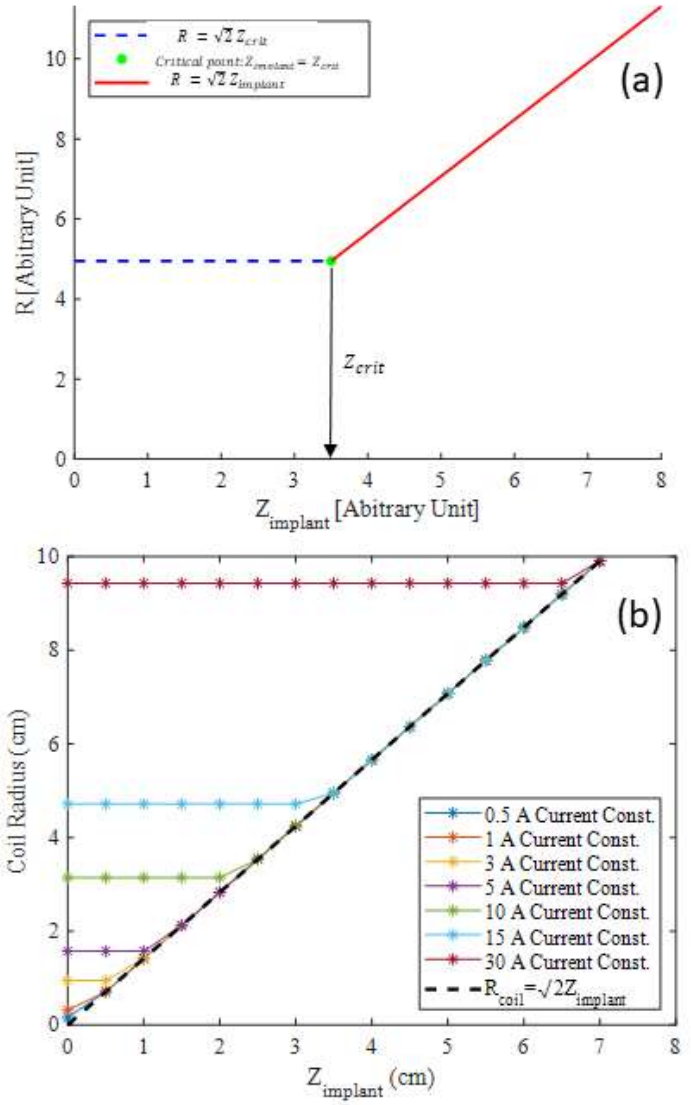

Figure 3.5 Examples of the critical distance for different current constraints. (a) Definition of the critical distance. (b) The radius of the optimal coil design in terms of implant depth for different current constraints. The magnetic field safety limit is held constant at 200 μT for all cases. For shallow implant depths ($Z_{implant} < Z_{crit}$), the transmit coil radius is constant for a given case. Once the implant depth is equal to $Z_{crit,}$, the radius increases linearly at the same rate for all cases, independent of the current and magnetic field safety constraints [97].

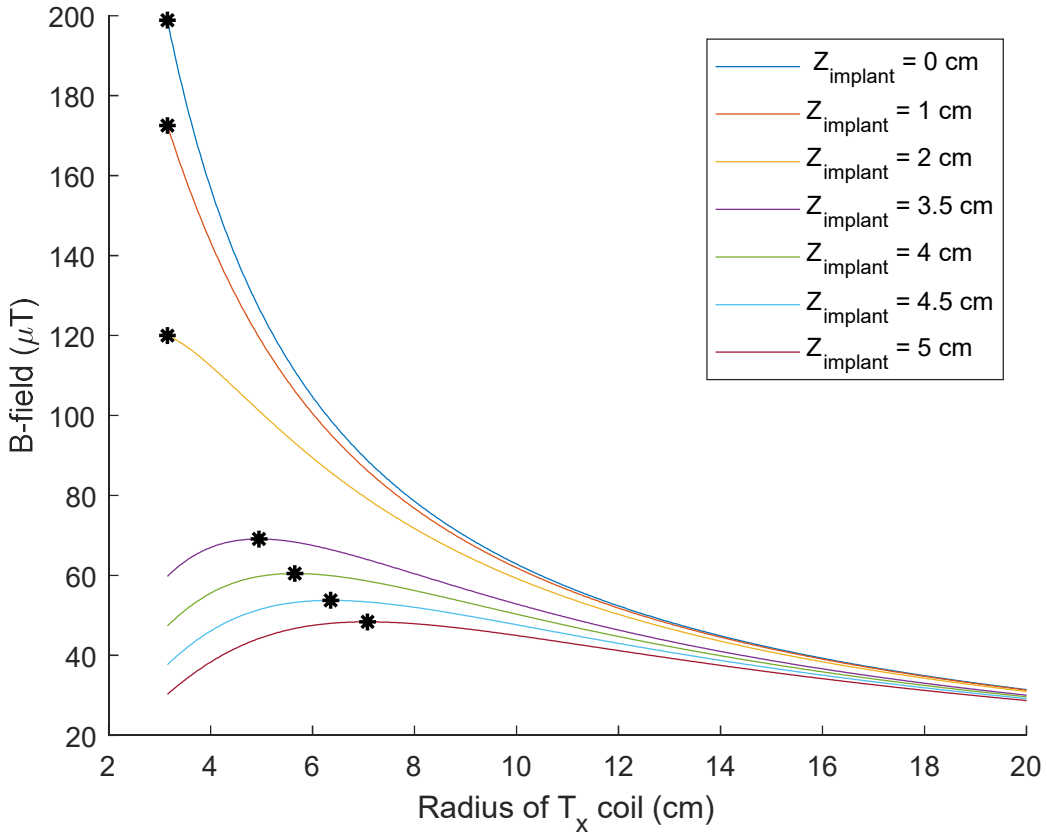

Figure 3.6 The B-field plotted at different distances inside the human body, $Z_{implant}$, vs the radius of the transmit coil. The max B-field is marked on each curve. The smallest allowable coil radius is 3.16 cm, any smaller and the safety limit of 200 μT at the skin would be violated. For all distances less than Z_{crit}, 2.2 cm in this case, the max B-field occurs with a coil radius equal to 3.16 cm. For distances greater than Z_{crit}, the max B-field occurs at a unique transmit coil radius dependent upon the location of the implant.

Table 3.1 Experimental optimal coil parameters

Coil Radius	Number of Turns	Wire Diameter	Current (RMS)
5.65 cm	9	1.291 mm (16 AWG)	15 A
7.78 cm	9	1.291 mm (16 AWG)	15 A

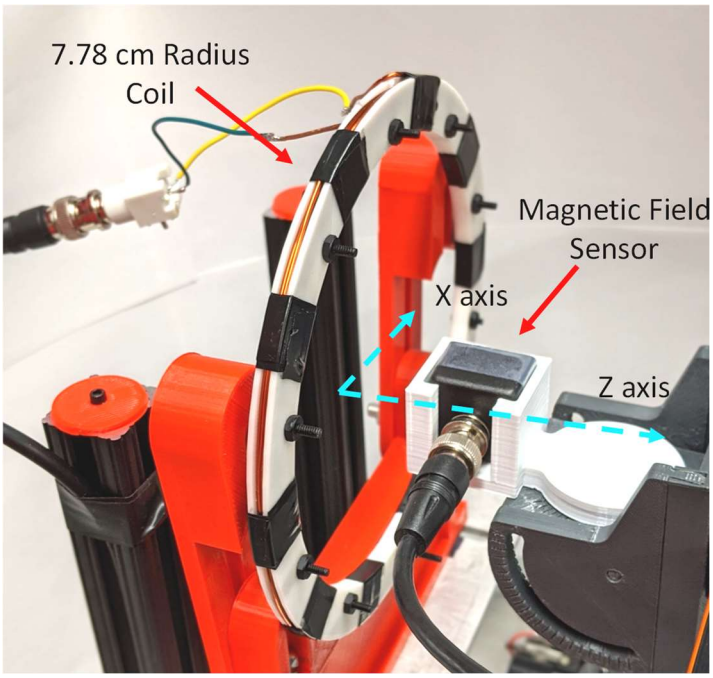

Figure 3.7 The 7.78 cm radius solenoid coil attached to the experimental setup. The setup consists of aluminum supports and screws as well as ABS plastic. These materials were selected because of their neutral magnetic properties. Two different transmit coils were constructed with different radii and each coils' B-field was experimentally validated.

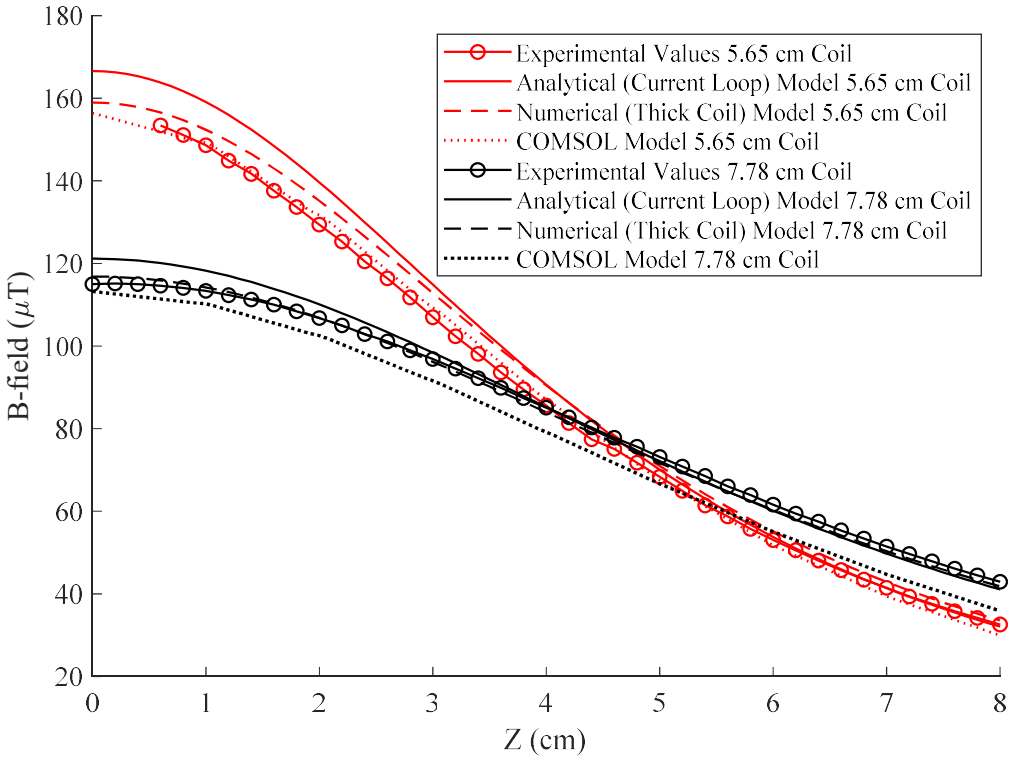

Figure 3.8 Experimentally measured B-field field using the MC110A magnetic field sensor, simulated B-field data using COMSOL, the analytical solution to the B-field of a current loop along its centerline, and a thick solenoid coil B-field numerical approximation versus distance into the human body for the 7.78 cm coil. The measured experimental data closely follows the simulated data.

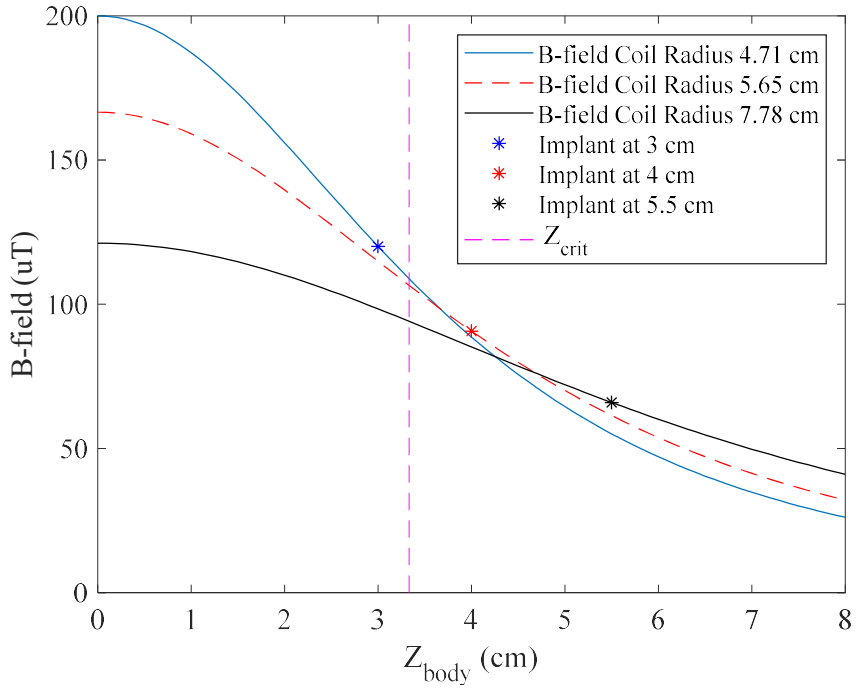

Figure 3.9 Simulated B-field using the analytical model in Eq. (4) as a function of the distance into the body for three coils optimized around different implant depths. The optimally designed coil gives a greater B-field at its own implant distance in comparison with the other two coils. At any distances, all three coils produce a B-field that is under the safety limit of 200 μT.

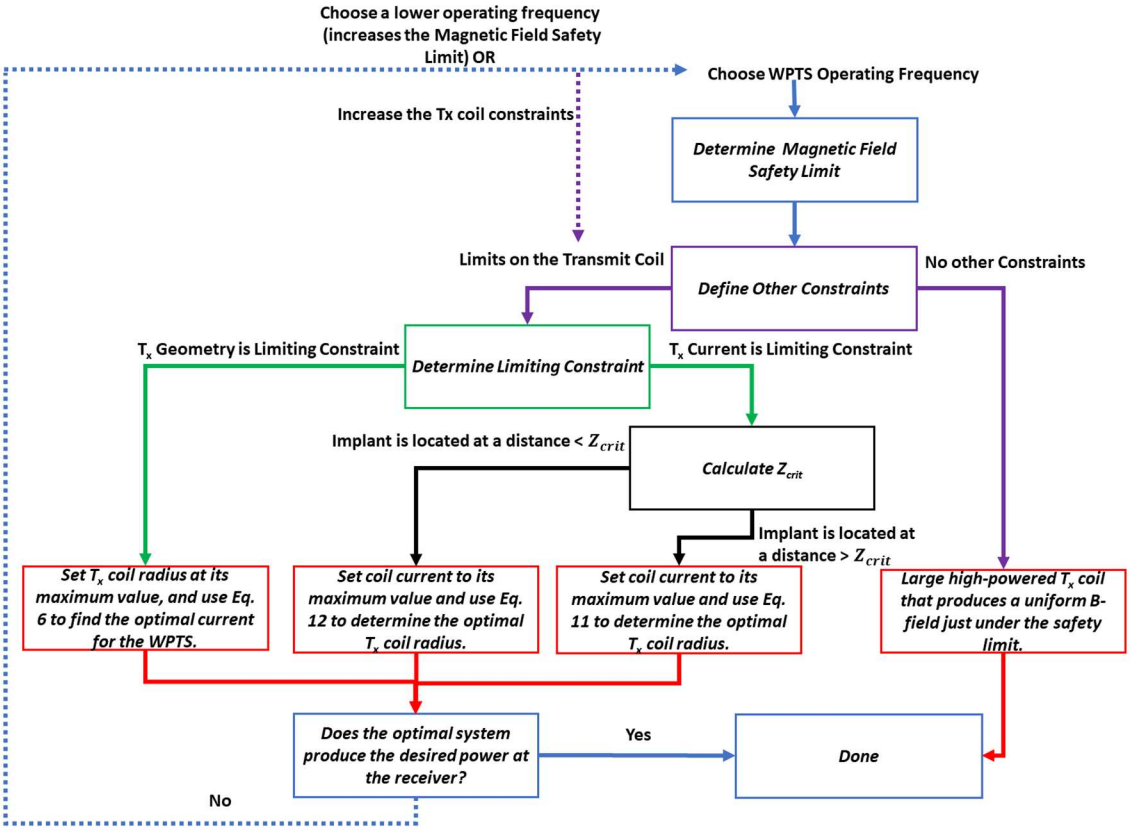

Figure 3.10 Flow chart illustrating the 3 step design process for optimal transmit coil design.

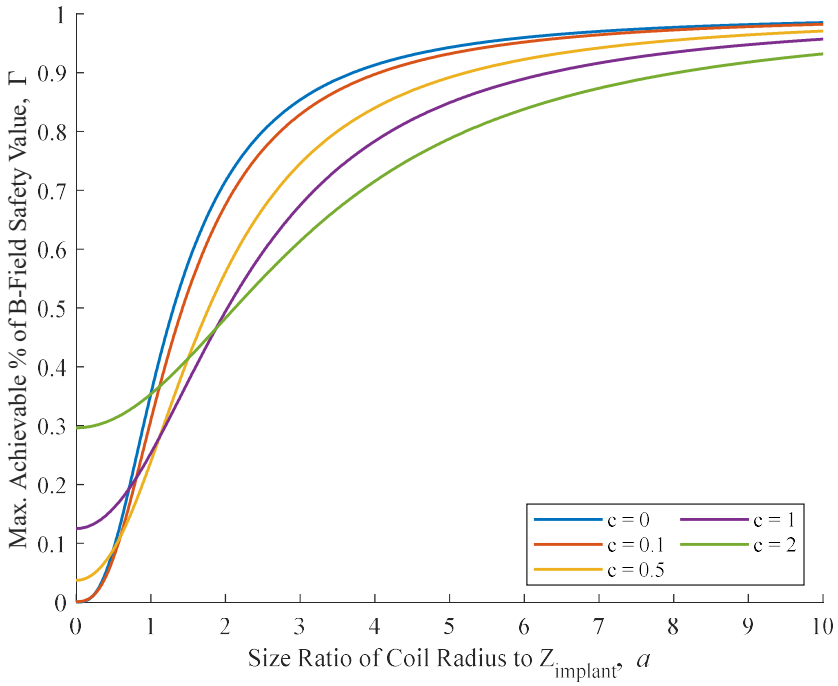

Figure 3.11 Maximum achievable B-field ratio (Γ) versus coil radius ratio (a) for different air gaps ($c = b\ Z_{implant}$). As the air gap increases (i.e. c increases), the maximum achievable B-field (or equivalently, Γ) decreases for the same a.

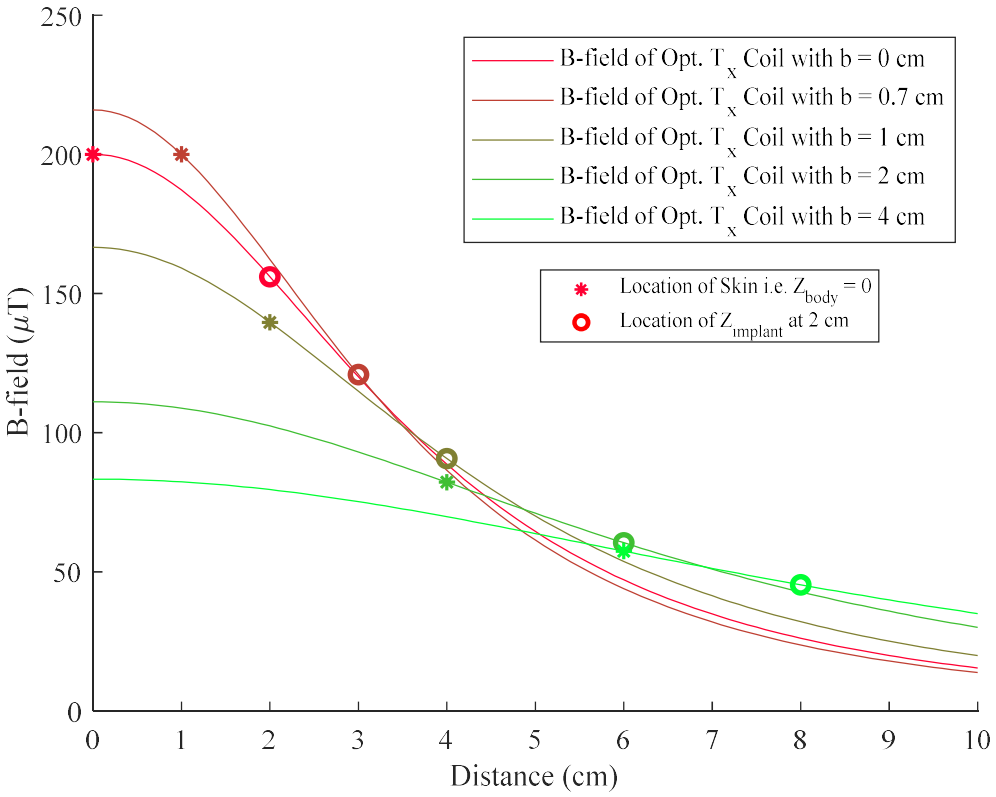

Figure 3.12 The B-field produced along the centerline of optimal transmit coils in WPTSs with different air gaps b. The implant is located at a depth of 2 cm for all cases and its location for each different WPTS is marked with a circle. The strength of the B-field at the skin for each case is denoted by a star . Current constraint is 15 A and B-field constraint is 200 μT.

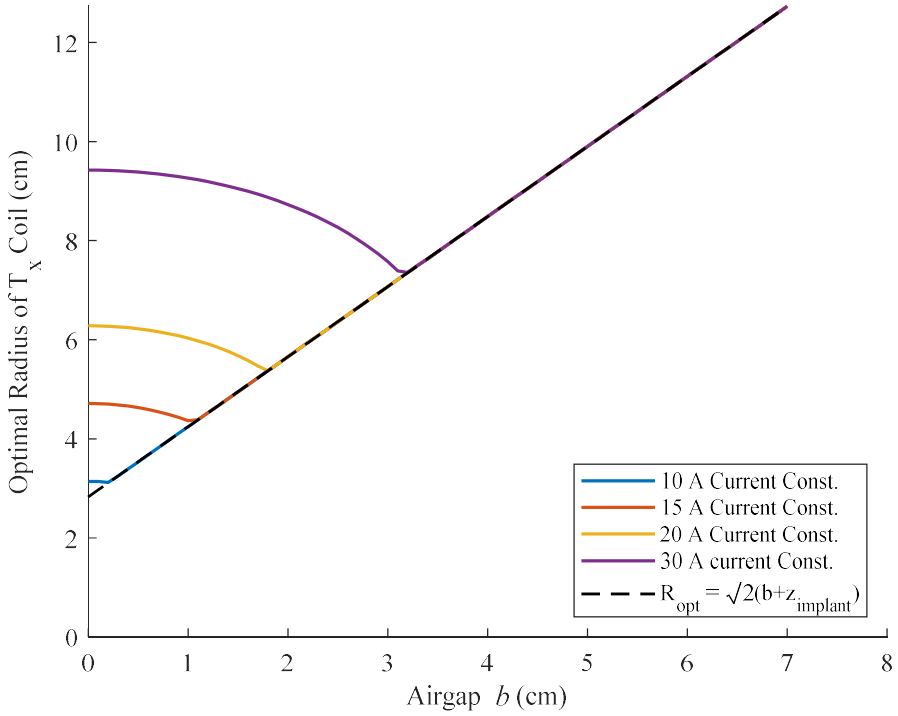

Figure 3.13 Optimal radius of transmit coil in terms of different air gaps for various current constrained WPTS. For air gaps below b_{crit}, the optimal radius is polynomic. If the air gaps are greater than b_{crit}, the optimal radius is obtained by Eq. (14a), regardless of the current constraint. All WPTSs have a magnetic field safety constraint of 200 μT and $z_{implant} = 2\ cm$.

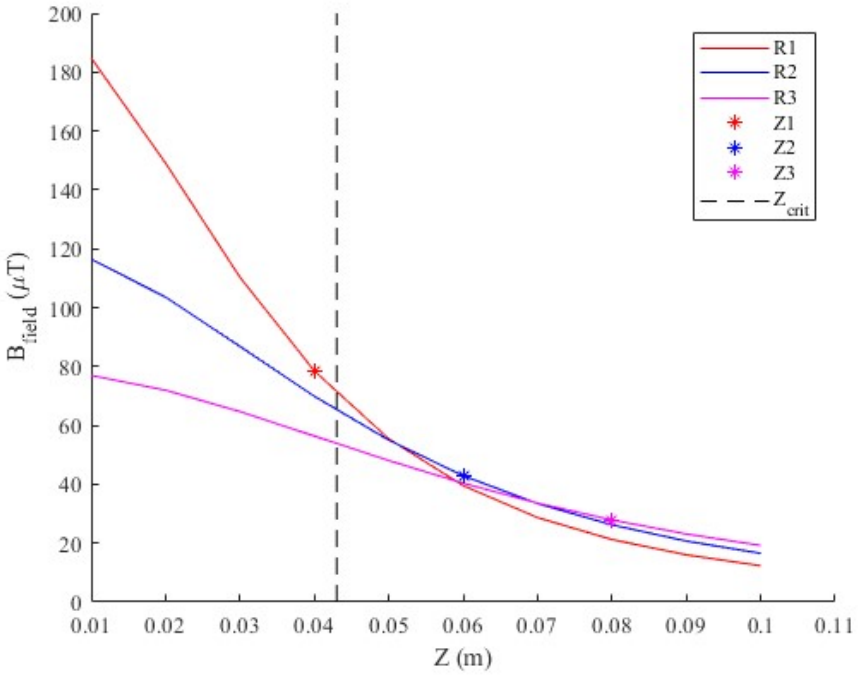

Figure 3.14 B-field vs Z for three different optimally designed WPTS. The implants are located at 4, 6 and 8 cm (indicated by the stars). The maximum B-field at each implant occurs with its optimally designed transmit coil. The safety limit of 200 μT is maintained.

CHAPTER 4

DESIGN AND CHARACTERIZATION OF A RIC WPTS FOR A KNEE STABILITY SENSOR

This chapter uses the principles of Chapter 3 to build a RIC WPTS for a specific biomedical sensor. This work was done in collaboration with the group of Professor Peter Woias at the University of Freiburg (IMTEK). I would like to acknowledge the contributions of Laura Cornella and Karthika Prakash in developing the knee stability sensor.

4.1 Introduction

The previous chapter explored how WPTS can be optimized for maximizing the B-field at the receiver when the WPTS has safety, size, and power constraints. This chapter will explore how those principles were used to design a wirelessly powered biomedical device, specifically a knee sensor to help diagnose anterior cruciate ligament (ACL) injuries. This work was done in collaboration with a group at IMTEK (University of Freiburg, Germany).

One of the most common knee injuries is the anterior cruciate ligament (ACL) tear, accounting for 20% of all knee injuries [98]. Physical examination methods are standardized for diagnosing ACL tears, however, the diagnoses vary when a patient is

seen by different examiners. This range of outcomes happens despite the standardized procedure because there are flexible parameters, such as the examiner's hand size or pressure applied, and the diagnosis relies on the examiner to detect subtle differences in the patient's knee's laxity. A better method to give more repeatable results would be using a biomedical sensor.

Our collaborators at IMTEK developed a flexible knee sensor that could measure the knee's laxity to help diagnose ACL tears. This system is composed of a polymer-based capacitive strain gauge sensor attached to an ASIC with a Bluetooth antenna capable of wirelessly transmitting its data. The strain gauge capacitive sensor consists of 279 fingers separated by a distance of 0.4 mm and two enlarged contact areas, as shown in Figure 4.1. The total length and width of the strain gauge sensor are 65 x 11.5 mm. Powering this sensor through wires could limit the natural dynamic range of the patient and limit the physician's movement around the patient. Powering the implant using a battery is an option, but it is not as environmentally friendly as single-use batteries can be ecologically wasteful. Additionally, the EU is increasing considering resolutions to reduce or entirely phase out the use of single use batteries[99]. The group at IMTEK ask us to develop a WPTS to power their knee sensor.

4.2 System Constraints for the WPTS

The WPTS has both size and power constraints. For the WPTS to be conducive to the physician's operating environment, a size constraint of 11.5 cm was imposed on the transmit coil's radius. Additionally, the receiver must fit comfortably on a patient's legs, so it was constrained to be no larger than a circle with a 4.25 cm radius. The WPTS also

had to be capable of working with a 20 W RF power amplifier. Furthermore, the WPTS had to be able to power the IMTEK sensor over a minimum distance of 10 cm. The IMTEK knee sensor system, on average, uses 6 mW of power, which would spike to 36 mW when the Bluetooth antenna was broadcasting.

At this time, the highest-powered ME transducer receiver we had developed in our lab was a 1 x 2 cm, two-layer Galfenol, one layer PZT device. At its optimal loading, it produced 4.97 mW of power with a B-field of 120 μT. Assuming a factor of safety of 3x and a small storage capacitor to help power the device when the Bluetooth is broadcasting and the power consumption spikes, we would need a B-field of 230 μT to generate 18 mW of power. Using the optimal design procedure outlined in Chapter 2, the limiting constraint was found to be the radius of the coil. With a transmit coil radius of 11.5 cm, 146.4 A is required to produce 230 μT at 10 cm. This high current and B-field requirement make ME transducers less feasible than a RIC WPTS for this device. The current ME receiver is much smaller than the constrained size, and it could potentially be enlarged to generate more power at a lower B-field. However, adding more ME material is a detriment in this scenario because the increased receiver mass could possibly affect the inertia of the patient's knees and add some error to the knee sensor’s readings. So due to the relatively high-power requirements, large gap between the transmitter and receiver, and the large allowable size of the receiver, we choose to design a RIC WPTS instead of a ME WPTS.

4.3 Fundamentals of RIC WPTS

RIC WPTS involves two tuned LC circuits. The inductors in the RIC WPTS are the transmit and receive coils, while external capacitors are added to tune the two coils to a single resonant frequency. The efficiency of a two coil RIC WPTS is expressed by

$$\eta = \frac{k^2 Q_1 Q_2}{(\sqrt{1 + k^2 Q_1 Q_2} + 1)^2} \tag{114}$$

where Q_1 and Q_2 are the quality factors of the transmitter and receive coils defined as

$$Q_1 = \frac{\omega_0 L}{R_1}. \tag{115}$$

The coupling coefficient, k is defined by $k = M/\sqrt{L_1 L_2}$, where M is the mutual inductance between the two coils.

Equation (114) shows that the overall efficiency of the WPTS depends on three factors, the operating frequency, ω_0, the coupling coefficient, k, which is a measure of the fraction of B-field generated by the transmitter that passes through orthogonality the place circumscribed by the receiver, and the quality factors of the coils.

We choose an operating frequency of 6.78 MHz. This frequency is the highest ISM Band open frequency for which we also have an operational power amplifier and is becoming a common operating frequency for RIC WPTS [100]. Additionally, buying electronic components that are sourced for this range is much cheaper than for systems operating at higher frequencies, which would be beneficial if this sensor system were made into a commercially viable product.

The coupling coefficient, k, can be maximized by making the transmit and receive coils the same size and minimizing the distance between them. However, we are constrained in our case from maximizing k by both the constraint on the receive coil size

and the minimum distance constraint between the transmit and receive coil.

Using the optimal design process outlined in Chapter 2, we discovered that size was our limiting constraint, and therefore the transmit coil was built to be at the size constraint. The receive coil was also built at its size constraint to further maximize the coupling coefficient. While building the coils at their size constraint helps maximize k, the distance constraint between the transmitter and the receiver is relatively large compared with the coils' size, which will lead to a small coupling coefficient.

Maximizing the quality factors of the coils involves maximizing L while minimizing the parasitic resistance. The inductance can be increased by adding more and larger turns to the transmit or receive coil. However, the total number of turns is limited by the coil's size constraint and the coil's self-resonant frequency. Additionally, adding more turns increases the parasitic resistance as well.

Every coil can be modeled as an inductor with parasitic resistance and capacitance. As the number of turns on a coil is increased, both the inductance and the parasitic capacitance increase. The self-resonant frequency of the coil is determined by

$$\omega_0 = \frac{1}{\sqrt{LC_p}} \tag{116}$$

where C_p is the parasitic capacitance of the coil. Tuning the coil to the operating frequency of 6.78 MHz is done by adding external capacitance, meaning that the tuned resonant frequency can only be lower than the self-resonant frequency of the coil. Therefore, the self-resonant frequency must be greater than the operating frequency, limiting the number of turns utilized in the transmit and receive coils.

4.4 Design of WPTS for Knee Stability Sensor

The WPTS transmit and receive coils we designed are outlined in Table 4.1. Additionally, we designed the power conditioning circuity, consisting of a half-wave rectifier, filter capacitors, and a linear dropout regulator (LDO) to deliver the correct voltage to the MCU, as shown in Figure 4.2. We choose SMC 30 V 100 mA Schottky diodes due to their fast recovery time. We used Johanson Technology High Q/Low ESR capacitors which are high voltage and high Q capacitors. And we used a Onsemi 3.3 V 100 mA LDO due to its low quiescent current and voltage drop. Two 100 nF SMD capacitors were used as the filter capacitors in the power conditioning circuit.

For the testing in our lab at the University of Utah, we used an E&I 240L 40W RF power amplifier to supply current to the transmit coil. Additionally, we used an MFJ 939 antenna tuner to help impedance match between the RF power amplifier and the transmit coil.

As shown in Figure 4.3, the WPTS can transmit 997 mW of power at 10 cm and 355 mW of power at 15 cm with the transmit coil supplied with 10 W of power. With the addition of the power conditioning circuity, the power drops to 341 mW at 10 cm and 146 mW at 15 cm. We tested it with the identical MCU used in the IMTEK sensor (except this MCU is integrated into a TI LaunchXL-CC26X2R1-ND evaluation board, and it consumes 306 mW of power) and were able to successfully power the MCU with up to 12.5 cm of displacement.

Since the receive coil might shift and become angularly misaligned as the knee rotates, we tested the misalignment tolerance of the WPTS. The WPTS, while transmitting at 10 W, is able to deliver 330 mW of power at 60 degrees of misalignment,

as shown in Figure 4.4, which would sufficiently meet the power demands of the sensor.

4.5 WPTS Integration

Unfortunately, when the RIC WPTS we originally developed was being integrated with the knee sensor at IMTEK, the RF power amplifier at IMTEK broke on the first day of testing. This was the only RF power amplifier we had access to at IMTEK that could deliver power at 6.78 MHz. Due to this unfortunate circumstance, we had to quickly redesign the WPTS to work with a different RF power amplifier that was rated for operation between 20 -500 MHz. The WPTS was rebuilt to operate at a higher frequency.

The new WPTS comprises a Mini-Circuits ZHL-100W-GAN+ Class-A power amplifier and a different transmit coil and receive coil tuned to a higher operating frequency. The transmit coil and receive coils are described in Table 4.2. The transmit coil is a series LC circuit, with the tuning capacitance added in series to avoid saturating the voltage limits of the power amplifier. The receiver is tuned as a parallel LC circuit to achieve the necessary voltage input for the sensor's MCU.

The power conditioning circuit was not changed and still was composed of a half-wave rectifier, a 100 nF smoothing capacitor, and an LDO that ensures the voltage will not exceed the 3.3 V input limit of the sensor’s MCU. Additionally, no impedance matching was done with this WPTS. The modified WPTS could power the TI LaunchXL-CC26X2R1-ND evaluation board, which consumes 306 mW of power, at 7 cm. The complete wirelessly powered sensor system was first successfully demonstrated on a robotic knee, as shown in Figure 4.5 and then used to power the sensors in human experimental trials.

4.6 Conclusion

Using the optimal design procedure outlined in Chapter 3, we successfully constructed a RIC WPTS to power a biomedical sensor. The WPTS consisted of a transmit coil that can easily fit on a physician's table and a receive coil that can be attached to the patient's leg. The WPTS was capable of delivering 341 mW of power of 10 cm and could withstand misalignments of 60 degrees. The RIC WPTS was integrated with a knee sensor developed by IMTEK and used in experimental trials with their biomedical sensor.

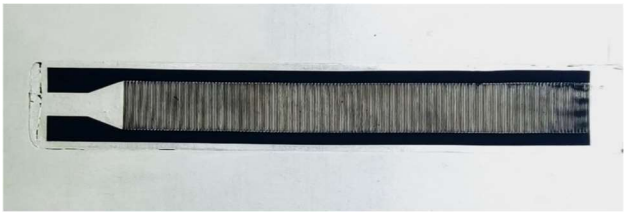

Figure 4.1 The capacitive sensor developed by IMTEK to measure the knee's laxity. When the sensor is stretched, the change in capacitance is measured, and the knee's rotation can be calculated.

Table 4.1 Original WPTS parameters

Coil	Dimensions	Wire Comp.	Tuning Capacitance	Resonant Frequency	LC Resonant Circuit Geometry	Q
Transmitter	6 turn, 6.25 cm and 11.5 cm (inner and outer radii)	Copper, 22 AWG (0.644 mm)	15 pF	6.98 MHz	Series	26.8
Receiver	8 turn, 2 and 4.25 cm (inner and outer radii)	Copper, 22 AWG (0.644 mm)	129 pF	6.75 MHz	Parallel	4.80

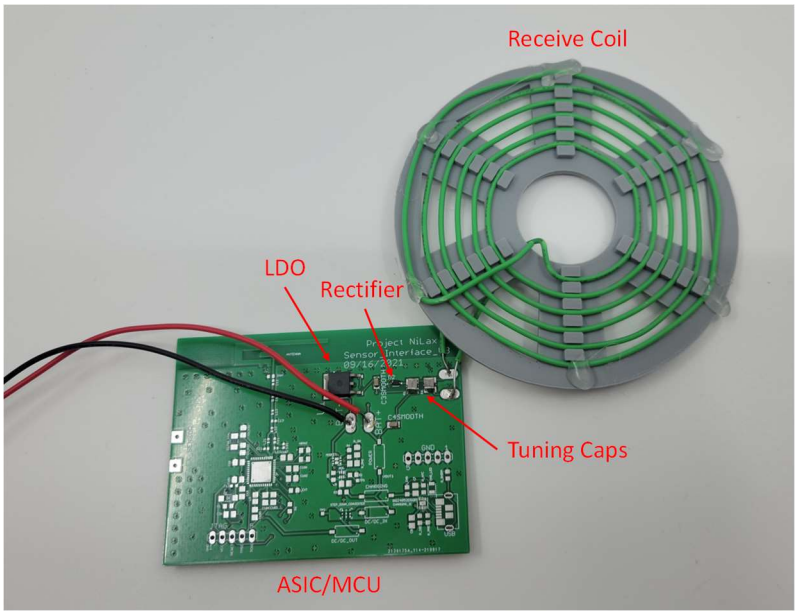

Figure 4.2 The 6-turn, 4.25 cm radius receive coil attached to the IMTEK Knee Sensor printed circuit board. Only the WPTS components have been populated. The receive coil is tuned to a resonant frequency of 6.78 MHz through external capacitors. The power is rectified through a half-wave rectifier. The 3.3 voltage input for the MCU is maintained through an LDO.

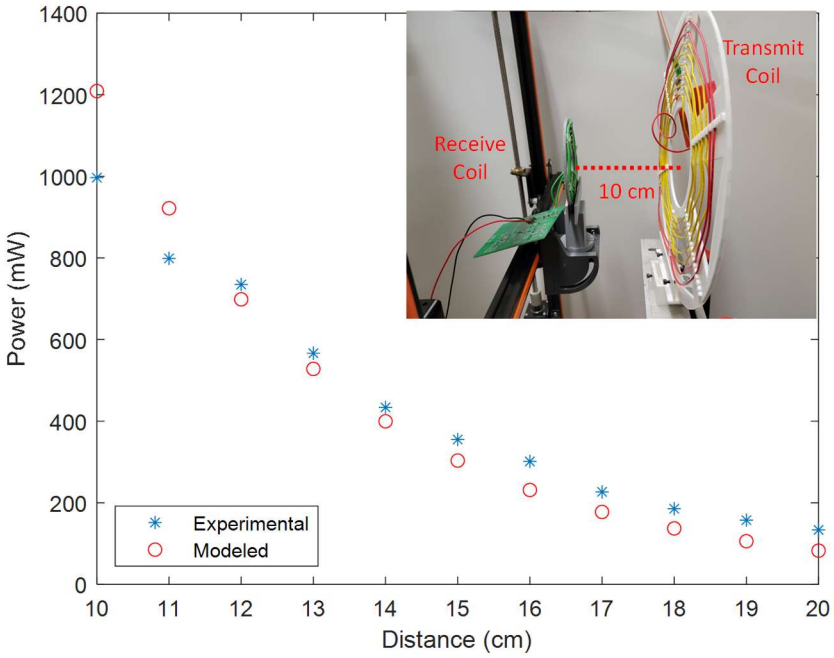

Figure 4.3 Received power (AC) versus distance for the RIC WPTS. The WPTS could supply 997 mWs at 9.97% efficiency over a distance of 10 cm, far exceeding the necessary power requirements for the IMTEK knee sensor. The experimental results closely follow the predicted model. **Inset**: The experimental setup for the RIC WPTS.

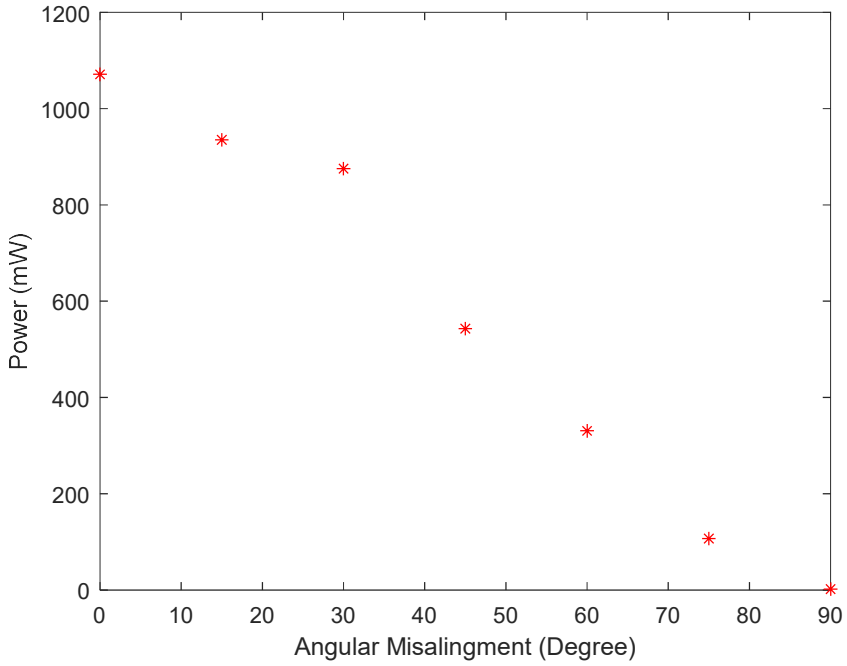

Figure 4.4 Received power (AC) versus angular misalignment for the RIC WPTS with the receive coil located 10 cm from the transmit coil. The RIC WPTS can supply 330 mW of power with the receiver misaligned by 60 degrees, enabling the IMTEK sensor functionally even if the receive coil rotated during the experimental trials.

Table 4.2 Modified WPTS parameters

Coil	Dimensions	Wire Comp.	Tuning Capacitance	Resonant Frequency	LC Resonant Circuit Geometry
Transmitter	2 turn, 6 cm and 9 cm (inner and outer radii)	Copper, 22 AWG (0.644 mm)	27 pF	19.34 MHz	Series
Receiver	1 turn, 3.75 cm radius	Copper, 22 AWG (0.644 mm)	12 pF	19.38 MHz	Parallel

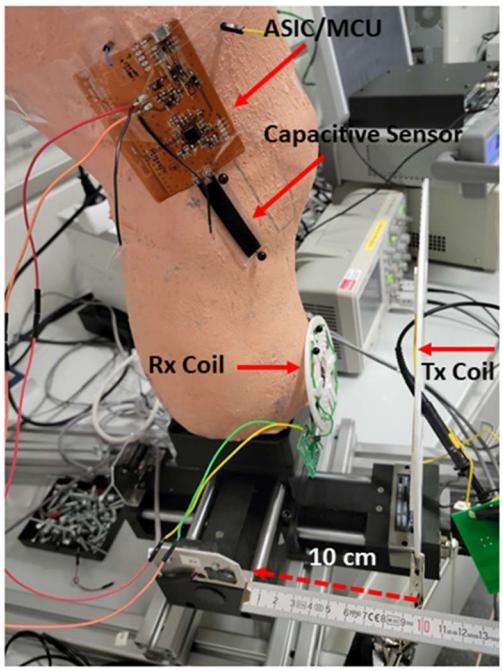

Figure 4.5 The WPTS was used to power the capacitive knee sensor on both the robotic knee and human patients. The WPTS could deliver adequate power to the sensor with a distance of 10 cm between the transmit and receive coils.

CHAPTER 5

A DYNAMIC TRANSMIT COIL THAT INCREASES EFFICIENCY FOR WIRELESSLY POWERING BIOMEDICAL IMPLANTS WITH MAGNETOELECTRIC TRANSDUCER RECEIVERS

In this chapter, we develop a novel method to counteract misalignment in WPTS using a dynamic transmit coil. The dynamic transmit coil uses servo motors to change the alignment of its B-field.

5.1 Introduction

In addition to adhering to magnetic field safety standards, another consideration for wirelessly powering biomedical implants is the effect of misalignment between the receiver and the transmitter in the WPTS. Once the surgeon installs an implant, its exact location and orientation may be unknown. Misalignment between the receiver and the transmitter reduces the efficiency of the WPTS, and this reduction in efficiency is true for both inductive [43]–[49] and ME WPTS [30], which require the B-field to be aligned with the receiver for maximum wireless power transfer.

As previously mentioned, the magnetic field exposure safety standards must be followed to safely power a biomedical implant. These safety constraints prevent compensating for the misalignment, and thus reduced efficiency, by just increasing the transmit coil power, and thus increasing the WPTS B-field, to obtain a certain power

level at the receiver. An inefficient WPTS could mean long recharge times for implants with a battery or passive implants (i.e., implants with no onboard energy storage) not receiving enough power to function.

Receiver misalignment can be compensated by adjusting the B-field to realign it at the receiver. Research has been done on omnidirectional WPTS that can alter the direction of the B-field at a point or specific points in space. The most common construction of omnidirectional WPTS is multiple transmit coils configured in either a single plane [53]–[55] or as orthogonal intersecting coils [50]–[52]. These omnidirectional WPTS can be used to realign the B-field with a misaligned receiver at a point in space, by using constructive interference of the B-field produced by the coil arrays. However, we want to explore a method to compensate for misaligned receivers by using a single solenoid coil.

A single coil transmitter using servo motors to alter its orientation/location, as shown in Figure 5.1, which we call a dynamic transmit coil, can increase power transfer to misaligned receivers without needing additional transmit coil arrays. The B-field's direction at the receiver can be altered and aligned with the misaligned receiver by actuating the transmit coil. Thus, increasing the power available to load at the receiver and the overall efficiency of the WPTS. Using a single transmit coil has an additional advantage. It is easy to calculate the B-field at the receiver and any location inside the body, ensuring that the receiver can get adequate B-field to power the device while ensuring all the magnetic field safety constraints are followed.

This chapter presents a novel method to increase efficiency and counteract misalignment in WPTS through the use of a dynamic transmit coil. This chapter will

explore the power gains (or increase of WPTS efficiency) of a dynamic transmit coil over a static transmit coil. Additionally, we present the closed loop control system that allows the dynamic coil to find its optimal position. We experimentally confirm our model's power gain by comparing the received power in two identical ME WPTS except for the use of a dynamic transmit coil over a static transmit coil. While a dynamic transmit coil can improve the efficiency of both inductive and ME WPTS, this chapter will focus solely on analyzing the efficiency and power gains for ME WPTS. We only examine ME WPTS because we assume the transmitter dynamics can be decoupled from the receiver, which is generally true for ME WPTS. This same analysis can also be applied to RIC WPTS in the weak coupling region (i.e., $k^2 Q_1 Q_2 \ll 1$) where the assumption of a decoupled transmitter and receiver is valid.

5.2 Methodology

5.2.1 ME WPTS Modeling

The equivalent circuit diagram of a ME WPTS is shown in Figure 5.2 [77]. The transmit coil is an electrical system in which the coil is represented as an inductor, L_r, with some parasitic capacitance, C_r, and parasitic resistance, R_r. The ME transducer receiver is composed of a magnetostrictive layer represented as an impedance, Z, with mechanical damping, b, and a piezoelectric layer which some self-capacitance, C_0. The magnetostrictive layer is coupled with the transmit coil through

$$\Psi_m = \alpha \Gamma_m \tag{117}$$

where Γ_m is the magneto-elastic transduction factor of the magnetostrictive layer, and α is a geometric factor that relates the dimensions of the transmit coil to the B-field, B_o, at

the ME transducer or

$$\alpha I = B_0 \tag{118}$$

The B-field at a point in space produced by a solenoid coil is

$$B = \frac{\mu}{4\pi}\iiint_V \vec{j}\, d\tilde{v} \wedge \frac{\vec{r} - \overrightarrow{r'}}{\left|\vec{r} - \overrightarrow{r'}\right|^3} \tag{119}$$

where μ is the magnetic permeability of the operating space, $\vec{j}$ is the current density, and $\vec{r} - \overrightarrow{r'}$ is a space vector between the point in space where the magnetic field is calculated and a location inside the solenoid conductor. V is the volume of the solenoid conductor. Using (119), we can easily predict the strength and location of the maximum B-field produced by the coil for a given power input and ensure it does not violate any safety constraints.

The piezoelectric layer is coupled with the magnetostrictive layer by Γ_p, the electromechanical transduction factor of the piezoelectric, defined as

$$\Gamma_p = -w\left(\frac{d_{31,p}}{s_{11}^E}\right) \tag{120}$$

where w is the width of the piezoelectric in the ME WPTS, $d_{31,p}$ is the transverse piezoelectric constant, s_{11}^E is the elastic compliance of the piezoelectric material.

Using the equivalent circuit diagram, it is possible to derive the optimal load, R_{opt}, for a ME WPTS operating at the ME transducer's resonance as

$$R_{opt} = \frac{\sqrt{M_1^2 + 1}}{\omega C_0} \tag{121}$$

$$M_1 = \frac{\Delta K}{b\omega}. \tag{122}$$

where M_1 is a resonator figure of merit defined as

ΔK is defined as

$$\Delta \mathrm{K} = \frac{\Gamma_p^2}{C_0} \tag{123}$$

where

$$C_0 = \frac{\epsilon_{33}^S wL}{t_p}. \tag{124}$$

ϵ_{33}^S is the permittivity through the thickness of the material at constant strain, assuming the device is a thin narrow beam, t_p is the thickness of the piezoelectric layer, ω is the operating frequency of the ME WPTS, and L is the length of the ME transducer. The ME WPTS is assumed to operate at the resonant frequency of the ME transducer.

The power delivered to an optimally loaded ME WPTS is

$$P_{opt} = \frac{\left(\Gamma_m B_{eff}\right)^2}{(4b)\mu^2} M_1(\sqrt{M_1^2 + 1} - M_1) \tag{125}$$

where b the mechanical damping coefficient is

$$b = \frac{\omega m}{Q} \tag{126}$$

where m is the equivalent mass of the ME transducer and Q is the quality factor of the ME transducer [77].

P_{opt} is proportional to the square of the effective B-field, B_{eff} defined as

$$B_{eff} = B_0 \cos\theta \tag{127}$$

where B_0 is the strength of the total magnetic field at the receiver, and θ is the angle between the receiver and the B-field. From (125) and (127), we see that as the B-field becomes more misaligned with the receiver, the power decreases as a function of $\cos^2\theta$. For a given ME transducer WPTS receiver, maximizing the power available to the load is equivalent to maximizing the magnetic field, B_0, at the ME transducer's location and

decreasing the misalignment between the receiver and the B-field produced by the transmitter, θ. Γ_m ,M_1, and b are all defined based on the ME receiver's material, geometry, and construction.

Electromagnets are the most common way to induce an AC magnetic field at the ME receiver's resonant frequency. Most electromagnets used for ME WPTS are solenoid coils due to their ease of construction and their well described magnetic wave propagation properties. Additionally, the optimization results in Chapter 3 for solenoid coils resulted in coil geometries where the thickness and length of the coil was much smaller than the inner radius of the coil. This chapter will consider transmitters whose geometry is a solenoid. For most WPTS using a solenoid coil, it is a flat solenoid coil, i.e. a coil whose radius is much greater than its thickness or length. For our WPTS, we also use flat solenoid coils, with the radius of the coil being the most important design parameter.

Additionally, when comparing a ME WPTS using a dynamic transmit coil and a ME WPTS using a static transmit coil we assume that the both ME WPTS are using identical ME transducers, operating at the same resonant frequency and loaded with the optimal load defined in (121). We define a figure of merit, T, as

$$\mathrm{T} = \frac{P_{dyanmic}}{P_{static}} \tag{128}$$

where $P_{dynamic}$ is the power delivered to the receiver using the dynamic transmit coil and P_{static} is the power delivered to the receiver using the static transmit coil defined in (125). However, since the ME transducer for both systems is equivalent, $\Gamma_m,\ b,\ M_1,$ and μ are equal and T can be reduced to

$$\mathrm{T} = \frac{B_{dynamic}^2}{B_{static}^2} \tag{129}$$

where $B_{dynamic}$ is the strength of the effective B-field (the strength of the B-field aligned with the ME transducer defined in (127)) for the dynamic transmit coil and B_{static} is the strength of the effective B-field for the static transmit coil.

5.2.2 Proposed Operating Environment

The operating environment we envision is one in which the dynamic transmit coil is at a fixed location (e.g. on a patient's desk or by a physician's table) and the ME receiver is implanted in a patient and located some distance away from the transmitter. The transmitter is not touching or in contact with the skin. Therefore, if the receiver is misaligned, the transmitter can rotate or translate to decrease the misalignment. As a patient is unlikely to know their implant's exact orientation and location, we believe that misalignment is highly likely to occur. Furthermore, if the patient moves while the transmitter is charging the receiver, the WPTS can adjust to ensure the WPTS is operating at maximum possible efficiency.

In this work, we considered two different types of dynamic transmit coils, as shown in Figure 5.1. The first type we call a translational dynamic transmit coil. It consists of a coil mounted to rails, similar to a fused deposition modeling 3D printer, that changes the position of the coil within the xy plane, as seen in Figure 5.3. This type of dynamic transmit coil can have an extensive range of adjustments, but it also requires a large footprint. The other type of dynamic transmit coil, which we call a rotational dynamic transmit coil, uses servo motors to change the orientation of the coil by rotating the coil about its motor's axis of rotation. The advantage of this system is that it has a

small footprint, barely larger than the solenoid coil itself; however, it lacks the full range of adjustment as the translational system. Additionally, the rotational dynamic transmit coil must operate in a region similar to what is shown in Figure 5.3, where the inner cross-sectional plane of the transmit coil is not parallel to the longitudinal plane of the ME receiver. If the dynamic transmit coil shown in Figure 5.3 were rotated 90 degrees by the distal joint, then it would be in a singularity and would lose one degree of freedom.

The WPTS is considered to operate at maximum possible efficiency when the dynamic transmit coil is in a position that supplies the maximum power, which is equivalent to the maximizing the effective B-field, to a receiver at a given location. For most locations, the optimal position of the ME receiver is located along the transmit coil's centerline z-axis, as seen in Figure 5.3. When the receiver becomes radially misaligned by some distance, R_{offset}, or angular misaligned by some angle, θ, measured with respect to the coil's z-axis and the receiver's longitudinal direction, the efficiency of the WPTS decreases. A dynamic transmit coil can either rotate or translate to increase the efficiency of the WPTS. The rotation and translation increases the B-field's alignment, which increases the strength of the B-field at the receiver.

For generality, all distances in this analysis were non-dimensionalized by the transmit coil's radius. This non-dimensionalization ensures that the coil comparisons are valid for any sized transmit coils operating with any given current. Additionally, we assumed a minimum distance of three quarters (0.75) of the transmit coil's radius between the transmit coil and the ME transducer receiver. This reflects what we envision as a likely operating scenario where the dynamic transmit coil is set on a surface with some non-trivial distance between it and the patient. Furthermore, it allows the rotational

dynamic transmit coil a rotational operating range of at least 50 degrees.

When doing this analysis, we used a solenoid transmit coil for both the static and dynamic WPTS with a radius of 7.78 cm, made of 9 turns with 16 AWG (1.291 mm diameter) copper wire supplied with 1.67 amps of current. We used this WPTS because it matches the system used in the experimental verification section of this chapter. However, because we normalized all distances by the transmit coil's radius and we are comparing the ratio of the power produced by an identical flat solenoid coil with the same given current for both the dynamic and static WPTS, these results are generalizable for any flat solenoid or ring sized transmit coil with any current. The ME transducer's location was varied along both the radial and transverse directions (along the xz-plane in Figure 5.3). The ME transducer is assumed to be placed at a value on the y-axis that aligns with the center of the transmit coil. At each point, the B-field for the static transmit coil, and the B-field for the dynamic transmit coil in its optimal alignment were computed and used to calculate T for a given location. The optimal alignment was calculated by sweeping the dynamic transmit coil through its full range of motion, calculating $B_{dynamic}$ at each point, and then saving the largest $B_{dynamic}$ value.

5.2.3 Modeling Results

Figure 5.4 shows the power gain from a dynamic transmit coil as a function of radial misalignment, rotational misalignment, and implant depth. The dynamic coil equals or outperforms the static transmit coil in every scenario, i.e., $T \geq 1$. Actuating the transmit coil leads to better alignment of the B-field and increases the strength of the B-field at the receiver, leading to an increase in available power for the system. While this

result may seem obvious, the value of this work lies in modeling the specific and significant power gains associated with adding a simple servo motor system to the transmit coil in a WPTS.

For the rotational dynamic transmit coil, the greater the angular misalignment of the receiver, θ, the higher the power gain, T, the dynamic transmit coil exhibited over the static transmit coil. With receiver misalignment (i.e., radial offset) under half of a coil radius, the dynamic transmit coil had regions where $T > 2$. Between roughly half a coil radius to one coil radius, the optimal alignment of the dynamic transmit coil is equivalent to the placement of the static transmit coil. In this region, $T = 1$, or both WPTS perform equally well. Unlike the B-field near the center of the coil, which is primarily aligned with the z-axis, the B-field away from the z-axis, at the location of a misaligned receiver is naturally divergent from the z-axis and more aligned with the misaligned receiver. While rotating could increase the B-field's alignment, it also increases the distance between the inner plane of the coil and the receiver, which reduces the overall strength of the B-field. As the receiver misalignment becomes more severe past one coil radius, the dynamic transmit coil provides only modest power gains.

For the translational dynamic transmit coil, the highest power gains occurred in the regions of severe translational misalignment. If the receiver was misaligned by more than a coil radius away, the power gains, T, were 3-20 times greater than the static transmit coil. For WPTS with receiver misalignment between zero and one coil radius, the translational dynamic transmit coil produced higher power gains as the receiver misalignment increased. At small radial misalignments, the translational dynamic WPTS provides higher power gains as for more rotationally misaligned receivers. For example,

at zero radial offset, the highest T for the 45 degree misaligned receiver is $T = 1.51$ compared to $T = 1.18$ with the 30 degree misaligned receiver, while at 0.25 radial offset the highest power gain is 1.13 for the 45 degree misaligned reciever compared to a power gain of 1.02 for the 30 degree misaligned receiver.

Although the translational dynamic transmit coils produced the highest power gain, they have the disadvantage of needing a larger footprint than static or rotational dynamic coil WPTS. This larger footprint is necessary for the supports or tracks that the dynamic coil will use to translate. However, if translational misalignment is likely, it could be worth the operational cost of having a dynamic transmit coil with a large footprint.

Comparing the rotational dynamic transmit coil to the translational dynamic transmit coil, one does not consistently outperform the other. For implants with large translational misalignment, greater than half of the transmit coil's radius, the translational dynamic transmit coil outperforms the rotational dynamic coil. For example, in Figure 5.4 it can be seen that for a receiver with an angular misalignment of 30 degrees, the translational coil has a power gain of up to 20, while the rotational dynamic transmit coil highest value of power gain is 1.5. If the angular misalignment increases to 45 degrees, then the translational coil has a power gain of up to 10, while the rotational coil provides very little power gain over a static coil. The rotational dynamic transmit coils perform better for implants with small translational misalignments, less than half a coil radius. For example, in this region for a receiver with θ of 30 degrees, a rotational dynamic transmit coil can provide a power gain of up to 2.98, while the translational dynamic coil can provide a power gain of up to 1.18 as seen in Figure 5.4. The rotation of the transmit coil

helps realign the B-field with the receiver and it also decreases the distance between the receiver and the inner plane of the transmit coil which increases the strength of the B-field. Also, the larger the angular misalignment of the receiver, the better the rotational dynamic transmit coils perform. Either case, however, leads to significant improvement over a static transmit coil.

5.2.4 Control System for Recharging Biomedical Implants

Now that the power gains of a dynamic transmit coil have been modeled, it is necessary to develop a control system that will drive the dynamic transmit coil to its optimal orientation. There are two possible scenarios for biomedical implants, those that have no onboard energy storage (passive implants) and those implants that have onboard energy storage such as batteries (active implants). The dynamic transmit coil is probably more useful for the latter case, where the battery on the active implant allows for a closed-loop controller to be utilized. The closed-loop controller presented in this section is developed for a rotational dynamic transmit coil, which will be built and experimentally validated in the next section. As the transmitter becomes more optimally aligned with the receiver, the voltage across the receiver will increase. The optimally aligned WPTS will increase the recharge rate of the battery. The goal of this controller, shown in Figure 5.5, is to achieve the optimal alignment to reduce the recharge time of the WPTS.

First, the transmit coil should be supplied with the maximum safe current or the maximum current level that will not cause the transmit coil to exceed the magnetic field exposure safety constraints. This current level can be found by using (119). This

controller uses a combination of a feedforward term, θ_f, with a proportional feedback controller to drive the transmit coil to its optimal orientation, which maximizes the voltage, or power, across the ME receiver. Initially, the feedforward term causes the coil to begin rotating. If the rotation causes the voltage across the receiver to increase ($V_{rx_i} > V_{rx_{i-1}}$), the coil continues to rotate in that direction. This rotation continues until the voltage across the receiver starts to decrease ($V_{rx_i} < V_{rx_{i-1}}$), implying that the coil has rotated past its optimal orientation. At this point, the feedforward term is turned off ($\theta_f = 0$), to prevent the coil from oscillating around the optimal orientation and the proportional controller drives the transmit coil back to its optimal orientation.

5.3 Experimental Verification

To verify the modeling results, a rotational dynamic transmit coil was built. The transmit coil is a 7.78 cm radius, 9-turn solenoid coil composed of 16 AWG (1.291mm diameter) copper wire as shown in Figure 5.6. The coil was mounted to a servo motor, Tower Pro MG945, and connected to an Arduino Uno microcontroller. This transmit coil was used for both the dynamic WPTS tests and the static WPTS tests. The servo motor was not used for the static case, and the transmit coil was left in its initial position. For the dynamic WPTS transmitter test, the servo motor rotated the transmit coil to its optimal position.

The receiver for this WPTS is a self-biased ME transducer with dimensions of 13.5 mm x 5 mm x 1.5 mm and consists of two layers of nickel, two layers of Metglas 2605 SA1, and a single layer of PZT. Regular ME transducers typically require a DC bias magnetic field to maximize the efficiency of the WPTS. However, our self-biased ME

transducer receiver uses two different magnetostrictive materials (nickel and metglas) with different permeabilities and coercivities fields, causing differences in saturation magnetization. This difference in saturation magnetizations causes an internal magnetostatic field transverse to the layers. The internal magnetostatic field mitigates the need for an external DC magnetic bias field for the WPTS to operate at its peak efficiency[101]–[103]. The relevant material properties for this ME transducer receiver are listed in Table 5.1.

The ME transducer was placed 5.84 cm (5.84 i.e., 0.75*Coil Radius) away from the center of the transmit coil along the coil's z-axis with an angular misalignment of $\theta =$ 45 degrees. Initially, the radial misalignment, R_{offset}, is equal to zero. The power across a 4.4 kΩ resistor (the optimal impedance for the ME transducer receiver) was measured. The position of the ME transducer was then varied by 1 cm in the coil's radial direction. First, the WPTS was tested with the static transmit coil. The transmit coil was supplied with a current equal to 1.67 amps, with resulted in a maximum effective B-field, $B_{eff} =$ 32 μT, along the center of the transmit coil at $R_{offset} = 0$ cm. The maximum effective B-field was $B_{eff} = 39$ μT which occurred when the receiver's offset was $R_{offset} =$ $0.39 * \text{Coil Radius} = 3.0$ cm.

For the dynamic transmit coil testing, the same transmit coil was supplied with 1.67 amps, and the same experimental procedure was followed. However, at each new ME transducer position, the dynamic transmit coil employed the control system shown in Figure 5.5, to rotate the transmit coil into its optimal position as shown in Figure 5.7. The power across the 4.4 kΩ load resistance was measured once the transmit coil had settled into its final optimal position. For the dynamic transmit coil WPTS, the maximum

effective B-field occurred when $R_{offset} = 0$ cm and was $B_{eff} = 50\ \mu T$. The full experimental results for the static transmit coil WPTS, and the dynamic WPTS are plotted in Figure 5.8. Note that these results are obtained using magnetic fields that are well below half the magnetic field exposure limits. With a reasonable magnetic field of 100 μT, the power output would be quadruple.

The experimental results closely follow the predicted model results, the static transmit coil has a mean and median error of 9.38% and 6.51% respectively, while the dynamic transmit coil has a mean and median error of 9.08% and 7.27% respectively. Figure 5.9 shows how the dynamic transmit coil produces significant power gains for misaligned ME receivers when $R_{offset} < \frac{1}{2}$, which follows the predicted values for the power gain, T, shown in Figure 5.4

5.3.1 Discussion

In this work, we have outlined the benefits of adding a simple servo motor system to transform static transmit coils into dynamic transmit coils to increase the overall efficiency of the WPTS. The increase in efficiency is helpful for two cases. The first is for passive implants, when the misalignment causes the implants not to receive enough power to function. The following example illustrates the benefit of the dynamic transmit coil for this case. Using the transmit coil outlined in the Experimental Results section and assuming that an implant needs 20 uWs to function, a static transmit coil will only be able to deliver sufficient power to a ME transducer with no angular misalignment $\theta = 0$ in an approximately 86.7 cm^3 region. The same WPTS can deliver sufficient power to an approximately 151 cm^3 region by adding a servo motor and using the dynamic transmit

coil. If there is angular misalignment as well, for example, if θ=45, the static transmit coil can supply adequate power in a 131 cm^3 region, while the dynamic transmit coil can supply adequate power in a 181 cm^3 region.

The second case is for recharging the implant's batteries. Assuming an identical load and ME receiver, a dynamic transmit coil WPTS with a power gain of $T = 2$ leads to a decrease in charging time of 41% ($\sqrt{2} = 1.41$) over a static coil system. The rotational dynamic WPTS in the experimental validation section, with a ME transducer misaligned by 45 degrees and at $R_{offset} = 0$ cm, the dynamic transmit WPTS exhibited a $T = 2.43$. If the load was charging a 5 mAhr battery, the dynamic transmit coil would fully charge the battery in 3.22 minutes, while the static transmit coil system would need 5.04 minutes to fully charge the same battery, a 56 percent increase in required charging time.

5.4 Conclusion

This chapter presents a novel way to increase the efficiency for WPTS with misaligned receivers, specifically for biomedical implants using ME transducers. Using a single solenoid transmit coil that uses servo motors, which we call a dynamic transmit coil, to alter its position/orientation allows the WPTS to alter the directionality of the B-field at the receiver without violating magnetic field safety constraints. This dynamic transmit coil outperforms identically constructed static transmit coils and delivers higher power to systems with misaligned receivers. We modeled how rotational dynamic transmit coils can provide up to 3 times the power gain over static coils. Additionally, translational dynamic transmit coils can deliver power gains up to 10- 20x for systems

with severe misalignment.

A rotational dynamic transmit coil was built to validate the power gains shown by the model experimentally. Two control systems were presented. The first allows the dynamic transmit coil to sufficiently power passive implants. The second optimally aligns the dynamic transmit coil to maximize the power transfer and reduce recharging times for implants with batteries. Using a ME transducer receiver with various radial misalignments and an angular misalignment of 45 degrees, the dynamic transmit coil experimentally provided up to 2.4 times the amount of power to the misaligned receiver compared to a static transmit coil for some areas of misalignment but produced better or equal power gains for all ME receiver misalignment locations.

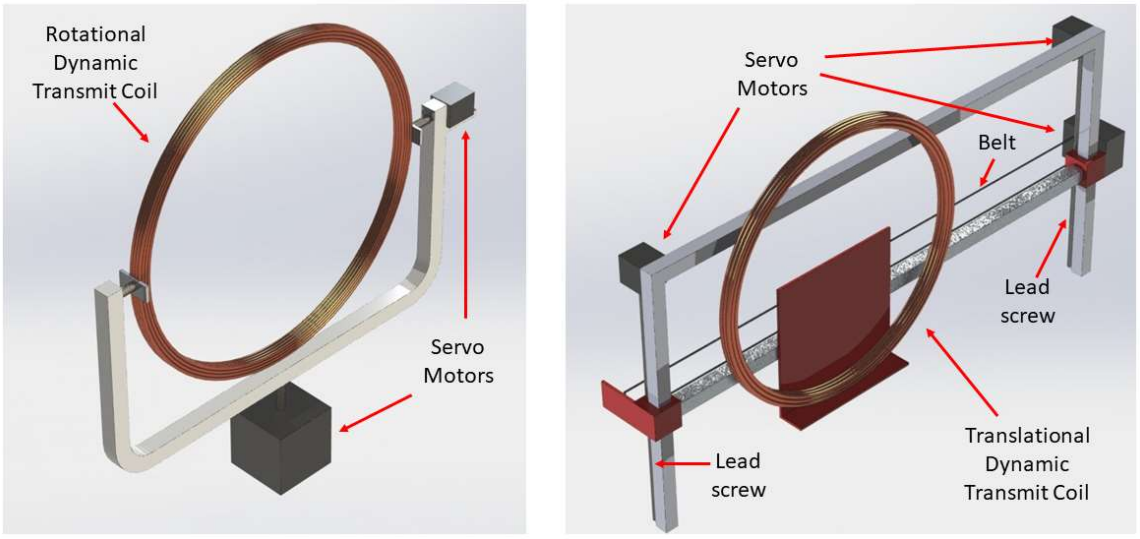

Figure 5.1 An example of a dynamic transmit coil. The dynamic transmit coil consists of a single solenoid coil whose position/orientation is controlled through servo motors. Left) An example of a rotational dynamic transmit coil. Its servo motors rotate the coil about the motor's fixed axes. Right). An example of a translational dynamic transmit coil that uses servo motors with a belt and lead screw system to shift the position of the solenoid transmit coil.

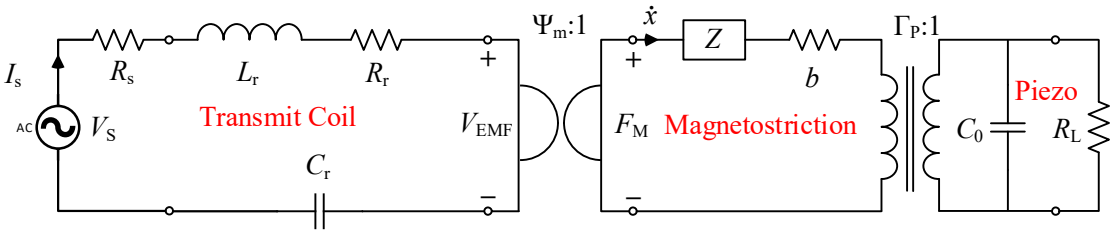

Figure 5.2 The equivalent circuit diagram of a ME WPTS. The transmit coil is an electrical system with some parasitic inductance, resistance, and capacitance. The ME transducer receiver is composed of two mechanical systems which have some impedance and damping. And the piezoelectric component has some equivalent capacitance.

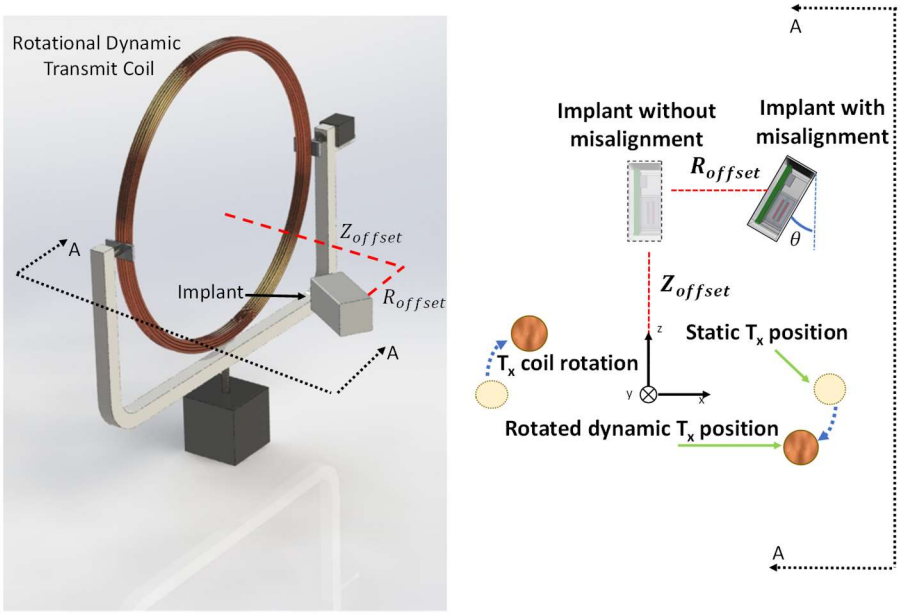

Figure 5.3 A 3D view (left) and planar cross-sectional view from the top (right) of the static and dynamic WPTS. The circles represent the cross-sectional area of the different transmit coils. The 3D view shows a rotational dynamic transmit coil. The global coordinate frame is in defined in the center of the static transmit coil, which is equal to the initial position of the dynamic transmit coil. The ME transducer WPTS receiver is located at some distance along the coil's z-axis, Z_{offset}, and some distance along the coil's radial axis (x-axis), R_{offset}. Additionally, the receiver can be misaligned with the static transmit coil by some angle θ which is defined by the angle between the receiver's longitudinal direction and the global z-axis. The position of the static transmit coil is shown, as well as a possible position for the dynamic transmit coil. A rotational dynamic transmit coil (copper color) rotates about the y-axis to its optimal position, where the alignment of the B-field and the ME receiver maximizes the power available to the load[104].

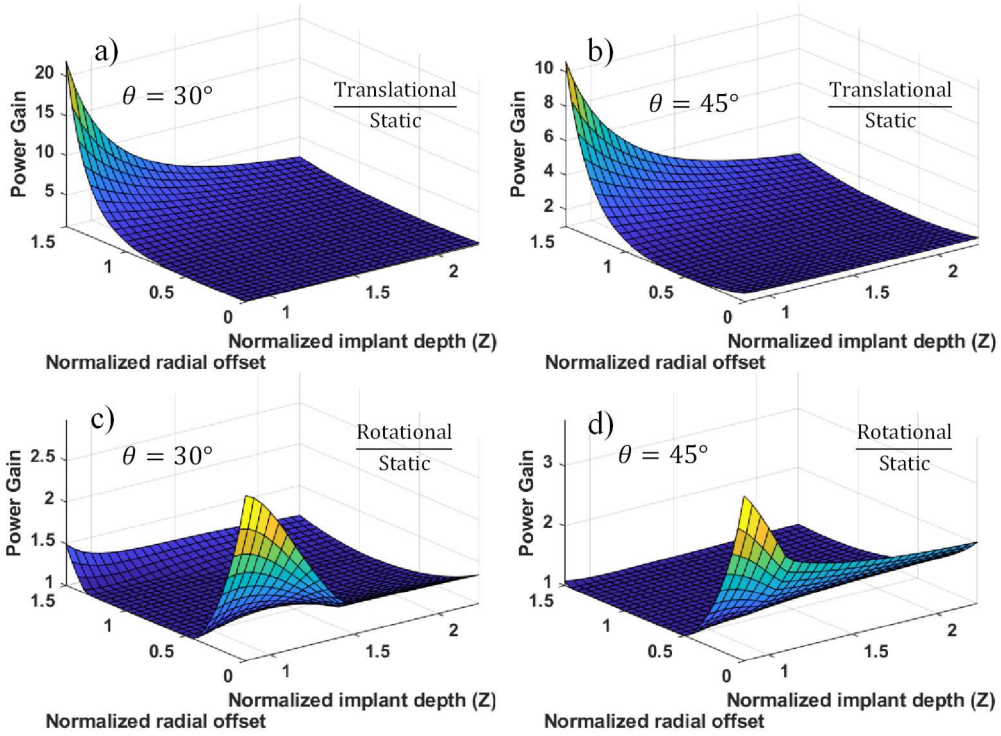

Figure 5.4 The power gain, T, for a dynamic transmit coil WPTS compared to a static transmit coil WPTS for an ME transducer receiver located at various points in an xz plane located at a y value equal to the center of the transmit coil. The normalized implant depth is the z-direction and the normalized radial offset is the x-direction using the axes definitions given in Figure 5.3. a) The power gains of a translational dynamic transmit coil vs a static transmit coil with the receiver misaligned by 30 degrees. b) The power gains of a translational dynamic transmit coil vs a static transmit coil with the receiver misaligned by 45 degrees. c) The power gains of a rotational dynamic transmit coil vs a static transmit coil with the receiver misaligned by 30 degrees. d) The power gains of a rotational dynamic transmit coil vs a static transmit coil with the receiver misaligned by 45 degrees. The distances have been normalized by the radius of the transmit coil. The dynamic transmit coils equal or outperform the static coils in every case. Note, the scales are different for each graph. However, all the normalized implant depth starts at 0.75 and the power gain scales starts at 1 for all graphs.

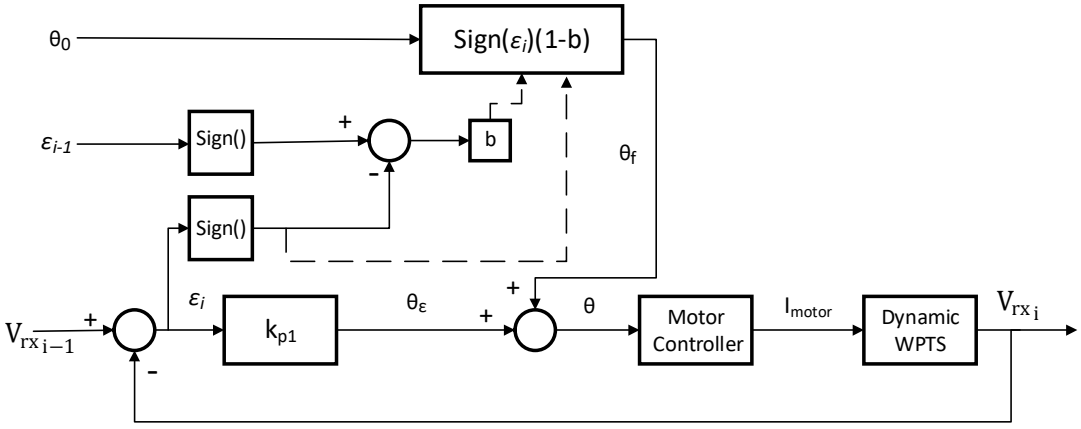

Figure 5.5 The controller for recharging biomedical implants with batteries. The controller uses feedback control to drive the dynamic transmit coil into its optimal orientation, maximizing the voltage across the ME receiver. This version of the controller uses a feedforward term, θ_f, to quickly drive the dynamic transmit coil into its optimal orientation, at which point it is turned off to prevent the system oscillating around the optimal orientation.

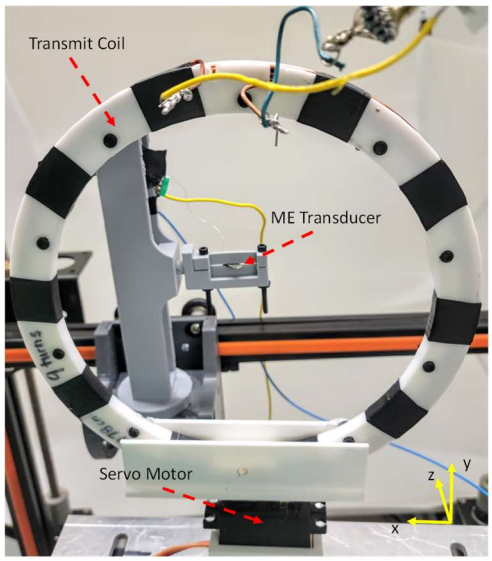

Figure 5.6 The experimental setup with a rotational dynamic transmit coil. A servo motor turns the coil to its optimal position. The self-biased ME transducer is placed at a misalignment angle of 45 degrees. A 3-D printer (composed of aluminum to not interfere with the magnetic waves) moves the ME transducer along the radial axis (x-axis). The power is measured at each ME transducer location across an optimal load resistor of 4.4 kΩ .

Table 5.1 ME transducer receiver properties

$f_0 = \frac{\omega}{2\pi}$	179.9kHz
Q	105.8
m	$4.18x10^{-4}$ kg
$d_{31,p}$	$190x10^{-12}$ $\frac{\text{m}}{\text{V}}$
s_{11}^{E}	$1.51x10^{-11}$ $\frac{1}{\text{Pa}}$
C_0	1.3 nF

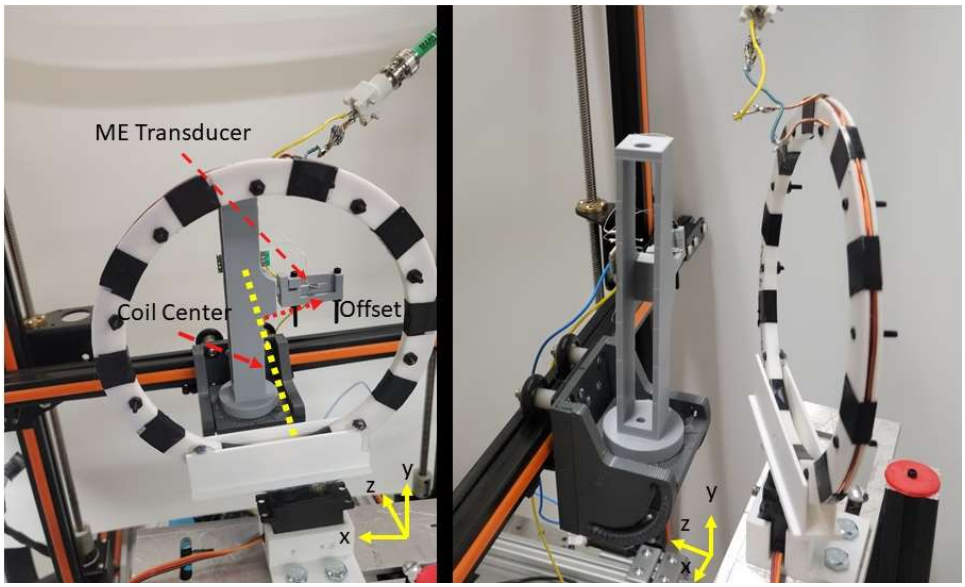

Figure 5.7 The experimental setup. Left) The ME transducer had a constant Z_{offset} displacement of 5.84 cm while the radial offset was varied. Right) The dynamic transmit coil rotates into its optimal position to compensate for the receiver misalignment.

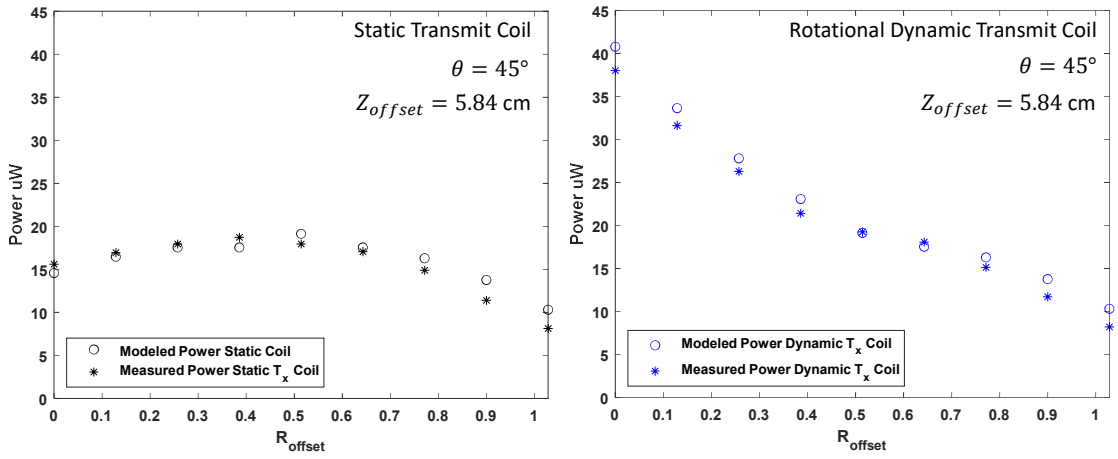

Figure 5.8 Experimental results versus theoretical results for the ME WPTS. Left) Experimental power output versus modeled power output using (125) for a static WPTS to a ME transducer located at $Z_{offset} = 5.84$ cm with angular misalignment $\theta = 45$ degrees. Right) Experimental power output versus modeled power output for a rotational dynamic WPTS to a ME transducer located at $Z_{offset} = 5.84$ cm with angular misalignment $\theta = 45$ degrees.

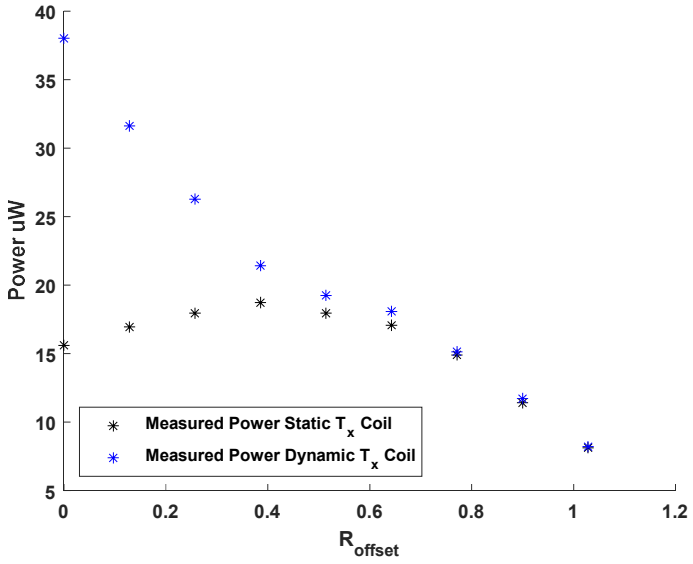

Figure 5.9 Experimental results of a rotational dynamic transmit coil versus a static transmit coil for a ME transducer located at $Z_{offset} = 5.84$ cm with angular misalignment $\theta = 45$ degrees.

CHAPTER 6

MAGNETOELECTRIC WIRELESS POWER TRANSFER SYSTEM DEMONSTRATION AND CHARACTERIZATION

In this chapter, we build and characterize a self-biased ME WPTS for a biomedical implant and compare our device to other ME, RF, and MF WPTS for biomedical devices.

6.1 Introduction

With the development of an optimal design process for a WPTS transmit coil for biomedical implants and a method to increase the efficiency of a WPTS for misaligned biomedical implants, the next step is to build and characterize a full wirelessly powered sensor system. While there is a wide range of functionally for biomedical sensors, ranging from glucose sensors to pacemakers, we choose to design a temperature sensor as a suitable proof of concept demonstration for the effectiveness of our ME WPTS.

Ideally, implantable biomedical sensors should be small, making them easier to insert via noninvasive surgery and increasing the regions inside the body that are potentially compatible with the device. Furthermore, the device should operate at low power since space for energy storage will be at a premium. And the longer the implant can operate without a recharge, the more valuable it can be. Additionally, because the implant will be recharged wirelessly, it should have efficient power conditioning circuity.

And lastly, transmitting the sensor data wirelessly is essential for the implant to be useful.

This chapter describes the overall system design of the ME WPTS and a low-powered biomedical temperature sensor. The ME WPTS system is characterized, and each step's power loss and efficiency are determined. The ME WPTS is then used to power a biomedical implant composed of an MCU, temperature sensor, and Bluetooth radio. This work is compared with other state-of-the-art ME, RIC, and MF WPTS designed explicitly for biomedical applications. We see that ME WPTS generally perform equal to RIC and MF for powering small biomedical implants.

6.2 System Design and Experimental Validation

6.2.1 ME Receiver Design

ME transducer receivers for optimal wireless power transfer usually require a large external DC bias field. This DC bias field is generally accomplished through permanent magnets attached near the ME transducer. However, for implantable biomedical applications, installing large permanent magnets poses a health risk for the patient. Therefore, a self-biased ME transducer was built, shown in Figure 6.1, that mitigates the need for an external bias field [105].

The self-biased ME receiver is a 5-layer device composed of two layers of Metglas, two layers of nickel, and a single layer of PZT 5A. The dimensions of each layer are given in Table 6.1.

6.2.2 Power Electronics and Low Powered MCU Design

Because of the potential for low coupling and hence low voltage produced in the ME WPTS, a voltage doubler (VD) rectifier was built. The VD rectifier consists of two Infineon Technologies BAT15-03W Schottky diodes with a typical forward voltage drop of 0.25 V and two 10 nF capacitors. These diodes were chosen because of their low voltage drop and small self-capacitance, 0.4 pF.

The rectified voltage is passed into an EPEAS AEM30940 energy harvesting chip. The EPEAS AEM30940 boosts or bucks the voltage to the appropriate level (3.3 V) for the MCU. The EPEAS chip was chosen because of its low minimum DC voltage input, 50 mV, and its low cold-start power requirement, 3 μW. In addition to boosting the voltage, the EPEAS chip also actively manages the power output to the MCU. If the MCU is consuming less power than is inputted via the ME receiver, then the excess power is stored in a storage capacitor. If the MCU requires more power than is being inputted, then the EPEAS chip draws the necessary current from the storage capacitor. The output voltage of the EPEAS is programable and can be set between 1.2 and 3.3 V. The MCU is an ATmega328P modified to operate in a low power state. When the MCU is not sampling or transmitting data, all functionally of the chip is shut down except for the clock circuit. The temperature sensor is an Analog Device TMP36. The MCU transmits the sensor data via a low powered NRF24L01 2.4 GHz radio. The system setup is shown below in Figure 6.2.

6.2.3 Transmit Coil System Description

The transmit coil is a 7.78 cm radius, nine turn, flat solenoid coil composed of 16 AWG (1.219 mm diameter) copper wire as shown in Figure 6.3. An E&I 240L class A linear power amplifier was used to supply the transmitter coil with a high–frequency current. At 5 cm, the maximum B-field for this WPTS is 50 μT. At 2 cm, the maximum B-field for the WPTS is 80 μT. The maximum B-field is constrained by the maximum power output of our RF power amplifier. The transmit coil was not designed to be optimal. Having an optimally designed transmit coil would decrease the amount of power needed to produce the B-field at each location but would not alter the power produced by the ME WPTS for a given B-field.

6.2.4 Power Requirements and System Power Losses

Once turned on, the MCU requires 66 μW of power in its low power state. Reading the temperature via the TMP36 requires only 1.5 μW of power. The largest power requirement for the wireless biomedical sensor is transmitting the data via the low-power Bluetooth radio, which requires 99 μW.

The system power losses for the ME receiver when exposed to a 50 μT B-field are shown in Table 6.2.

At this B-field level, there is a significant loss of power in both the EPEAS chip and the VD rectifier. Most of the VD rectifier's power losses can be accounted for by the forward voltage drop of the two diodes. The EPEAS chip boosting the voltage to 3.3 V is the least efficient step, and the overall system efficiency is 38%. With the low input power of the ME receiver at 50 μT, the EPEAS chip is much more efficient, boosting to

1.8V (at this voltage level, the step efficiency to boost to 1.8Vs was 95%). However, the Bluetooth radio transmitter needs 3.3 V to operate, which is why the 3.3V output is required. Note, the optimal load for the EPEAS was found to be the minimum resistance that the EPEAS chip could maintain a designated constant voltage output (e.g., below 310000 Ω, the voltage across the resistor would not be able to be held at 3.3 V, but would periodically drop below the set output level).

Increasing the B-field to 80 μT improves the efficiency of the ME WPTS, as shown in Table 6.3.

With the higher B-field and subsequent higher voltage across the ME transducer, both the VD rectifier and the EPEAS chip efficiencies increase. Again, most of the power loss in the VD rectifier can be attributed to the forward voltage drop of the diodes. With the higher WPTS efficiency at this B-field, the ME transducer can directly power the biomedical sensor.

6.2.5 Full System Implementation and Experimental Validation

To validate the system power requirements, the full ME WPTS sensors system was demonstrated and power generation characterized. The ME receiver was placed 2 cm from the cross-sectional plane of the transmit coil. A simplified circuit diagram of the receiver is shown in Figure 6.4 . The transmit coil was supplied with 1.26 A of current at 179 kHz, which induced a B-field of 80 μT at the ME receiver. The B-field produced an AC voltage in the ME receiver which was rectified through the VD rectified. The rectified voltage was boosted to 3.3 V through the EPEAS chip. The EPEAS chip produced a current of 20 μA to power the MCU, I_L. By measuring the change in the

voltage, ΔV, over time, Δt, across the storage capacitor, C_s, I_s was calculated according to

$$I_s = C_s \frac{\Delta V}{\Delta \mathrm{t}}. \qquad (130)$$

When the storage capacitor value C_s is 1 mF, $\frac{\Delta V}{\Delta t} = \frac{0.32}{7.4s}$ which gives $I_s = 43.2\ \mu A$. The total power going out of the EPEAS chip can be calculated by $V_{MCU} * I_L + V_{C_s} * I_s$, which is equal to 221.5 µW.

The 221.5 µW of power delivered to the load was sufficient to power the MCU, even when transmitting its sensor data via the Bluetooth radio. The MCU successfully read and wirelessly transmitted the temperature sensor's reading to a laptop with a receiver station set up nearby. The power calculated here is slightly greater than the power previously calculated in the system power loss section. This slight difference in power is probably a result of the RF power amplifier dynamics, whose current output level varies slightly over time.

6.3 Comparison of ME, MF, and RIC WPTS for Biomedical Implants

6.3.1 Comparison Of ME WPTS for Biomedical Implants

To compare our ME WPTS to other WPTS designed explicitly for biomedical implants, we define a figure of merit, F_{ME}, that normalizes the power by the device's volume and the WPTS B-field,

$$F_{ME} = \frac{P_L}{V_{rx} B^2 \omega} \qquad (131)$$

where P_L is the power delivered to the load for the WPTS and V_{rx} is the volume of the receiver, B is the strength of the B-field at the receiver and, ω is the operating frequency

of the ME WPTS. F_{ME} is defined in $WsT^{-2}m^{-3}$. The comparative analysis shown in Table 6.4 shows that our device performs very well compared with other ME WPTS. The only ME WPTS that had a higher F_{ME} was a larger Galfenol-PZT device [22] that required a large DC bias field produced by large (relative to the receiver size) permanent magnets to achieve its high-power gain. Even then, our self-biased device has a F_{ME} only 47.7% lower with the bias field coming from the device's internal structure. If a biomedical sensor were to be built out of a non-self-biased ME receiver, then it would be essential to consider the volume of the permanent magnets that would be needed to define the overall volume of the complete ME transducer receiver.

6.3.2 Comparison of ME, RIC, and MF WPTS

The comparison of this work and other state-of-the-art WPTS for biomedical implants is given below in Table 6.5. The table is broken into three categories midfield (MF), resonant inductive coupling (RIC), and magnetoelectric (ME) WPTS. MF WPTS typically operate in frequency ranges that are considered higher than near-field inductive WPTS but not yet far-field radiative power transfer. If fully defined in the article, the receiver's volume is given; otherwise, the area of the receiver is reported for the receiver size. For ME WPTS, the volume of the device is consistently reported, but RIC and MF WPTS often just report the receiver size has an area not a volume. For RIC and MF WPTS, the efficiency of the WPTS is recorded. ME WPTS do not generally give efficiency numbers. Rather, when comparing ME WPTS, the power is normalized by the B-field (i.e., as shown in F_{ME}) which is reported instead of efficiency. Additionally, we define another figure of merit

$$F_{RF} = \eta * d^2 \qquad (132)$$

where η is the efficiency of the WPTS and d is the wireless power transfer distance that is reported for both the MF and RIC WPTS. For the ME WTPS, F_{ME} is recorded instead. Note, ϕ is the receiver's diameter.

Plotting F_{RF} of the WPTS versus the area of the receiver, we see that the efficiency normalized by transmit distance, F_{RF}, decreases as a function of the receiver's area, as shown in Figure 6.5. (For those systems that reported volume, the largest cross-sectional area of the receiver was used in this analysis.)

6.3.3 Discussion

Directly comparing ME, RIC, and MF WPTS found in literature is difficult because there is no straightforward way to convert between efficiency (which is often reported in RIC and MF WPTS but not in ME WPTS) and B-field at the receiver (which is often reported in ME WPTS but not in RIC and MF WPTS). So, directly comparing published RIC and ME WPTS is not really possible without making many assumptions. However, from Table 6.5 we can take note of some general trends. RIC systems are the most efficient but generally operate at very small distances. MF are small and operate at larges distances, but they have poor efficiency and deliver low power to the load. The ME WPTS delivered similar levels of power to the implant as both the RIC and MF WPTS.

Additionally, Figure 6.5 shows the importance of receiver size. As the implants get smaller and deeper into the body, the efficiency of the inductive WPTS drops significantly. While we acknowledge that receiver volume, not area, would be the ideal

comparison, the lack of reported receiver volume in MF and RIC WPTS prevented this analysis.

It is important to note that the power delivered to the load may be a more critical metric than the system efficiency for biomedical implants. The power delivered to the load, not the overall system efficiency, determines whether the implant can operate. Additionally, because of the safety constraints for wirelessly transmitting power through the human body, the power delivered to the load cannot simply be increased by increasing the power in the transmitter. Most of the MF and RIC systems did not report any safety considerations or analysis in their articles, making it harder to directly compare the different RIC and MF WPTS to each other and the ME WPTS.

Because the ME WPTS directly report their B-field, we can see which of the ME WPTS operate above the magnetic field exposure reference levels. Using the IEEE reference levels, both [23], [25] operate at higher B-fields than the prescribed safety level. Because the ME WPTS power output scales with the magnetic field squared, our ME WPTS could increase its power by 2.03x if we operated the WPTS at 114 μT, which is the safety constraint at 179 kHz. Additionally, if our ME receiver resonant frequency could be shifted down to 100 kHz and below while maintaining its quality factor, the magnetic field safety constraint would rise to 615 μT leading to a potential increase of 59x to the power delivered to the load.

6.4 Conclusion

In conclusion, a self-biased ME WPTS for a biomedical implant was successfully built and characterized. The self-biased ME receiver can deliver 389 μW of power to an

optimal resistive load with a B-field of 80 μT. The designed power conditioning electronics achieved an end-to-end efficiency of 60%, resulting in 221.5 μW being used to power an implant that senses the temperature and successfully transmits its data wirelessly through a Bluetooth antenna. This demonstration shows the potential usefulness of small ME transducer receivers to power biomedical implants, especially for biomedical device companies and research funding institutions. Future work will involve taking the bench top demonstration of the ME WPTS and miniaturizing it into an mm-scale biomedical implant. This future work would include designing the PCB (which would likely require custom ASIC development to meet the size constraints), the ME receiver's clamping mechanisms, and the implant's biomedical-grade casing.

In addition to the device demonstration, a comparison was made between our ME WPTS to other ME WPTS designed for biomedical implants. Our ME WPTS performed better than all but one ME WPTS when the power delivered to the load was normalized by device's volume and B-field. Additionally, since our device is a self-biased ME transducer, it would not need additional volume in the implant for large permanent magnets.

We also compared ME, MF, and RIC WPTS designed for biomedical implants and found that no one WPTS is definitively better for powering biomedical implants. All of the different WPTS can provide power capable of operating a device on the order of mW or hundreds of μWs to mm-sized receivers. However, for inductive WPTS, the efficiency normalized by transmit distance decreases as the receiver size decreases, potentially leading to poor power delivered to the load for small or deep biomedical implants. These results lend further evidence that ME transducers can be an attractive

option to power small biomedical implants, especially if they are implanted deep in the body.

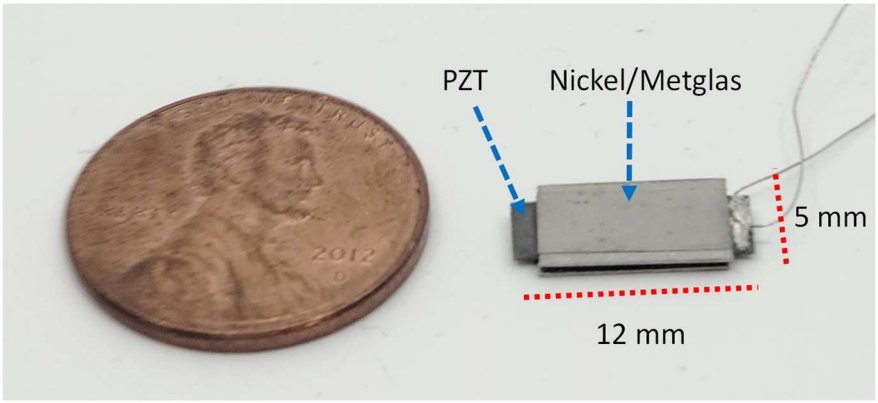

Figure 6.1 The self-biased ME transducer receiver is a 12 x 5 x 1.05 mm^3 composite beam composed of PZT, nickel, and Metglas.

Table 6.1 The self-biased ME transducer receiver

Materials	Length, mm	Width, mm	Thickness, mm
PZT-5A	12.36	3.81	0.5
Nickel	10.16	5	0.25
Metglas	10.16	3.81	0.023

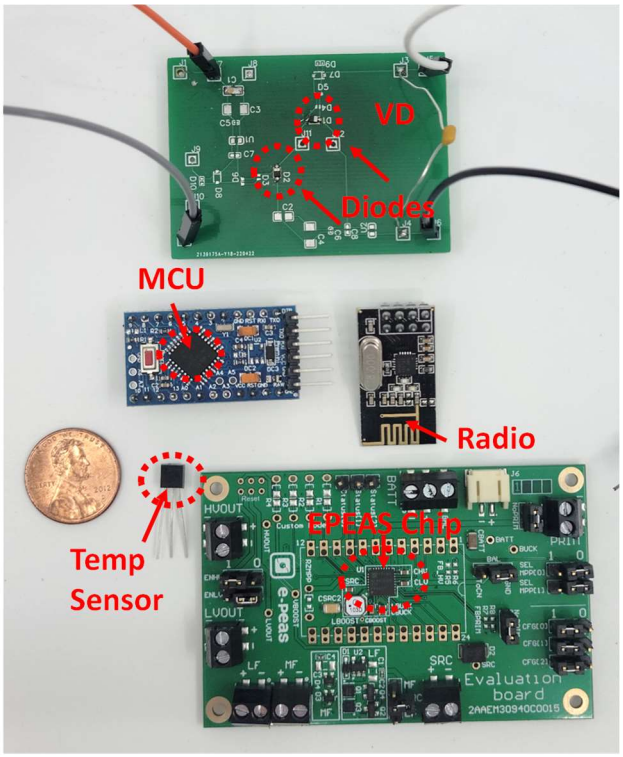

Figure 6.2 The power conditioning electronics and MCU, temperature sensor, and Bluetooth radio. The large printed circuit boards (PCBs), evaluation boards, and jumper cables are done for ease in the prototyping process.

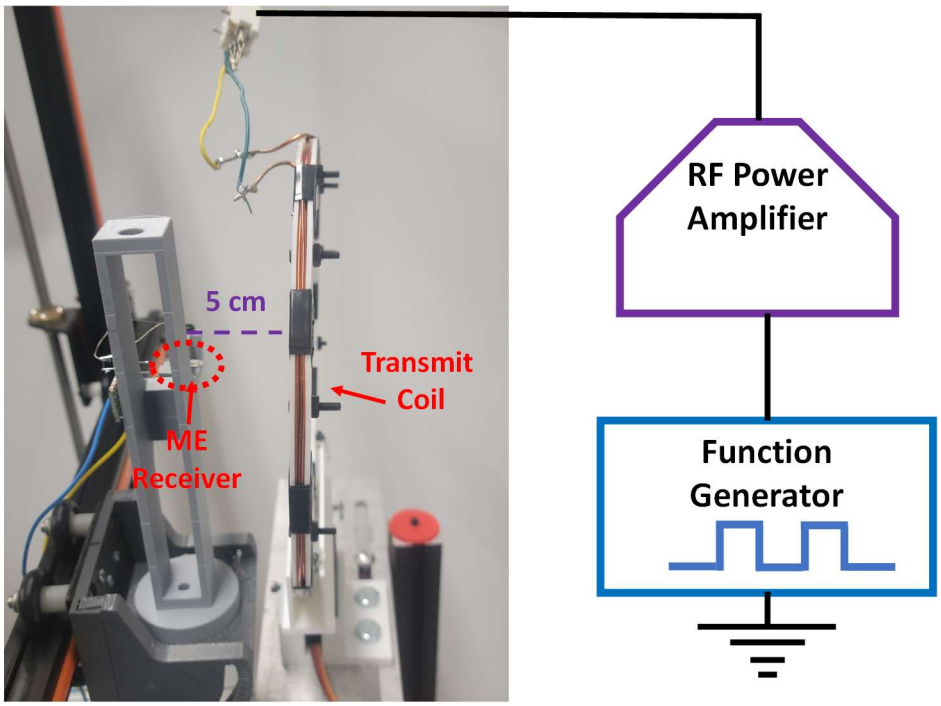

Figure 6.3 The setup of the ME WPTS and the 7.78 cm radius, nine turn, flat solenoid transmit coil. The function generator inputs a signal to the RF power amplifier, which excites high-frequency current in the transmit coil creating a B-field at the ME receiver.

Table 6.2 Stepwise system power losses for ME WPTS at 50 μT

	Optimal Load (Ω)	Voltage (V -RMS)	Power (μW)	Step Efficiency	Overall Efficiency
No rectifier	4400	0.637	92.13	X	X
VD rectifier	35000	1.48	62.6	0.68	X
VD rectifier with EPEAS	310000	3.3	35.1	0.56	0.38

Table 6.3 Stepwise system power losses for ME WPTS at 80 μT

	Optimal Load (Ω)	Voltage (V -RMS)	Power (μW)	Step Efficiency	Overall Efficiency
No rectifier	4400	1.24	349	X	X
VD rectifier	35000	3.1	275	0.79	X
VD rectifier with EPEAS	52300	3.3	208	0.76	0.60

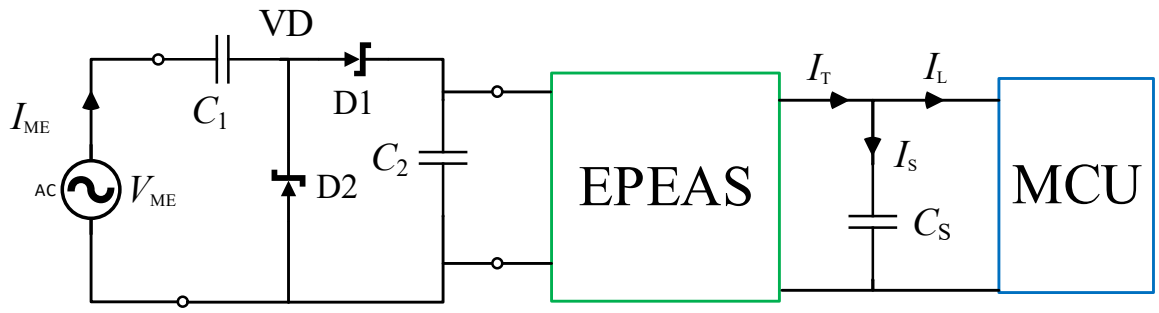

Figure 6.4 A simplified circuit diagram of the receiver side of the ME WPTS. The ME receiver is an AC voltage source that is rectified through the VD rectifier. The DC current is then passed into the EPEAS chip which outputs a total current, I_T, which powers the MCU with I_L. The excess current, I_s, charges a storage capacitor, C_s.

Table 6.4 Comparison of ME WPTS for biomedical implants

Article	Method	Frequency	Receiver Size	P_L	B-field (μT)	F_{ME} (MWs/T^{2}m^3)
[22] 2019	ME	150 kHz	10 x 20 x 1.76 mm^3	5 mW	101	9.283
[23] 2019	ME	202 kHz	10 mm ϕ x 2.4 mm	19.5 mW	1000	0.512
[24] 2019	ME	70 kHz	10 x 20 x 2.035 mm^3	600 μW	600	0.059
[25] 2008	ME	60 kHz	41 x 20 x 0.3 mm^3	160 mW	2000	2.694
Our Work 2022	ME	179 kHz	12 x 5 x 1.05 mm^3	349 μW	80	4.854

Table 6.5 Comparison of WPTS for biomedical implants

Article	Method	Frequency	Receiver Size	Distance	P_L	Efficiency (B-field)	F_{RF}	F_{ME}
[34] 2010	MF	1 GHz	2 x 2 x 0.04 mm^3	40 mm	150 µW	0.20%	3.2e-6	NA
[6] 2014	MF	1.6 GHz	2 mm ϕ	50 mm	200 µW	0.04%	1.0e-6	NA
[42] 2021	MF	2.5 GHz	12 x 12 x 3 mm^3	190 mm	20 mW	0.50%	1.81e-4	NA
[5] 2016	RIC	200 MHz	1 mm ϕ x 1 mm	12 mm	224 µW	0.56%	8.06e-7	NA
[33] 2011	RIC	8 MHz	10 mm ϕ x 0.2mm	10 mm	10 mW	24.60%	2.46e-5	NA
[8] 2013	RIC	13.56 MHz	25 x 10 x 0.5 mm^3	10 mm	10 mW	58%	5.80e-5	NA
[9] 2016	RIC	13.56 MHz	42 mm ϕ	10 mm	10 mW	89%	8.9e-5	NA
[35] 2018	RIC	11 MHz	5 mm ϕ x 1mm	52 mm	1.0 mW	47.8%	1.30e-3	NA
[38] 2012	RIC	256 kHz	15 mm ϕ	10 mm	14 mW	5%	5.0e-6	NA
[39] 2018	RIC	800 kHz	70 mm ϕ	10 mm	25 W	90%	9.0e-5	NA
[40] 2015	RIC	13.56 MHz	8 x 8 mm^2	5 mm	105 mW	65.8%	1.65e-5	NA
[106] 2022	RIC	6.78 MHz	3 mm ϕ x 10 mm	20 mm	600 µW	5.3 %	2.12e-5	NA
[22] 2019	ME	150 kHz	10 x 20 x 1.76 mm^3	0 mm	5 mW	101 µT	NA	9.28
[23] 2019	ME	202 kHz	10 mm ϕ x 2.4 mm	0 mm	19.5 mW	1000 µT	NA	0.51
[24] 2019	ME	70 kHz	10 x 20 x 2.035 mm^3	0 mm	600 µW	600 µT	NA	0.05
[25] 2008	ME	60 kHz	41 x 20 x 0.3 mm^3	30 mm	160 mW	2000 µT	NA	2.69
Our Work 2022	ME	179 kHz	12 x 5 x 1.05 mm^3	20 mm	349 µW	80 µT	NA	4.85

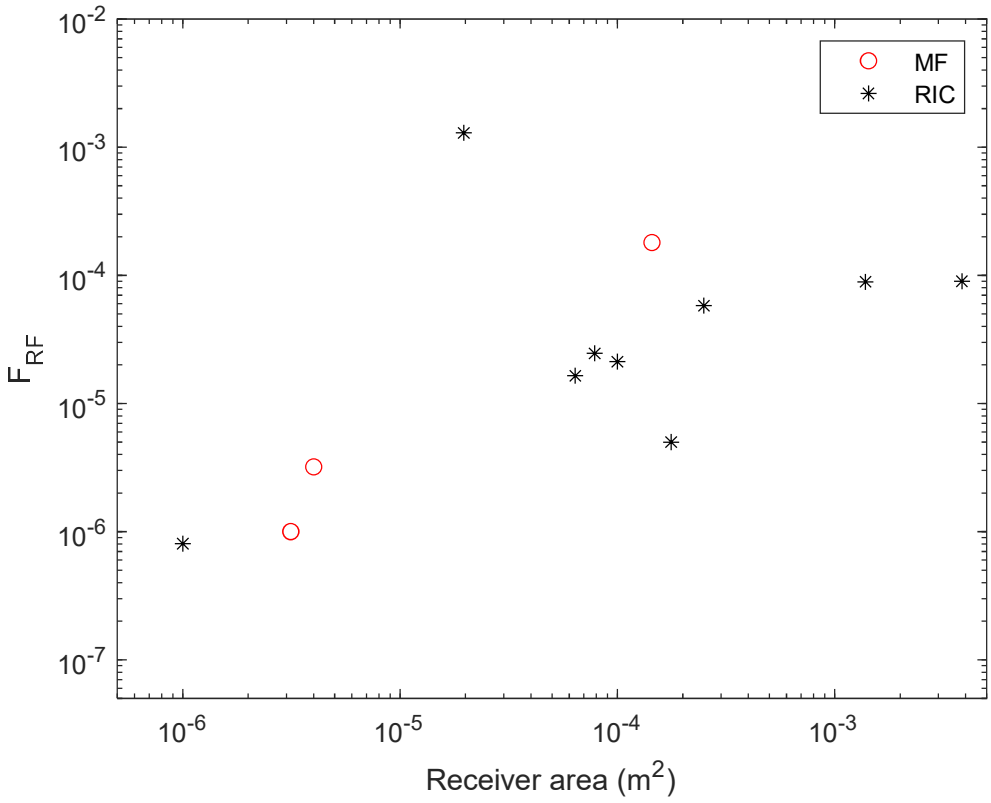

Figure 6.5 Normalized efficiency F_{RF} for MF and RIC WPTS. There is a positive correlation between the receiver size and F_{RF}. Note the logarithmic scales on both axes.

CHAPTER 7

CONCLUSION AND FUTURE WORK

This dissertation has centered on improving wireless power transfer to small biomedical implants. We examined how choosing the operating frequency affects the wireless power transfer for low coupled WPTS. Both low coupled RIC and ME WPTS rely on the B-field as the mechanism for wireless power transfer, and both systems' power scales with the B-field squared. Additionally, for RIC WPTS, the power increases with the frequency squared, making operating frequency an important parameter for designing RIC WPTS. However, for ME WPTS and nonresonant inductive WPTS, the power scales linearly with frequency, making maximizing the B-field the more critical parameter in these WPTS.

But when transmitting power wirelessly through the body, it is important to follow the magnetic field exposure safety constraints. The two main bodies that set exposure limits for non-ionizing RF exposure, IEEE and ICNRIP, both have safety standards that decrease the allowed magnetic field exposure as the frequency of the WPTS increases. Because maximizing the B-field is essential for small receiver WPTS, which will have very low coupling between the receiver and transmitter, we developed an optimal design process for the WPTS that maximizes the B-field at the receiver while adhering to safety, size, and power constraints. Additionally, this insight, combined with the effect of frequency on the different WPTS, allows us to optimally design WPTS at

frequencies where the power transfer will be maximized.

For ME WPTS, power scales with the square of the B-field and linearly with frequency, $P_{ME} \propto B_{field}^2 \omega$. By taking the IEEE magnetic field exposure limit and multiplying it by the operating frequency, we can find the optimal operating frequency for ME WPTS. As shown in Figure 7.1, the optimal operating frequency that leads to the maximum theoretical power output for an ME WPTS would be 100 kHz. After 100 kHz, the maximum theoretical power outputs for an ME WPTS drops due to the significant decrease in allowable B-field.

Maximizing wireless power transfer to biomedical implants requires dealing with the likely misalignment between the receiver and transmitter. Once implanted, the exact orientation of the implant will be unknown, and both RIC and ME WPTS suffer a loss of efficiency as an effect of receiver misalignment. We developed a novel method to minimize transmitter-receiver misalignment using a dynamic transmit coil. The dynamic transmit coil can increase the power gain of a WPTS with a misaligned receiver by 2-3x, and it can operate without any a priori knowledge of the receiver's orientation. Additionally, because it consists of a single flat solenoid coil, it is easy to ensure that the B-field inside the body is under the magnetic field exposure limits.

To help experimentally validate these findings, two WPTS were built. The first was a RIC WPTS, which used the optimal design process to deliver 997 mW across a 100 mm gap and could successfully power an MCU even with 60 degrees of angular misalignment between the receive coil and transmit coil. This RIC WPTS was successfully integrated into a knee sensor built by our collaborators at the University of Freiburg (IMTEK) and then used in experimental trials.

The second WPTS was a self-biased ME receiver WPTS that, when supplied with 80μT at its resonant frequency of 179 kHz, produced 349 μW of power. When normalized by its volume and B-field, our device performed better than all other state of the art ME transducers built for powering biomedical implants expect for a Galfenol-PZT device that used large external biasing magnets. A low-powered biomedical temperature sensor was built that consumed on average 66μW of power, which only briefly spiked to 99 μW when transmitting its data via Bluetooth radio. Charging a small battery or supercapacitor with our ME WPTS for 1 hour would allow approximately 5.3 hours of runtime for the biomedical sensor. If the B-field of the ME WPTS was increased to the IEEE exposure limit of 114 μT, a 1 hour charge would allow a 10.6-hour runtime for the sensor. However, suppose the resonant frequency of our ME receiver could be lowered to 100 kHz, possibly by reducing the width of the receiver and increasing its length while holding its thickness constant. In that case, the maximum safe B-field exposure limit rises to 615 μT. At this B-field level, the ME receiver power output is 59x greater, implying a one-hour charge would allow 312 hours (13 days) of continuous operation of the biomedical sensor. This level of wireless power transfer to a small mm-sized implant can potentially decrease the size of current biomedical implants and increase the functionality of new small biomedical implants that can help diagnose and treat a wide range of ailments.

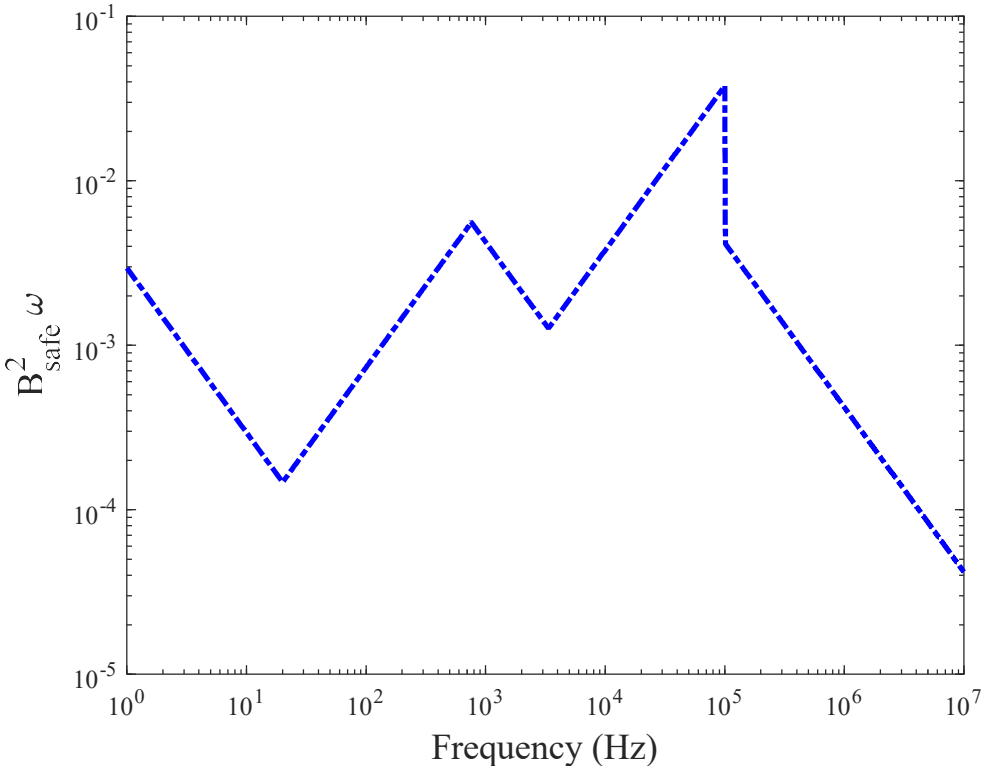

Figure 7.1 The IEEE exposure limit B-field squared multiplied by frequency, $B^2_{safe}\omega$, versus frequency for a ME WPTS following the IEEE exposure limits. For a ME WPTS, the optimal operating frequency is 100 kHz.

REFERENCES

[1] A. Kurs, A. Karalis, R. Moffatt, J. D. Joannopoulos, P. Fisher, and M. Soljačić, "Wireless power transfer via strongly coupled magnetic resonances," *Science (80-.).*, vol. 317, no. 5834, pp. 83–86, Jul. 2007.

[2] "What is a pacemaker?," *Boston Scientific*, 2015. [Online]. Available: www.bostonscientific.com,. [Accessed: 14-Apr-2022].

[3] H. Dinis and P. M. Mendes, "A comprehensive review of powering methods used in state-of-the-art miniaturized implantable electronic devices," *Biosens. Bioelectron.*, vol. 172, p. 112781, Jan. 2021.

[4] Hao Jiang *et al.*, "A low-frequency versatile wireless power transfer technology for biomedical implants," *IEEE Trans. Biomed. Circuits Syst.*, vol. 7, no. 4, pp. 526–535, Aug. 2013.

[5] D. Ahn and M. Ghovanloo, "Optimal design of wireless power transmission links for millimeter-sized biomedical implants," *IEEE Trans. Biomed. Circuits Syst.*, vol. 10, no. 1, pp. 125–137, Feb. 2016.

[6] J. S. Ho *et al.*, "Wireless power transfer to deep-tissue microimplants.," *Proc. Natl. Acad. Sci. U. S. A.*, vol. 111, no. 22, pp. 7974–9, Jun. 2014.

[7] D. Ahn and S. Hong, "Wireless power transmission with self-regulated output voltage for biomedical implant," *IEEE Trans. Ind. Electron.*, vol. 61, no. 5, pp. 2225–2235, May 2014.

[8] R.-F. Xue, K.-W. Cheng, and M. Je, "High-efficiency wireless power transfer for biomedical implants by optimal resonant load transformation," *IEEE Trans. Circuits Syst. I Regul. Pap.*, vol. 60, no. 4, pp. 867–874, Apr. 2013.

[9] S. Ha, C. Kim, J. Park, S. Joshi, and G. Cauwenberghs, "Energy recycling telemetry IC with simultaneous 11.5 mW power and 6.78 Mb/s backward data delivery over a single 13.56 MHz inductive link," *IEEE J. Solid-State Circuits*, vol. 51, no. 11, pp. 2664–2678, Nov. 2016.

[10] Y. Jia, B. Lee, S. A. Mirbozorgi, M. Ghovanloo, W. Khan, and W. Li, "Towards a free-floating wireless implantable optogenetic stimulating system," in *2017 IEEE 60th Int. Midwest Symp. on Circuits and Systems (MWSCAS)*, 2017, pp. 381–384.

[11] A. K. RamRakhyani, S. Mirabbasi, and M. Chiao, “Design and optimization of resonance-based efficient wireless power delivery systems for biomedical implants,” *IEEE Trans. Biomed. Circuits Syst.*, vol. 5, no. 1, pp. 48–63, Feb. 2011.

[12] W. X. Zhong, C. Zhang, X. Liu, and S. Y. R. Hui, “A methodology for making a three-coil wireless power transfer system more energy efficient than a two-coil counterpart for extended transfer distance,” *IEEE Trans. Power Electron.*, vol. 30, no. 2, pp. 933–942, Feb. 2015.

[13] H. S. Gougheri and M. Kiani, “Optimal frequency for powering millimeter-sized biomedical implants inside an inductively-powered homecage,” in *2016 38th Annu. Int. Conf. of the IEEE Engineering in Medicine and Biology Society (EMBC)*, 2016, pp. 4804–4807.

[14] A. Yakovlev, S. Kim, and A. Poon, “Implantable biomedical devices: Wireless powering and communication,” *IEEE Commun. Mag.*, vol. 50, no. 4, pp. 152–159, Apr. 2012.

[15] J. S. Ho, S. Kim, and A. S. Y. Poon, “Midfield wireless powering for implantable systems,” *Proc. IEEE*, vol. 101, no. 6, pp. 1369–1378, 2013.

[16] Y.-T. Liao, H. Yao, A. Lingley, B. Parviz, and B. P. Otis, “A 3-uW CMOS glucose sensor for wireless contact-lens tear glucose monitoring,” *IEEE J. Solid-State Circuits*, vol. 47, no. 1, pp. 335–344, Jan. 2012.

[17] A. S. Y. Poon, S. O’Driscoll, and T. H. Meng, “Optimal frequency for wireless power transmission into dispersive tissue,” *IEEE Trans. Antennas Propag.*, vol. 58, no. 5, pp. 1739–1750, May 2010.

[18] Y. Zhou, S. Chul Yang, D. J. Apo, D. Maurya, and S. Priya, “Tunable self-biased magnetoelectric response in homogenous laminates,” *Appl. Phys. Lett.*, vol. 101, no. 23, p. 232905, Dec. 2012.

[19] Shuxiang Dong, Jie-Fang Li, and D. Viehland, “Longitudinal and transverse magnetoelectric voltage coefficients of magnetostrictive/ piezoelectric laminate composite: experiments,” *IEEE Trans. Ultrason. Ferroelectr. Freq. Control*, vol. 51, no. 7, pp. 794–799, Jul. 2004.

[20] J. Ryu *et al.*, “Ubiquitous magneto-mechano-electric generator,” *Energy Environ. Sci.*, vol. 8, no. 8, pp. 2402–2408, Jul. 2015.

[21] T. Nan *et al.*, “Acoustically actuated ultra-compact NEMS magnetoelectric antennas,” *Nat. Commun.*, vol. 8, no. 1, pp. 1–8, Dec. 2017.

[22] T. Rupp, B. D. Truong, S. Williams, and S. Roundy, “Magnetoelectric transducer designs for use as wireless power receivers in wearable and implantable applications,”

Materials (Basel)., vol. 12, no. 3, p. 512, Feb. 2019.

[23] G. Rizzo, V. Loyau, R. Nocua, J. C. Lourme, and E. Lefeuvre, "Potentiality of magnetoelectric composites for wireless power transmission in medical implants," in *Int. Symp. on Medical Information and Communication Tech., ISMICT*, 2019, vol. 2019-May, pp. 1–4.

[24] K. Malleron, A. Gensbittel, H. Talleb, and Z. Ren, "Experimental study of magnetoelectric transducers for power supply of small biomedical devices," *Microelectronics J.*, vol. 88, pp. 184–189, Jun. 2019.

[25] R. C. O'Handley, J. K. Huang, D. C. Bono, and J. Simon, "Improved wireless, transcutaneous power transmission for in vivo applications," *IEEE Sens. J.*, vol. 8, no. 1, pp. 57–62, Jan. 2008.

[26] J. Xu *et al.*, "A low frequency mechanical transmitter based on magnetoelectric heterostructures operated at their resonance frequency," *Sensors*, vol. 19, no. 4, p. 853, Feb. 2019.

[27] "ICNIRP guidelines for limiting exposure to time-varying electric and magnetic fields (1 Hz-100 kHz)," 2010.

[28] "International commission on non-ionizing radiation protection icnirp guidelines for limiting exposure to electromagnetic fields (100 kHz to 300 GHz)," 2020.

[29] "C95.1-2019 - IEEE standard for safety levels with respect to human exposure to electric, magnetic, and electromagnetic fields, 0 Hz to 300 GHz.," IEEE, 2019.

[30] B. D. Truong, E. Andersen, C. Casados, and S. Roundy, "Magnetoelectric wireless power transfer for biomedical implants: Effects of non-uniform magnetic field, alignment and orientation," *Sensors Actuators A Phys.*, p. 112269, Aug. 2020.

[31] S. W. Park, "Investigating human exposure to a practical wireless power transfer system using and the effect about key parameters of dosimetry," *PLoS One*, vol. 15, no. 8, p. e0236929, Aug. 2020.

[32] D. B. Ahire, V. J. Gond, and J. J. Chopade, "Coil material and magnetic shielding methods for efficient wireless power transfer system for biomedical implant application," *Biosens. Bioelectron. X*, vol. 10, p. 100123, May 2022.

[33] K. M. Silay, C. Dehollain, and M. Declercq, "Inductive power link for a wireless cortical implant with two-body packaging," *IEEE Sens. J.*, vol. 11, no. 11, pp. 2825–2833, 2011.

[34] A. S. Y. Poon, S. O'driscoll, and T. H. Meng, "Optimal frequency for wireless power transmission into dispersive tissue," in *IEEE Trans. on Antennas and Propagation*,

2010, vol. 58, no. 5, pp. 1739–1750.

[35] A. Ibrahim, M. Meng, and M. Kiani, “A comprehensive comparative study on inductive and ultrasonic wireless power transmission to biomedical implants,” *IEEE Sens. J.*, vol. 18, no. 9, pp. 3813–3826, May 2018.

[36] K. Agarwal, R. Jegadeesan, Y. X. Guo, and N. V. Thakor, “Wireless power transfer strategies for implantable bioelectronics,” *IEEE Rev. Biomed. Eng.*, vol. 10, pp. 136–161, 2017.

[37] J. H. Cheong *et al.*, “An inductively powered implantable blood flow sensor microsystem for vascular grafts,” *IEEE Trans. Biomed. Eng.*, vol. 59, no. 9, pp. 2466–2475, 2012.

[38] S. Y. Lee, C. H. Hsieh, and C. M. Yang, “Wireless front-end with power management for an implantable cardiac microstimulator,” *IEEE Trans. Biomed. Circuits Syst.*, vol. 6, no. 1, pp. 28–38, Feb. 2012.

[39] O. Knecht and J. W. Kolar, “Performance evaluation of series-compensated IPT systems for transcutaneous energy transfer,” *IEEE Trans. Power Electron.*, vol. 34, no. 1, pp. 438–451, 2018.

[40] R. Jegadeesan, S. Nag, K. Agarwal, N. V. Thakor, and Y. X. Guo, “Enabling wireless powering and telemetry for peripheral nerve implants,” *IEEE J. Biomed. Heal. Informatics*, vol. 19, no. 3, pp. 958–970, May 2015.

[41] B. H. Waters, A. P. Sample, P. Bonde, and J. R. Smith, “Powering a ventricular assist device (VAD) with the free-range resonant electrical energy delivery (FREE-D) system,” *Proc. IEEE*, vol. 100, no. 1, pp. 138–149, 2012.

[42] M. A. Tanha, F. F. Hanzaee, R. Bayford, and A. Demosthenous, “RF wireless power transfer for EIT neonate lung function monitoring,” *Proc. - IEEE Int. Symp. Circuits Syst.*, vol. 2021-May, 2021.

[43] K. Fotopoulou and B. W. Flynn, “Wireless power transfer in loosely coupled links: Coil misalignment model,” *IEEE Trans. Magn.*, vol. 47, no. 2 PART 2, pp. 416–430, Feb. 2011.

[44] B. W. Flynn and K. Fotopoulou, “Rectifying loose coils: Wireless power transfer in loosely coupled inductive links with lateral and angular misalignment,” *IEEE Microw. Mag.*, vol. 14, no. 2, pp. 48–54, 2013.

[45] S. Aldhaher, P. C. K. Luk, and J. F. Whidborne, “Electronic tuning of misaligned coils in wireless power transfer systems,” *IEEE Trans. Power Electron.*, vol. 29, no. 11, pp. 5975–5982, 2014.

[46] O. Jonah, S. V. Georgakopoulos, and M. M. Tentzeris, “Orientation insensitive power transfer by magnetic resonance for mobile devices,” *2013 IEEE Wirel. Power Transf. WPT 2013*, pp. 5–8, 2013.

[47] D. Liu, H. Hu, and S. V. Georgakopoulos, “Misalignment sensitivity of strongly coupled wireless power transfer systems,” *IEEE Trans. Power Electron.*, vol. 32, no. 7, pp. 5509–5519, Jul. 2017.

[48] Y. Li, J. Zhao, Q. Yang, L. Liu, J. Ma, and X. Zhang, “A novel coil with high misalignment tolerance for wireless power transfer,” *IEEE Trans. Magn.*, vol. 55, no. 6, pp. 1–4, Jun. 2019.

[49] D. Liu and S. V. Georgakopoulos, “Cylindrical misalignment insensitive wireless power transfer systems,” *IEEE Trans. Power Electron.*, vol. 33, no. 11, pp. 9331–9343, Nov. 2018.

[50] A. J. Petruska and J. J. Abbott, “Omnimagnet: An omnidirectional electromagnet for controlled dipole-field generation,” *IEEE Trans. Magn.*, vol. 50, no. 7, pp. 1–10, 2014.

[51] W. M. Ng, C. Zhang, D. Lin, and S. Y. R. Hui, “Two- and three-dimensional omnidirectional wireless power transfer,” *IEEE Trans. Power Electron.*, vol. 29, no. 9, pp. 4470–4474, 2014.

[52] C. Zhang, D. Lin, and S. Y. Hui, “Basic control principles of omnidirectional wireless power transfer,” *IEEE Trans. Power Electron.*, vol. 31, no. 7, pp. 5215–5227, Jul. 2016.

[53] J. H. Kim, B. H. Choi, H. R. Kim, and C. T. Rim, “2-D synthesized magnetic field focusing technology with loop coils distributed in a rectangular formation,” *IEEE Trans. Ind. Electron.*, vol. 66, no. 7, pp. 5558–5566, Jul. 2019.

[54] M. W. Kim *et al.*, “High-resolution synthesized magnetic field focusing for RF barcode applications,” *IEEE Trans. Ind. Electron.*, vol. 65, no. 1, pp. 597–607, 2018.

[55] B. H. Choi, J. H. Kim, J. P. Cheon, and C. T. Rim, “Synthesized magnetic field focusing using a current-controlled coil array,” *IEEE Magn. Lett.*, vol. 7, pp. 1–4, 2016.

[56] N. Tesla, “Apparatus for transmitting electrical energy.,” 1907.

[57] M. Schormans, V. Valente, and A. Demosthenous, “Practical inductive link design for biomedical wireless power transfer: A tutorial,” *IEEE Trans. Biomed. Circuits Syst.*, vol. 12, no. 5, pp. 1112–1130, Jul. 2018.

[58] H. J. Kim, H. Hirayama, S. Kim, K. J. Han, R. Zhang, and J. W. Choi, “Review of near-field wireless power and communication for biomedical applications,” *IEEE Access*,

vol. 5, pp. 21264–21285, Sep. 2017.

[59] M. Song, P. Belov, and P. Kapitanova, “Wireless power transfer inspired by the modern trends in electromagnetics,” *Appl. Phys. Rev.*, vol. 4, no. 2, p. 021102, Apr. 2017.

[60] H. Chen *et al.*, “Ultra-compact mechanical antennas,” *Appl. Phys. Lett.*, vol. 117, no. 17, p. 170501, Oct. 2020.

[61] M. Zaeimbashi *et al.*, “Ultra-compact dual-band smart NEMS magnetoelectric antennas for simultaneous wireless energy harvesting and magnetic field sensing,” *Nat. Commun. 2021 121*, vol. 12, no. 1, pp. 1–11, May 2021.

[62] M. Muhibbullah, A. M. A. Haleem, and Y. Ikuma, “Frequency dependent power and energy flux density equations of the electromagnetic wave,” *Results Phys.*, vol. 7, pp. 435–439, Jan. 2017.

[63] C. Wei and X. Jing, “A comprehensive review on vibration energy harvesting: Modelling and realization,” *Renew. Sustain. Energy Rev.*, vol. 74, pp. 1–18, Jul. 2017.

[64] S. Yuan, Y. Huang, J. Zhou, Q. Xu, C. Song, and P. Thompson, “Magnetic field energy harvesting under overhead power lines,” *IEEE Trans. Power Electron.*, vol. 30, no. 11, pp. 6191–6202, Nov. 2015.

[65] S. W. Wright, M. E. Kiziroglou, S. Spasic, N. Radosevic, and E. M. Yeatman, “Inductive energy harvesting from current-carrying structures,” *IEEE Sensors Lett.*, vol. 3, no. 6, Jun. 2019.

[66] M. E. Kiziroglou, S. W. Wright, and E. M. Yeatman, “Coil and core design for inductive energy receivers,” *Sensors Actuators A Phys.*, vol. 313, p. 112206, Oct. 2020.

[67] B. D. Truong, C. Roundy, E. Andersen, and S. Roundy, “Analysis of resonance and anti-resonance frequencies in a wireless power transfer system: Analytical model and experiments,” *IEEE Trans. Circuits Syst. II Express Briefs*, vol. 66, no. 7, pp. 1222–1226, Jul. 2019.

[68] M. Zargham and P. G. Gulak, “Maximum achievable efficiency in near-field coupled power-transfer systems,” *IEEE Trans. Biomed. Circuits Syst.*, vol. 6, no. 3, pp. 228–245, 2012.

[69] B. Duc Truong, T. Le, and B. Sensale-Rodriguez, “Two-coil wireless power transfer system configured in series-series topology: fundamental dynamics and limitations on transmitted power,” *Appl. Phys.*, pp. 1–14, Nov. 2020.

[70] B. D. Truong, “Power optimization of a magnetoelectric wireless power transfer system with volume constraint,” *Sensors Actuators A Phys.*, vol. 341, p. 113226, Jul. 2022.

[71] E. Alper and D. Inman, *Piezoelectric Energy Harvesting*. Wiley, 2011.

[72] B. D. Truong and S. Roundy, "Wireless power transfer system with center-clamped magneto-mechano-electric (MME) receiver: Model validation and efficiency investigation," *Smart Mater. Struct.*, vol. 28, no. 1, p. 015004, Jan. 2019.

[73] V. R. Challa, J. O. Mur-Miranda, and D. P. Arnold, "Wireless power transmission to an electromechanical receiver using low-frequency magnetic fields," *Smart Mater. Struct.*, vol. 21, no. 11, p. 115017, Oct. 2012.

[74] K. Sondhi *et al.*, "Modeling and experimental analysis of rotating magnet receivers for electrodynamic wireless power transmission," *J. Phys. D. Appl. Phys.*, vol. 52, no. 18, p. 185501, Feb. 2019.

[75] C. S. Kong, "A general maximum power transfer theorem," *IEEE Trans. Educ.*, vol. 38, no. 3, pp. 296–298, 1995.

[76] B. D. Truong, "Investigation on power optimization principles for series-configured resonant coupled wireless power transfer systems," *AEU - Int. J. Electron. Commun.*, vol. 106, pp. 67–81, Jul. 2019.

[77] B. D. Truong and S. Roundy, "Experimentally validated model and power optimization of a magnetoelectric wireless power transfer system in free-free configuration," *Smart Mater. Struct.*, vol. 29, no. 8, p. 085053, 2020.

[78] G. K. Felic, D. Ng, and E. Skafidas, "Investigation of frequency-dependent effects in inductive coils for implantable electronics," *IEEE Trans. Magn.*, vol. 49, no. 4, pp. 1353–1360, 2013.

[79] Y. Kuang *et al.*, "Magnetic field energy harvesting from the traction return current in rail tracks," *Appl. Energy*, vol. 292, p. 116911, Jun. 2021.

[80] H. B. DWIGHT, "Skin effect in tubular and flat conductors," *Trans. Am. Inst. Electr. Eng.*, vol. 37, pp. 1379–1403, 1918.

[81] J. D. Co, "Skin effect in rectangular conductors at high frequencies," *Proc. R. Soc. London. Ser. A, Contain. Pap. a Math. Phys. Character*, vol. 122, no. 790, pp. 533–542, Feb. 1929.

[82] Z. Pantic and S. Lukic, "Computationally-efficient, generalized expressions for the proximity-effect in multi-layer, multi-turn tubular coils for wireless power transfer systems," *IEEE Trans. Magn.*, vol. 49, no. 11, pp. 5404–5416, 2013.

[83] J. Kim and Y. J. Park, "Approximate closed-form formula for calculating ohmic resistance in coils of parallel round wires with unequal pitches," *IEEE Trans. Ind. Electron.*, vol. 62, no. 6, pp. 3482–3489, Jun. 2015.

[84] A. Aharoni, “Demagnetizing factors for rectangular ferromagnetic prisms,” *J. Appl. Phys.*, vol. 83, no. 6, p. 3432, Jun. 1998.

[85] E. Andersen, C. Casados, B. D. Truong, and S. Roundy, “Optimal Transmit Coil Design for Wirelessly Powered Biomedical Implants Considering Magnetic Field Safety Constraints,” *IEEE Trans. Electromagn. Compat.*, vol. 63, no. 5, pp. 1735–1747, Oct. 2021.

[86] R. Ravaud, G. Lemarquand, V. Lemarquand, S. Babic, and C. Akyel, “Calculation of the magnetic field created by a thick coil,” *J. Electromagn. Waves Appl.*, vol. 24, no. 10, pp. 1405–1418, 2010.

[87] S. Babic, Z. Andjelic, B. Krstajic, and S. Salon, “Analytical calculation of the 3D magnetostatic field of a toroidal conductor with rectangular cross section,” *IEEE Trans. Magn.*, vol. 24, no. 6, pp. 3162–3164, Nov. 1988.

[88] T. Ikeda, *Fundamentals of Piezoelectricity*. Oxford Univeristy Press, 1996.

[89] E. Halvorsen, “Optimal load and stiffness for displacement-constrained vibration energy harvesters,” pp. 1–7, Mar. 2016.

[90] E. B. Tadmor and G. Kósa, “Electromechanical coupling correction for piezoelectric layered beams,” *J. Microelectromechanical Syst.*, vol. 12, no. 6, pp. 899–906, Dec. 2003.

[91] M. Renaud *et al.*, “Optimum power and efficiency of piezoelectric vibration energy harvesters with sinusoidal and random vibrations,” *J. Micromechanics Microengineering*, vol. 22, no. 10, p. 105030, Sep. 2012.

[92] I. Marinova and V. Mateev, “Electromagnetic field modeling in human tissue,” *Int. J. Biomed. Biol. Eng.*, vol. 4, no. 4, pp. 140–145, 2010.

[93] P. K. Sharma and S. K. Guha, “Transmission of time varying magnetic field through body tissue,” *J. Biol. Phys.*, vol. 3, no. 2, pp. 95–102, Jun. 1975.

[94] P. N. Morgan, “Optimal design and construction of a lightweight minimum-power solenoid magnet,” *IEEE Trans. Magn.*, vol. 37, no. 5, pp. 3814–3817, 2001.

[95] A. Miklavc, “The solenoid which gives the desired value of magnetic field for the smallest possible volume of conductor,” *J. Appl. Phys.*, vol. 45, no. 4, pp. 1680–1681, Apr. 1974.

[96] P. N. Murgatroyd, “The optimal form for coreless inductors,” *IEEE Trans. Magn.*, vol. 25, no. 3, pp. 2670–2677, May 1989.

[97] E. Andersen, B. D. Truong, and S. Roundy, “Optimal coil design for wireless

powering of biomedical implants considering safety constraints," in *IEEE MTT-S Wireless Power Transfer Conf.*, 2019, no. 2, pp. 106–110.

[98] C. C. Kaeding, B. Léger-St-Jean, and R. A. Magnussen, "Epidemiology and diagnosis of anterior cruciate ligament injuries," *Clin. Sports Med.*, vol. 36, no. 1, pp. 1–8, Jan. 2017.

[99] EPRS, "New EU regulatory framework for batteries," 2022.

[100] Z. Zhang, H. Pang, A. Georgiadis, and C. Cecati, "Wireless power transfer - an overview," *IEEE Trans. Ind. Electron.*, vol. 66, no. 2, pp. 1044–1058, Feb. 2019.

[101] L. Chen, P. Li, Y. Wen, and Y. Zhu, "Large self-biased effect and dual-peak magnetoelectric effect in different three-phase magnetostrictive/piezoelectric composites," *J. Alloys Compd.*, vol. 606, pp. 15–20, Sep. 2014.

[102] M. Li, Z. Wang, Y. Wang, J. Li, and D. Viehland, "Giant magnetoelectric effect in self-biased laminates under zero magnetic field," *Appl. Phys. Lett.*, vol. 102, no. 8, p. 082404, Feb. 2013.

[103] S. K. Mandal, G. Sreenivasulu, V. M. Petrov, and G. Srinivasan, "Magnetization-graded multiferroic composite and magnetoelectric effects at zero bias," *Phys. Rev. B - Condens. Matter Mater. Phys.*, vol. 84, no. 1, p. 014432, Jul. 2011.

[104] E. Andersen, O. Saha, and S. Roundy, "A dynamic transmit coil for wirelessly powering small ME transducer based biomedical implants," *2021 IEEE 20th Int. Conf. Micro Nanotechnol. Power Gener. Energy Convers. Appl. PowerMEMS 2021*, pp. 212–215, 2021.

[105] O. Saha, E. Andersen, and S. Roundy, "Wireless power transfer by self-biased magnetoelectric laminate for biomedical implants," *2021 IEEE 20th Int. Conf. Micro Nanotechnol. Power Gener. Energy Convers. Appl. PowerMEMS 2021*, pp. 36–39, 2021.

[106] Y. Yu, T. Nguyen, P. Tathireddy, S. Roundy, and D. J. Young, "A wireless battery-less and moisture-resistant packaged glucose sensing system employing hydrogel-based inductive sensing technique and low-power ASIC for long-term glucose monitoring," *Sensors Actuators A Phys.*, vol. 341, p. 113574, Jul. 2022.